Search for gamma-ray emission from supernova remnants with the *Fermi*/LAT and MAGIC telescopes

Tesi doctoral

Ignasi Reichardt Candel

Universitat Autònoma de Barcelona
Departament de Física
08193 Bellaterra (Barcelona)
Spain
<ignasi@ifae.cat>

September 2012

Supervised by Dr. F. Javier Rico Castro
Co-supervised by Dr. Emma de Oña Wilhelmi

Resum

Aquesta tesi és sobre el problema dels raigs csmics galàctics, enfocat des de l'astrofísica.

Els raigs csmics són partícules d'alta energia que impacten l'atmosfera de la terra des de dalt. El descobriment del seu origen extraterrestre s'atribueix a Victor Hess, que va dur a terme una sèrie d'experiments clau ara fa cent anys. El centenari del descobriment ha estat celebrat mentre aquesta tesi era escrita. Aquesta coincidència ha motivat que es fes una breu recerca histrica sobre els desenvolupaments clau dels inicis de la física de raigs csmics. També es revisa l'estat actual del camp, posant l'èmfasi en la composició, la forma espectral i la cerca d'anisotropies. El Capítol 1 acaba amb la discussió sobre el coneixement que es té actualment sobre els possibles llocs d'acceleració de raigs csmics. A energies per sota de $10^{15.5}$ eV, es creu que les restes de supernova de la Galàxia són els principals contribuents. La resta de la tesi és dedicada a l'estudi de l'emissió de raigs gamma d'aquests objectes.

Els processos físics presents en restes de supernova són introduts al Capítol 2. El mecanisme paradigmàtic conegut com acceleració difusiva per xocs emplacen les restes de supernova com eficients acceleradors de raigs csmics. La millor manera d'aconseguir informació sobre les partícules accelerades a les restes de supernova és observar-ne els raigs gamma. Per tant, els processos d'emissió de raigs gamma són explicats. Els processos d'emissió que involucren protons accelerats són d'un interès particular, ja que aquests són les partícules majoritàries dels raigs csmics. Ens concentrem en la possibilitat de que hi hagi núvols moleculars a prop de les restes de supernova, doncs aquests intensifiquen l'emissió de raigs gamma. Finalment, una llista de candidates a ser observades des de l'hemisferi nord és produda.

Els telescopis als que hem tingut accés per dur a terme observacions de restes de supernova en el domini dels raigs gamma són *Fermi*/LAT i MAGIC. Ambdós són presentats al Capítol 3. *Fermi*/LAT és un telescopi espacial, amb cobertura de tot el cel, que proveeix accés lliure a les dades a través d'una pàgina web. Per tant, la cobertura dels objectes seleccionats estava garantida en aquest rang d'energia. En canvi, MAGIC és operat per una col·laboració internacional d'institucions de recerca. Com a membres de la col·laboració MAGIC, vam poder proposar l'observació d'alguns dels objectes a la nostra llista de candidats, i aquestes van ser acceptades i dutes a terme. Els telescopis MAGIC són descrits detalladament, en particular pel que fa a l'anàlisi de dades, ja que l'autor hi tenia responsabilitats dins de la col·laboració.

El primer objecte individual en ser presentat són les restes de supernova HB 21 (Capítol 4). L'anàlisi de les dades públiques del telescopi *Fermi*/LAT ens porta a destacar l'existència d'una font extensa i resolta de raigs gamma. Vam ser capa cos de dividir la font en tres regions i obtenir l'espectre de cada una d'elles. Com a resultat, vam trobar variacions espectrals al llarg de les restes de supernova, que nosaltres relacionem amb variacions de les propietats del medi interestel·lar.

Al Capítol 5 expliquem les observacions de les restes de supernova conegudes com el Lla c del Cigne. De la mateixa manera que per HB 21, la font és resolta en les observacions amb *Fermi*/LAT, i duem a terme un anàlisi similar al de HB 21, en el que trobem que les variacions espectrals són encara més acusades. Hi ha dos punts en particular que presenten un espectre més dur, que s'estén fins uns quants GeV. Resulta que un d'aquests punts va ser observat gràcies a la nostra proposta d'observar el Lla c del Cigne amb els telescopis MAGIC, abans de tenir la informació de *Fermi*/LAT, i basant-nos només en estimacions grolleres del flux fetes a partir de la densitat del medi interestel·lar.

Tant el Lla c del Cigne com HB 21 resulten ser restes de supernova properes i de baixa lluminositat. Per contra, les restes de supernova W51C (presentades al Capítol 6) són les més lluminoses detectades fins ara a la Galàxia. Les nostres observacions amb els telescopis MAGIC estenen fins a 5 TeV les mesures de l'espectre fetes prèviament per la col·laboració *Fermi*. Amés, localitzem la regió d'emissió en una zona molt particular on W51C interacciona amb la W51B, una regió de formació estel·lar vena. La resta de la closca que formen les restes d'aquesta supernova no emet raigs gamma, excepte per una pic d'emissió secundària (no significatiu per ell mateix) que coincideix amb una possible nebulosa de vent de púlsar.

Per concloure, discutim l'impacte d'aquestes observacions en el camp de l'emissió d'alta energia de restes de supernova. Emfatitzem la utilitat de les observacions resoltes espacialment per l'estudi de l'escapament i difusió de raigs csmics procedents de restes de supernova. També mencionem l'existència d'una població de restes de supernova de baixa lluminositat a la qual pertanyen el Lla c del Cigne i HB 21. Aquestes restes de supernova de baixa lluminositat podrien ser abundants a la Galàxia, i per tant tenir una contribució important al flux de raigs csmics.

Summary

This thesis is an astrophysical approach to the problem of the Galactic cosmic rays.

Cosmic rays are energetic particles that hit the Earth atmosphere from above. The discovery of its extraterrestrial origin is attributed to Victor Hess, who conducted a series of key experiments one hundred years ago. The centenary of the discovery has been celebrated at the time this thesis has been written. This coincidence motivated to perform a brief historical search of the key developments of the early history of the cosmic-ray physics. The current status of the field is also reviewed, focusing in composition, spectral shape and anisotropy searches. Chapter 1 ends discussing the current knowledge of the possible acceleration sites of cosmic rays. At energies below $10^{15.5}$ eV, Galactic supernova remnants are believed to be the main contributors. The rest of the thesis is devoted to the study of gamma-ray emission from some of these objects.

Physical processes in supernova remnants are introduced in Chapter 2. The paradigmatic mechanism known as diffusive shock acceleration places supernova remnants as efficient cosmic-ray accelerators. Information regarding particles accelerated in supernova remnants is best gathered by observing them in the gamma-ray domain. Therefore, emission processes yielding gamma rays are discussed. Mechanisms involving accelerated protons are of particular interest, as they prove the majority component in the cosmic rays. We focus in the possibility of having molecular clouds near supernova remnants enhancing the gamma-ray emission. Finally, a list of candidates for being observed from the northern hemisphere is elaborated.

The telescopes to which we had access to perform observations of supernova remnants in the gamma-ray domain were *Fermi*/LAT and MAGIC. Both are introduced in Chapter 3. *Fermi*/LAT is a space telescope with all-sky coverage that provides free access to the data through a web page. Therefore, the coverage of the objects of interest was granted in this energy range. MAGIC instead, is operated by an international collaboration of institutions. As members of the MAGIC collaboration, we were able to propose observations of some of the objects in our target list, that were accepted and conducted. The MAGIC telescopes themselves are described with some detail, in particular the aspects regarding data analysis, in which the author had responsibilities within the collaboration.

The first of the individual objects to be discussed is the supernova remnant HB 21 (Chapter 4). The analysis of the public *Fermi*/LAT data lead us to claim the existence of a resolved gamma-ray source. We were able to divide the source in three regions and obtain the spectrum of each of them. As a result, we found that there are spectral variations across the supernova remnant, that we attribute to variations in the properties of the interstellar medium.

In Chapter 5 we discuss observations of the Cygnus Loop supernova remnant. Same as for HB 21, the source is resolved in the observations with *Fermi*/LAT, and we perform an analysis similar to that of HB 21, in which we find even more marked spectral variations.

There are two spots in particular that present a harder spectrum, extending to energies of several GeV. It turns out that one these spots was targeted by our proposal to observe the Cygnus Loop with the MAGIC telescopes, prior to knowing the information from *Fermi*/LAT, and based only in rough flux expectations based on the interstellar medium density.

Both the Cygnus Loop and HB 21 happen to be low-luminosity, nearby supernova remnants. In contrast with these objects, the supernova remnant W51C (discussed in Chapter 6) is the most luminous gamma-ray emitting supernova remnant detected so far in the Galaxy. Our observations with the MAGIC telescopes extend the spectrum previously measured by the *Fermi* Collaboration up to energies of 5 TeV. In addition, we locate the emission region in a very particular zone of interaction between W51C and the adjacent star-forming region W51B. The rest of the supernova remnant shell is dark in gamma rays, except for a secondary emission peak (not significant by itself) coincident with a possible pulsar wind nebula.

To conclude, we discuss the impact that these observations have in the field of high-energy emission from supernova remnants. We stress the convenience of space-resolved observations for the study of the escape and diffusion of cosmic rays from supernova remnants. We also note the existence of a population of low luminosity supernova remnants of which Cygnus Loop and HB 21 are representatives. These low luminosity supernova remnants could be abundant in the Galaxy, and thus could have a large contribution to the cosmic rays.

Contents

Chapter 1

Cosmic rays and its origin

Cosmic rays were established as such one hundred years ago by Victor Hess. This discovery represented the first source of cosmic information beyond optical astronomy, long before the advent of radio, infrared, ultraviolet, X-ray and gamma-ray astronomies. Moreover, the investigation of cosmic rays widened the field of particle physics, remaining as the main resource for discovering new particles until the 1950s. The discovery of extensive air showers by Pierre Auger in 1938 suggested that the maximum energies must be higher than 10^{15} eV. In the 1960s it became clear that some of these particles actually reached energies of about 10^{20} eV. It is commonly believed that cosmic rays with energies up to some 10^{15} eV are accelerated at the shock fronts of Galactic supernova remnants, at their early stages of evolution. However, a firm confirmation is still missing. If this energy range poses a puzzle, then the 10^{20} eV range is a complete mystery.

1.1 Discovery and early history of cosmic rays

It can be said that the discovery of the cosmic rays is a byproduct of the studies on the conductivity of the air, initiated by C. A. de Coulomb in 1785. By the end of the 19^{th} century, the discovery of natural radioactivity and, consequently, how α, β and γ rays ionize gases, provided a decisive hint to solve the problem. The solution to the -initially- marginal problem of why a charged conductor in an isolated container did lose its charge resulted in a spectacular discovery with unsuspected consequences for physics and astronomy (Walter and Wolfendale, 2012).

From the instrumental side, the key device was the electrometer, invented by Abraham Bennet in 1789. An electrometer consists of two thin gold leaves connected mounted on a metal bar. When the bar gets charged, the gold leaves separate from each other a certain distance, which is a measure of the charge accumulated in the device. Theodor Wulf introduced essential improvements to the design by substituting the leaves by strings and introducing an eyeglass with a micrometer scale for the separation measurements.

In 1909 and 1910 some controversy was raised between Wulf and Pacini regarding the origin of the γ radiation *existing in the atmosphere*. Wulf reported that this radiation was produced by radioactive substances concentrated in the upper earth layer, down to a depth of one meter. He assessed that if part of the radiation came from the atmosphere, then it was to small to be detected with the electrometers he had (Wulf, 1909). In contrast, Pacini performed his measurements on the Mediterranean sea, far from the shore and water depths of more than 4 meters. Under these circumstances, no radiation

was expected from the soil, but he was still detecting two thirds of the ionization that Wulf found on the ground. Pacini concluded that "a sizable cause of ionization exists in the atmosphere, originating from penetrating radiation, independent of direct action of radioactive substances in the soil" (Pacini, 1912).

The understanding of the presence of ionizing radiation in the atmosphere was further boosted by the studies in meteorology and geology aiming to measure the electric field of the Earth. For that purpose, Franz Linke flew a balloon six times in 1902 and 1903 and measured the conductivity of the air up to an altitude of 5500 m. His conclusion was "Would one compare the presented values with those on ground, one must say that in 1000 m altitude where the measurements in general began the leakage is smaller than on ground, between 1 and 3 km of the same amount, and above larger than on earth, with values increasing up to a factor of 4" (Linke, 1904). This represents an anticipation of the results that later lead to the discovery of cosmic rays. However, other balloon experiments did not reach conclusive results, mainly because of problems in the electrometers.

Equipped with improved, systematically calibrated electrometers, Victor Hess started his balloon flights in August 1911. The initial results were that at altitudes of up to 1000 m the ionization was compatible with that on the ground (not smaller), and independent on whether the balloon was flown during daytime or during nighttime. For the next series of flights, starting in April 1912, Hess defined thorough guidelines to be followed in order to improve the significance of the conclusions of the experiments. The new measures included checks of the ionization near the balloon right before takeoff and right after landing; flights at constant altitude to check variability of the ionization; and the use of three electrometers, two of them optimized for γ-radiation, and the other optimized for β-radiation. The first six flights started near Viena and a limited altitude was achieved. However, the results were already remarkable: both kinds of electrometers showed identical variations with time and altitude; one flight during a solar eclipse confirmed that ionization variations were not connected to solar activity; and the rate did not decrease significantly with the increasing altitude. For the seventh flight, Hess used a hydrogen filled balloon and took off in the morning of August 7^{th} from Aussing. A maximum altitude of 5350 m was reached before landing at noon, 60 km south-east of Berlin. The ionization rates measured in that flight are shown in figure 1.1. The sentence that established Hess as discoverer of the cosmic rays comes in the discussion of these results: "the results of these observations seem to be explained by the assumption, that a radiation of high penetration power hits our atmosphere from top, which causes also in their lower layers a fraction of the observed ionization in the closed detectors. The intensity seems to underlie variations which are visible in time intervals of one hour. Since I did not find a decrease of radiation during the night or during the eclipse, the sun can not be the reason for this hypothetical radiation, at least if one assumes a direct γ-radiation with straight-line propagation" (Hess, 1912).

Since γ-rays had the strongest penetration power of the three known types of ionizing radiation, it was natural to assume that cosmic rays consisted of γ-rays. However, Werner Kolhörster decided to check the results from Hess at higher altitude, using an improved electrometer, stable against temperature and pressure variations. In June 1914, Kolhörster started his record flight up to an altitude of 9300 m above Berlin. The measurements confirmed the results from Hess at lower altitude, and revealed that at 9000 m the ionization was a factor four higher than the measured by Hess at 4800 m. From this measurement, Kolhörster could estimate that the penetration power of the cosmic radiation was 4.5 times higher than γ-rays from radioactive sources. The culminating step in

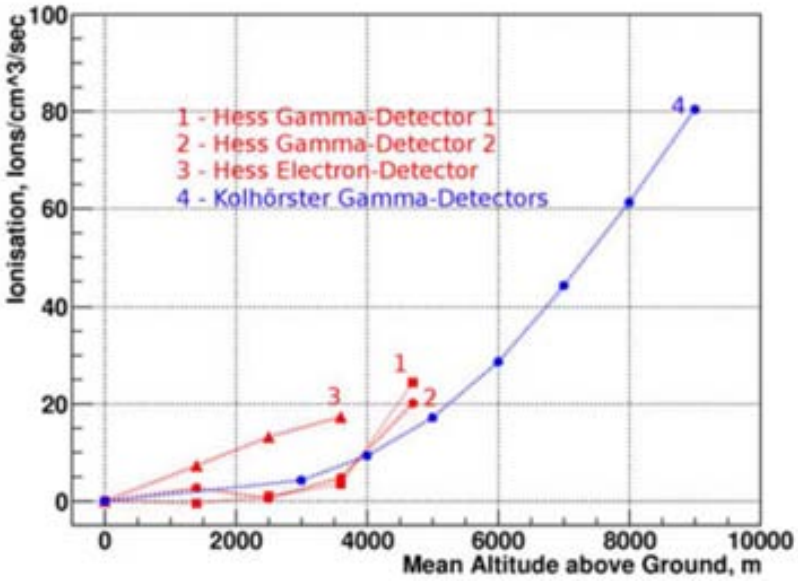

Figure 1.1: Curves 1-3: Ionization rate measured by Victor Hess in his seventh flight, August 1912. Curve 4: Ionization rate measured by Kolhörster in 1914. Figure extracted from Walter and Wolfendale (2012).

the development of the electrometers was the introduction of automated measurements. The separation between the strings was registered on a moving photographic film driven by a clockwork. These devices allowed in 1932 the measurement of the ionization rate from depths of -230 m to altitudes up to 30 km (Regener, 1932).

In 1928, the modification of ionization chambers towards the invention of the Geiger-Müller counter and the coincidence method by Walter Bothe lead to another breakthrough. Experiments by Kölhoster and Bothe demonstrated that the majority of cosmic rays were constituted by charged particles, and not γ-rays, as it had been assumed before. Moreover, it was demonstrated that there were differences in the properties measured at high altitude and well down in the atmosphere. It was later understood that this was due to the fact that at high altitude *primary* particles were detected, whereas byproducts of the interaction of the primaries with the air (or *secondaries*) were mainly detected at ground level. These studies culminated in the discovery of the extensive air showers by Auger and Maze in 1938. A possible East-West difference induced by the geomagnetic field was postulated by Rossi in 1931. This effect was seen by Johnson, Alvarez and Compton by their measurements in Mexico city in 1933, and confirmed by Rossi himself in equivalent observations in Eritrea. The surprising outcome was that the charge was preferably positive (electrons were expected by many before that) and typical energies ranged from a several to tens of GeV.

In 1908, Hale discovered the magnetic field of the solar system. Therefore, the realization that cosmic rays were mainly charged particles implied that their trajectory could not be traced back to their sources. The first possible responsible to be suggested were the Sun or double stars. Finally, attention was given to the work by Baade and Zwicky involving supernovae (Baade and Zwicky, 1934*b*,*a*). This association was based on the enormous luminosities measured in supernovae, which they estimated to peak at 10^8 solar luminosities. However, Baade and Zwicky insisted that cosmic rays had to be of extra-

galactic origin, *because no supernova had been detected in the Galaxy during the time that cosmic rays had been measured*. The authors gave values for the energy of cosmic rays emitted per supernova, and the supernova rate in the Universe that do not match the present measurements. Naturally, they were not aware of the Galactic trapping, nor the role of supernova remnant shocks.

In parallel to the measurements with electrometers, the accidental discovery of the cloud chamber by Wilson had provided the evidence that ionization explains the conductivity of the air. Few months before the 1912 flights by Hess, Wilson had photographed straight tracks in his device which were probably cosmic rays. In the 1930s the cloud chambers had been dramatically improved. With the introduction of magnetic fields and counter-controlled photographs it was possible to identify a particles with the mass and charge of the electron, but with opposite sign. The discovery of the positron was followed by the muon, as a particle of intermediate mass between electron and proton. These developments motivated the construction of accelerators in the late 1940s, and therefore they represent the start of modern particle physics.

1.2 Cosmic-ray measurements

1.2.1 Cosmic-ray nuclei

Nowadays, dozens of experiments have measured the cosmic-ray spectrum over a huge range in energy (figure 1.2). Up to 10^{14} eV, direct detection and particle classification in balloon- or satellite-borne experiments is possible. Cosmic rays are mainly protons, with a 10% of helium and 1% of both heavier nuclei and electrons.

Between 10^{10} eV and $10^{15.5}$ eV, the spectrum follows a power law, $N_{\rm CR}(E) \propto E^{-2.7}$ (Hillas, 2006). This energy range is bounded by low energy fall-off -considered to be a local effect due to he heliosphere- and the spectral feature commonly known as the *knee*. Below the knee cosmic rays can be confined by the interstellar magnetic field, and thus are certainly of Galactic origin. Among the heavy nuclei, there is a remarkable excess of Li, Be and B with respect to the abundances measured in the solar system, which can be explained as the result of spallation of heavier cosmic-ray nuclei by interstellar gas. The overabundance allows to derive the typical confinement time in the Galactic disk, which is $t_d \approx 3 \times 10^6$ years. This confinement is energy-dependent, with high energy particles escaping faster: $t_{esc}(E) = t_d (E/10\,{\rm GeV})^{-\delta}$ and $\delta \approx 0.3 - 0.6$ (Gabici, 2012). The featureless spectrum in this range suggests the existence of a very dominant source class producing it. Taking into account that the observed spectrum is softened by propagation, the injection spectrum must be $Q(E) \propto E^{-2.7+\delta}$, i.e. cosmic-ray sources emit particles with spectral index $\alpha \approx 2.1 - 2.4$. Assuming that cosmic rays leave the Galaxy in the direction transverse to the disk, a diffusion coefficient $D \approx h/t^2 = D_0 (E/10\,{\rm GeV})^{\delta}$, with of the order of $D_0 \approx 10^{28} - 10^{29}\,{\rm cm^2 s^{-1}}$ is expected. The low level of anisotropy (discussed in section 1.3) favors the flattest possible energy dependency $\delta = 0.3$ of the diffusion coefficient so that cosmic rays up to the knee are isotropic as observed.

Results from KASCADE (Haungs, 2003) shown that every nuclear component has downward bend in the spectrum at a magnetic rigidity near 3×10^{15} V. This corresponds to energies of 3×10^{15} eV for protons, 6×10^{15} eV for helium nuclei and 8×10^{16} V for iron nuclei -the heaviest common nucleus. The present understanding of this measurement is that the main galactic component is produced by one dominant source class, which makes up several elemental components, each extending to an energy near $Z \times 3 \times 10^{15}$ eV, where

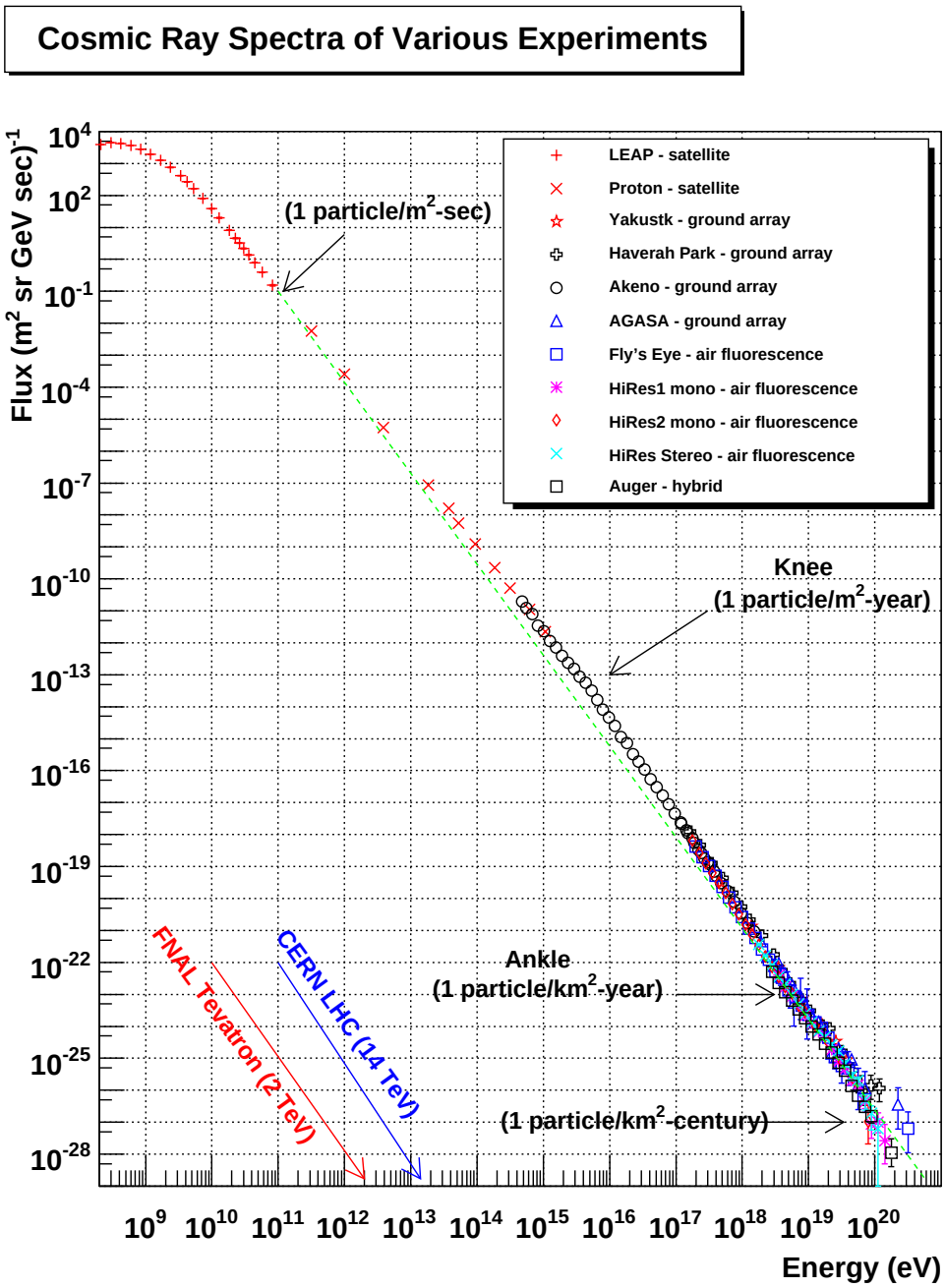

Figure 1.2: Energy flux of cosmic-ray particles reaching the Earth as a function of the energy per particle. Extracted from Hanlon (2009).

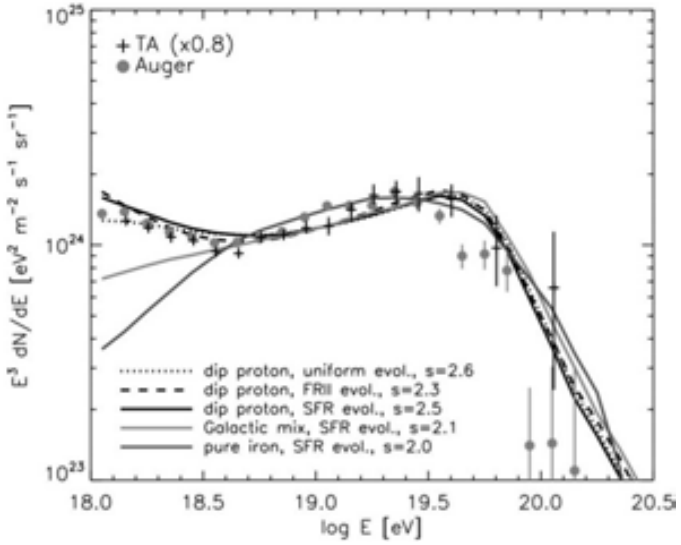

Figure 1.3: High energy end of the cosmic-ray flux measured by Auger and Telescope Array. In the mixed composition and iron dominated models, the ankle indicates a transition from Galactic to extragalactic cosmic rays, the source evolution is similar to the star-formation rate (SFR), and the injection spectra are relatively hard (power law index ∼2-2.1). In the proton dominated models in the figure, the ankle is due to pair production propagation losses, named "dip transition models", and the injection spectra are softer for a wide range of evolution models. Models with proton primaries can also fit the spectrum with harder injection with a transition from Galactic to extragalactic at the ankle. Extracted from (Olinto, 2012).

Ze is the charge of the nuclear charge of each component.

Beyond the knee, composition is derived from the observed development and particle content of the extensive air shower when it interacts with the atmosphere. The elemental component fluxes turn down sharply producing separated bends up to 10^{17} eV that are hardly noticeable in the spectrum. This series of turns down produces a smooth transition until above 10^{17} eV, where a second source class (perhaps of extragalactic origin) must become dominant. Near $10^{18.5}$ the cosmic-ray spectrum presents a hardening, commonly known as the *ankle* (figure 1.3). At these ultra-high energies the composition remains dominated by light nuclei, although Auger found a slight trend towards heavier nuclei starting at 10 EeV (Olinto, 2012).

Above $10^{19.5}$ eV statistics are scarce, but experiments like HiRes, Auger and Telescope Array have demonstrated the existence of a prominent softening of the spectrum. There is the possibility that this turn-down is due to the maximum energy achievable by the sources contributing above the ankle. However, the flux is also expected to drop sharply above due to energy losses accompanying pion production reactions between nucleons and cosmic microwave background (CMB) photons. This process, commonly known as the Greisen-Zatsepin-Kuzmin, GZK cut-off (Greisen, 1966; Zatsepin and Kuzmin, 1966). Both possibilities need of more statistics above 100 EeV in order to be solved.

1.2.2 Cosmic-ray electrons and positrons

Cosmic-ray electrons are much less numerous than protons: 1-2% around 1 GeV, and even more rare at higher energies. Alike for hadrons, the cosmic-ray electron spectrum is also expected to drop below 1 GeV due to the heliospheric modulation. Above 10 GeV

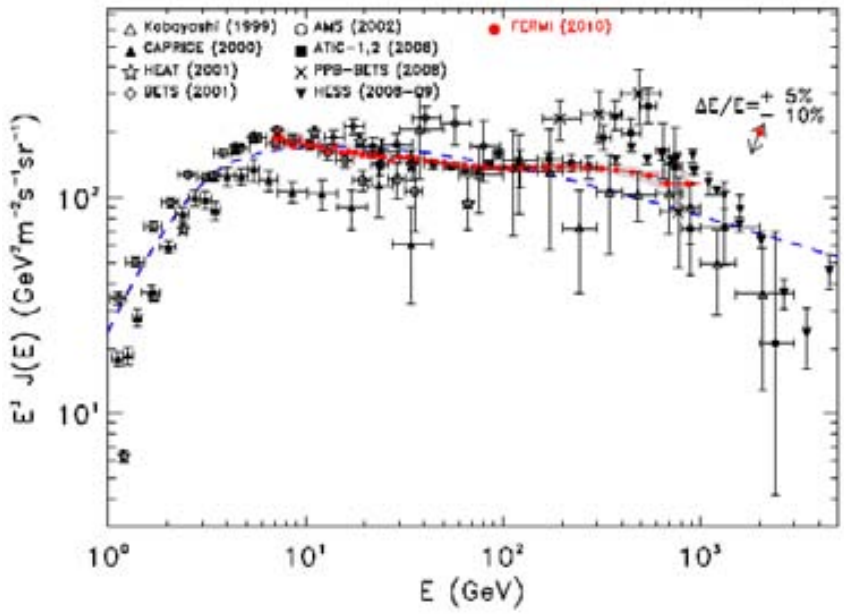

Figure 1.4: Cosmic-ray electron spectrum measured by *Fermi*/LAT (red circles) with other results from previous experiments. Dashed, blue line shows the model based on pre-*Fermi* results. Extracted from Ackermann et al. (2010).

the GALPROP model for the propagation of electrons from a distribution of supernova remnants and pulsars predicted a power-law spectrum with index 3.1-3.4 up to few hundred GeV, where local efects and temporal variations should dominate. However, the latest measurements with *Fermi*/LAT showed that the electron spectrum is significantly harder, with an average index of 3.08 ± 0.05, and a noticeable excess above 200 GeV as compared to the power-law fit (Ackermann et al., 2010). At higher energies, H.E.S.S (Aharonian et al., 2009) reported a significant steepening above 600 GeV (figure 1.4).

Cosmic-ray positrons are assumed to be secondary particles resulting from the interaction of a cosmic-ray nucleus with the interstellar gas. This process results in a positron fraction that decreases steadily with energy, whereas measurements show that it decreases up to ~ 10 GeV and then increases with energy (Adriani et al., 2010; Ackermann et al., 2012). This observation, together with the cosmic-ray electron spectrum discussed above indicate a nearby primary source of electrons and positrons which is not yet identified. The most plausible explanation seems the presence of a nearby pulsar, although a contribution from dark matter annihilation in the Galactic halo cannot be excluded.

1.3 Possible sites of acceleration of cosmic rays

Cosmic rays are mostly charged nuclei, and their arrival direction is deflected and highly iosotropized by the action of the Galactic and intergalactic magnetic fields. However, the Tibet ASγ experiment observed an energy-dependent, large-scale anisotropy in the arrival directions of multi-TeV protons with a relative amplitude of about $10^{-3} - 10^{-4}$ suggesting the existence of two distinct broad regions (Amenomori et al., 2006). Distributed around 40° to 90° in right ascension, the *tail-in* region shows an excess of cosmic rays. Conversely, the *loss cone*, distributed 150° to 240° in right ascension, shows a deficit. The origin of this

anisotropy is assumed to be related to the role of the most nearby, recent sources, or to a regular component in the Galactic magnetic field. In addition, the MILAGRO experiment reported evidence of a medium angular scale anisotropy contained in the tail-in region (Abdo et al., 2008). One of these regions presents a hard power-law spectrum with an exponential cutoff which deviates by $4.6\,\sigma$ from the isotropic power law measured around 10 TeV. Similar features were found by IceCube in the southern hemisphere (Abbasi et al., 2012). Finally, the ARGO-YBJ experiment not only confirmed the large- and medium-scale anisotropies found by Tibet ASγ and MILAGRO, but also reported the existence of multiple few-degree excesses not compatible with random fluctuations (Di Sciascio et al., 2012). Whether these anisotropies are due to local effects of the Galactic magnetic field or to nearby sources (or a combination of the two) is not yet fully understood.

In any case, point-like sources of cosmic-rays below the knee were completely unexpected. Even for cosmic rays with energies of the order of 1 EeV, there is little clear evidence of anisotropy, although the magnetic field in the vicinity of the Galaxy would not trap very effectively even the very heaviest nuclei. Therefore, the flux is presumed to originate much further away, most probably in systems dominated by jets from active galactic nuclei that could provide the necessary exceptional energy source. However, above 55 EeV the GZK attenuation would greatly diminish the flux originating at distances beyond the local Virgo supercluster. The magnetic fields intervening are not too strong and, at the greatest energies, diffuse particles from great distances should be strongly suppressed. Therefore, the so-called *trans-GZK* cosmic rays provide the opportunity to observe their sources in the local Universe, at distances closer than 100 Mpc. Indeed, Auger and Telescope Array have detected a hint of departure from isotropy in their set of trans-GZK events (Olinto, 2012). The yet weak signal indicates that at these energies still exists a large isotropic background. Interestingly, 19 out of 98 events in the Auger data set cluster around the closest active galactic nuclei: the radiogalaxy Centaurus A, at 3.8 Mpc. 7.6 events would be expected by chance correlation.

Primary and secondary neutrinos and photons can be produced in cosmic-ray sources, or by their interaction with ambient baryonic matter and radiation fields inside the source, or during their propagation from source to Earth. These particles travel in geodesics unaffected by magnetic fields and bear valuable information of the birthplace of their progenitors. The search of sources of cosmic rays has long been associated with the detection of neutrinos and gamma rays that might pinpoint the position of the accelerators in the sky.

Secondary neutrinos are very useful because, unlike cosmic-rays and photons, they are not absorbed by the cosmic backgrounds while propagating through the Universe. In particular, they give a unique access to observing sources at PeV energies. However, their small interaction cross-section makes it difficult to detect them on the Earth requiring the construction of km^3 or larger detectors. Neutrinos generated during ultra-high energy cosmic-ray propagation (often called cosmogenic neutrinos) represent a "guaranteed flux" and have encouraged efforts to detect them for decades. One important assumption for the existence of cosmogenic neutrinos is that cosmic rays are extragalactic at the highest energies. This has been verified by the detection of a feature consistent with the GZK cutoff in the cosmic ray spectrum and by the indication of anisotropies in the cosmic ray sky distribution at the highest energies.

The propagation of gamma rays is affected by their interaction with photon fields such as the extragalactic background light (infrared), CMB or radio waves, depending on the gamma-ray photon energy. These interactions lead to the production of high

energy electron and positron pairs which in turn up-scatter low-energy photons by inverse Compton processes, initiating electromagnetic cascades. As a consequence, one does not expect to observe gamma rays of energy above $\sim 1\,\mathrm{TeV}$ ($\sim 100\,\mathrm{TeV}$) from sources located beyond a horizon of a few Gpc (Mpc). However, these limitations are unimportant for the observation of acceleration sites within the Galaxy.

At energies of several GeV there is good evidence from observations of gamma rays produced in nuclear collisions that cosmic rays originate in the Galaxy and diffuse out (Hunter et al., 1997). Even when the supernova rate and the energy release measurements available to Baade and Zwicky were inaccurate, present observations prove correct that the power to maintain the Galactic population of cosmic rays is estimated to be a few percent of the total mechanical energy released by supernova explosions in our Galaxy. Therefore, their ideas evolved towards the common belief nowadays that the shocks produced in expanding supernova remnants (rather than supernovae themselves) are responsible for the galactic cosmic rays. The energetic argument must be fulfilled, but it is not exclusive: pulsars, young stars with powerful winds or microquasars also fulfill this argument. Further evidence supporting supernova remnants as main sources of Galactic cosmic rays are discussed below.

Theory provides quite a hint: predictions from diffusive shock acceleration applied to supernova remnant shocks foresee a power-law spectrum. Moreover, the non-linear treatment of the problem (Malkov and O'C Drury, 2001) revealed that the efficiency in the transfer of shock mechanical energy to non-thermal particles is of the order of 10% or higher, and that the photon index between 2 and 3 depending on the shock speed (Hillas, 2006).

Radio telescopes have for long drawn attention to supernova remnants as principal sources of multi-GeV electrons, through their synchrotron radiation. This fact is confirmed by the observation of featureless X-ray spectra in supernova remnants like SN 1006 or RX J1713.7-3946, which emit synchrotron radiation of $\sim 100\,\mathrm{TeV}$ electrons (Koyama, 2001). The existence of $\sim 100\,\mathrm{TeV}$ electrons revealed by X-ray observations of supernova remnants implies that protons in these systems must be accelerated to similar, or even higher energies. Accelerated protons are best proved by gamma-ray observations, although gamma-ray emission from supernova remnants might also have a leptonic origin. Indeed, 63 supernova remnants have been detected at GeV energies, and 25 have been detected at TeV energies (Ferrand and Safi-Harb, 2012). The hadronic origin of the gamma-ray emission for some of them is well established (e.g. Uchiyama et al., 2012; Aleksić et al., 2012). These observations add evidence that supernova remnants do contribute a large flux of protons to the main component of Galactic cosmic rays; multi-TeV observations add evidence that these systems can reach a maximum energy close to the knee.

Chapter 2

Physical processes in supernova remnants

Supernova remnants are important sources of energy and high energy particles in the Galaxy. After the free expansion stage, once the blast wave has swept up mass comparable to the mass of the ejecta, the blast wave expands adiabatically in a uniform medium. In this so-called Sedov phase is when the supernova remnant is able to accelerate particles to very-high energies via the mechanism of diffusive shock acceleration. Accelerated electrons and protons emit gamma rays through different processes discussed in this chapter.

2.1 Introduction

Supernova explosions are striking phenomena as they emit $\sim 10^{49}$ erg of visible radiation. This fact prompted the early claim from Baade and Zwicky (1934*a*) that supernovae could be responsible for the cosmic rays detected on Earth. However, most of the energy is released as kinetic energy of the ejecta. The supernova remnant consists of a shell of several solar masses initially expanding at several thousand km s^{-1} towards its surrounding medium. As a consequence, supernova remnants greatly determine the large-scale structure of the interstellar medium by heating it, ionizing it, and governing the mass exchange between various phases. In doing so, supernova remnants influence subsequent star formation and the recycling of heavy elements in galaxies.

Currently, 308 supernova remnants are known (Ferrand and Safi-Harb, 2012). Most of these objects are identified in radio continuum surveys, the limiting factors for their discovery being the surface brightness and the angular size. The distribution of supernova remnants in the Galaxy is expected to influence the cosmic-ray distribution, as well as the gamma-ray emission resulting from the interaction of cosmic rays with the interstellar medium. Green (2012) showed that this distribution may be modeled by a exponential radial profile with a minimum in the Galactic center:

$$\propto \left(\frac{R}{R_\odot}\right)^A \exp\left(-B\frac{R-R_\odot}{R_\odot}\right) \tag{2.1}$$

where the two parameters, A and B, are estimated by fitting the projection in Galactic longitude of the proposed model to the observed distribution of the 69 brightest supernova remnants. The maximum density of supernova remnants is attained around a radius of $\sim 1/3$ the distance to the Galactic center, $R_\odot$.

The evolution of supernova remnants is determined by their surrounding interstellar medium. Supernova remnant front shocks expand at constant velocity, and with constant interior temperature during the initial *free expansion* stage. A few hundred years after the supernova explosion, the supernova remnant enters the so-called *Sedov* phase, and the shock starts to slow down at a rate $v_{sh} \propto t^{-3/5}$. The slowdown corresponds to the time when the shock has reached a radius such that the swept up mass equals the mass of the ejecta. During this Sedov phase, the radius of the supernova remnant is $R = 13 \times (E_{51}/n_0)^{1/5} t_4^{2/5}$ pc, where E_{51} is the initial energy in units of 10^{51} erg, n_0, the ambient number density in units of cm^{-3}, and t_4, time in units of 10^4 years in a medium in which the mean mass per particle is $2.0 \times 10^{-24} g$ (Levenson et al., 1998). Rayleigh-Taylor instabilities mix up the ejected gas with the surrounding medium.

The Sedov phase lasts for 10000 to 20000 years, until the interior gas has cooled down to about 10^6 K and the pressure behind the blast wave is reduced. At this point, electrons start to recombine with ambient atoms and radiative losses become important. The beginning of the radiative phase occurs at $t = 1.9 \times 10^4 E_{51}^{3/14} n_0^{-4/7}$ years, when the radius is $R = 16.2 \times \ E_{51}^{2/7} n_0^{-3/7}$ pc, although the radiating shell is not fully formed yet (Levenson et al., 1998). Due to the cooling, the shell shrinks and becomes more dense, which increases the recombination reactions and therefore the energy loss. Eventually, the outward expansion stops and the shell starts to collapse under its own gravity, although Rayleigh-Taylor instabilities will break the material away and mix it with the interstellar medium rather than let it collapse to a new dense object.

Supernovae have two very different kinds of precursors. Type Ia supernovae are explosions of white dwarfs in binary systems, in which a late-type donor star transfers its outer layers to the compact object via Roche-lobe overflow. Eventually, the white dwarf reaches the Chandrasekhar mass $M_{Ch} = 1.44\, M_\odot$ and undergoes a runaway thermonuclear reaction that completely destroys the system. As white dwarves are old, evolved objects the explosion may happen in a place far away from the dense molecular environment where the binary system was born. The resulting supernova remnant, is often a clean, symmetrical shell which is unexpected to be disturbed by particularly dense clumps in its surroundings. In addition, no compact object is expected to be left behind the blast wave.

In contrast to type Ia, all other supernovae are produced by massive stars after the nuclear fuel in its core has been exhausted. The sudden drop of the inner thermal pressure causes the core to collapse beneath its own gravity, whereas the outer layers of the star are violently ejected. Depending on the mass of the progenitor, the collapsed object may become a neutron star or, if the Oppenheimer-Volkov mass $M_{OV} \sim 2 - 3\, M_\odot$ is exceeded, a black hole. Since massive stars evolve in few million year scales, the explosion most probably takes place near its native star-forming region, which is probably associated to a giant molecular cloud. Therefore the expansion of the ejecta is likely to be severely distorted by the surrounding medium.

If a neutron star is formed in a core-collapse explosion, a pulsar wind nebula will grow around it. Pulsar wind nebulae are likely accelerators of particles up to PeV energies, and the resulting gamma-ray emission is often superimposed to that from the supernova remnant. There is compelling evidence that particles dominating the gamma-ray emission in these objects are electrons producing synchrotron self-Compton radiation (discussed in section 2.3.2). Therefore, pulsar wind nebulae may not be major contributors to the cosmic ray flux. Instead, for the purpose of identifying sources of cosmic rays, pulsar wind

nebula act as a background rather than as a tracer.

2.2 Diffusive shock acceleration in supernova remnants

The model of diffusive shock acceleration at the boundaries of supernova remnants provides much the most persuasive theoretical basis for interpreting Galactic cosmic rays. The Fermi mechanism (Fermi, 1949) ensures that particles will repeatedly cross shock fronts and gain energy in each crossing, naturally producing a power-law distribution of particles. Although in reality many deviations arise due to e.g. nonlinear modification of the shock structure, magnetic field obliquity, geometric effects, time-dependence, and magnetic field amplification, the basic theory still holds.

In the rest frame of the shock, the material is streaming into the shock from upstream with velocity u, is compressed with a compression factor $r = u/u'$ and flows away from the shock with a speed u', reduced by the shock compression ratio. Particles in the high-energy tail of the particle distribution scatter off turbulent magnetic fields on both sides of the shock and may cross the shock many times. Each time they cross the shock, they are isotropized by scattering the medium on the other side and they gain energy of the order of $\Delta\ E/E \approx\ u/c$. These high energy particles may escape downstream with a certain probability, thus creating a power-law spectrum of accelerated particles: $N(E) \propto\ E^{-\Gamma}$, with $\Gamma \approx (r+2)/(r-1)$. In shocks with high Mach number, $r = 4$ and $\Gamma = 2$ (Hinton and Hofmann, 2009).

The crossing rate thus determines the energy gain rate,

$$\frac{1}{E}\left(\frac{\mathrm{d}E}{\mathrm{d}t}\right) \approx\ u^2/D \tag{2.2}$$

The maximum energy attainable depends on several factors, namely: the lifetime of the shock, synchrotron losses (in case of electrons) and the magnetic field. A small diffusion coefficient, D, implies that particles will stay close to the shock, an will have a bigger probability of crossing it again. The Bohm limit represents the slowest possible diffusion, with a mean free path of the order of the gyroradius. Assuming Bohm diffusion, protons may reach a maximum energy:

$$E_{\mathrm{max,p}} = \left(\frac{u}{1000\,\mathrm{km\ s^{-1}}}\right)^2 \left(\frac{t}{1\,\mathrm{kyr}}\right) \left(\frac{B}{1\,\mu\mathrm{G}}\right)\ \mathrm{TeV} \tag{2.3}$$

In contrast, synchrotron losses will limit the peak energy for electrons to:

$$E_{\mathrm{max,e}} = 100 \left(\frac{u}{1000\,\mathrm{km\ s^{-1}}}\right) \left(\frac{B}{1\,\mu\mathrm{G}}\right)^{-1/2}\ \mathrm{TeV} \tag{2.4}$$

As discussed above, diffusive shock acceleration transfers a significant fraction of the kinetic energy of the flow to high-energy protons. When the energy density of particles is comparable to that in the shock, nonlinear effects start to play a role. The overall compression factor may be increased beyond 4, but particles scattered upstream decelerate the inflowing material. Therefore, a precursor shock is created, and the compression factor of the main shock decreases below 4. Particles with small gyroradii compared to the separation between the two shocks experience a reduced acceleration due to the reduced compression factor. Instead, highest energy particles experience an acceleration

with $r > 4$. The expected result is a concave spectrum, with an index $\Gamma > 2$ at low energies, and Γ somewhat below 2 at high energies (Hinton and Hofmann, 2009).

When the gyroradius becomes of the order of the size of the shock, particles most probably escape. Therefore, magnetic field amplification is a critical issue in order to attain very-high energies. Evidence of magnetic field amplification was been found in *Chandra* X-ray images of supernova remnants: an extremely narrow smooth shell of synchrotron radiation at the outer edge of SN 1006 and Tycho's supernova remnant (Bamba et al., 2004; Hwang et al., 2002) revealed that the supernova remnant outer boundary is where relativistic electrons do gain their energy. The extreme thinness is consistent with a very short radiative cooling lifetime of $\sim 10^{13}$ eV electrons in a magnetic field of several hundred microgauss (Völk et al., 2005; Ballet, 2006). Such a magnetic field is two orders of magnitude more intense than the typical interstellar magnetic field.

The mechanism by which magnetic field amplification occurs is related to the propagation of cosmic rays themselves. Cosmic-ray streaming along magnetic field lines excite unstable growth of Alfvén waves. The wave growth is driven by the cosmic-ray pressure gradient and, on the other hand, the cosmic-ray diffusion coefficient is inversely proportional to the wave energy density (Schure et al., 2012). Therefore, if scattering is weak, cosmic rays escape a relatively large distance upstream, initiate instability growth far ahead of the shock and remedy the lack of a perturbed magnetic field able to scatter the cosmic rays. This regulates magnetic field ahead the shock precursor, where the instability has not had the opportunity to grow.

A distinction between scales shorter and longer than the gyroradius of the driving cosmic rays is to be made. Most rapid amplification can be achieved on short scales due to Bell instability (Bell, 2004). Fields on small scales explain the amplified fields observed at supernova remnant shocks, but they cannot by themselves provide the strong cosmic-ray scattering needed to accelerate particles to PeV energies. Cosmic rays in the precursor shock form filamentary structures due to self-generated magnetic fields. The cosmic-ray filamentation results in the growth of a long wavelength instability, and naturally couples the rapid non-linear amplification on small scales to larger length scales (Reville and Bell, 2012). Large-scale structures are especially important since cosmic rays are most effectively scattered by fields on this scale.

The discovery of megaparsec scale shocks (van Weeren et al., 2010) confirm that shocks are abundant in the Universe on all scales, and diffusive shock acceleration and magnetic field amplification are intrinsically linked. Therefore diffusive shock acceleration not only occurs in supernova remnants and this kind of objects may not be the only contributors to cosmic rays. On the Galactic scale, for instance, shocks around superbubbles have been discussed as accelerators (e.g. Ferrand, G. and Marcowith, A., 2010). Superbubbles are formed as a result of cumulative outflows from an assembly of massive stars, possibly enforced by the supernova explosions themselves. The outer region thus formed is a shock of large proportions that could potentially be a cosmic ray accelerator, or various multiple shocks can consecutively act to accelerate particles.

2.3 Non-thermal emission mechanisms in supernova remnants

Diffusive shock acceleration provides a population of accelerated particles (electrons and protons) that may interact with ambient magnetic fields, with ambient photon fields, or

with matter. The amount of relativistic particles increases with the time as the supernova remnant passes through its free expansion phase, and reaches a maximum when in the early stages of the Sedov phase. Correspondingly, the peak in gamma-ray luminosity typically appears some $10^3 - 10^4$ years after the supernova explosion. The processes that contribute to the broad band spectral energy distribution of supernova remnants are discussed below.

2.3.1 Interaction of accelerated particles with magnetic fields

In the presence of magnetic fields, relativistic charged particles emit synchrotron radiation. The classical treatment of the synchrotron radiation is valid under the assumption that

$$\frac{E_\mathrm{e}}{m_\mathrm{e}c^2}\frac{B}{B_\mathrm{cr}} \ll 1 \tag{2.5}$$

i.e. the magnetic field is much smaller than the critical value relevant to quantum effects, $B_\mathrm{cr} = m_\mathrm{e}^2 c^3/\mathrm{e}\hbar \approx 4.4\times10^{13}$ G (Aharonian, 2004). This limit is far from the magnetic field achieved in supernova remnant shocks, which attains the level of few hundred microgauss at most. Therefore, the energy of synchrotron photons is much lower than that of parent electrons, and no pair production is expected. Synchrotron radiation from protons can also be disregarded.

Accelerated electrons emitting synchrotron radiation produce a rising spectrum at low energies, with a maximum at an energy given by the expression (Longair, 1992):

$$E_\mathrm{peak} = 5\times10^{-9}\left(\frac{B_\perp}{1\,\mathrm{G}}\right)\gamma_\mathrm{e}^2\,\mathrm{eV} \tag{2.6}$$

The E_peak is, under usual conditions in supernova remnants, in the X-rays. After the maximum, the X-ray emission drops sharply.

Synchrotron losses slow down electrons and introduce a characteristic cooling time that can be expressed as (Gaisser et al., 1998):

$$t_\mathrm{syn} \approx 1.3\times10^{10}\left(\frac{B}{1\,\mu\mathrm{G}}\right)^{-2}\left(\frac{E}{1\,\mathrm{GeV}}\right)^{-1}\ \mathrm{years} \tag{2.7}$$

2.3.2 Interaction of accelerated particles with photon fields

Relativistic electrons can transfer part of their energy to low energy photons through inverse Compton scattering. The cross section of the process is determined by the Klein-Nishina formula, which depends on the product of the interacting photon and electron energies: $\kappa = E_\gamma E_\mathrm{e}$. Two regimes are to be distinguished:

Inverse Compton scattering in the Thomson regime

When $\kappa \ll m_\mathrm{e}^2c^4$, the cross-section of the inverse Compton scattering reduces to the Thomson cross-section, σ_T. Under these conditions the energy of the upscattered photon is $\epsilon_\gamma = E_\mathrm{e}^2/E_\gamma$, and only a small fraction of the energy of the electron is transferred to the photon. A power-law distribution of electrons, $\mathrm{d}N_\mathrm{e}/\mathrm{d}E_\mathrm{e} \propto E_\mathrm{e}^{-\Gamma}$, results in a power-law gamma-ray spectrum with photon index $\alpha = (\Gamma+1)/2$ (Ginzburg and Syrovatskii, 1964). Electrons transfer energy to photons at a rate given by (Aharonian, 2004):

$$\frac{\mathrm{d}E_\mathrm{e}}{\mathrm{d}t} = \frac{4}{3}\sigma_\mathrm{T}cn_\mathrm{ph}\frac{E_\mathrm{e}^2}{E_\gamma} \tag{2.8}$$

Therefore, the energy loss rate does not depend on the spectral energy distribution of target photons, but only on the total energy density of radiation, $u_{\rm r}$. The characteristic cooling time of electrons due to Thomson scattering can be expressed in a an equivalent way to equation 2.7:

$$t_{\rm IC} \approx 3 \times 10^8 \left(\frac{u_{\rm r}}{1\,{\rm eV\ cm^{-3}}} \right)^{-1} \left(\frac{E}{1\,{\rm GeV}} \right)^{-1} {\rm years} \tag{2.9}$$

Inverse Compton scattering in the Klein-Nishina regime

The Klein-Nishina formula when the electron is ultrarelativistic, $\kappa \gg m_{\rm e}^2 c^4$, can be approximated by:

$$\sigma_{\rm KN} = \pi\ r_{\rm e}^2 \frac{1}{\varepsilon} \left(\ln(2\varepsilon) + \frac{1}{2} \right)\ , \varepsilon = \frac{E_\gamma}{m_{\rm e} c^2} \tag{2.10}$$

The gamma-ray spectrum resulting from the upscattered photons grows sharply until a maximum energy, at which the photon gains a substantial fraction of the electron energy. In this case, the gamma-ray spectrum resulting from a power-law distribution of electrons is noticeably steeper, $\propto \epsilon_\gamma^{-\alpha}(\ln a + {\rm const})$, where $a = 4\epsilon_\gamma E_\gamma$ (Blumenthal and Gould, 1970). The electron cooling time depends on the energy distribution of the seed photon field. However, unlike in the Thomson regime, the cooling is slower the higher the energy of the target photons is and, consequently, the electron distribution gets harder with time.

Since ultrarelativistic electrons suffer large energy losses, there is a maximum energy gain, $\Delta E_{max} \approx 4\gamma_{\rm e}^2 E_\gamma$ for electron energies between 100 MeV and 10 GeV. This means that keV seed photons are upscattered to the GeV-TeV domain. When the upscattered photons are those emitted by synchrotron losses, the emission mechanism is known as synchrotron self-Compton. Other photon fields which can potentially interact with electrons are the cosmic microwave background or local sources of light, most often due to stars close to the accelerator.

2.3.3 Interaction of accelerated particles with matter

Sub-MeV and MeV and gamma rays are produced in the annihilation of electron-positron pairs and de-excitation of nuclei. To reach GeV and TeV energies, the most relevant processes are the interaction of charged particles with atoms (bremsstrahlung radiation) and the decay of subproducts of inelastic collisions of accelerated nucleons with matter.

Bremsstrahlung radiation

Bremsstrahlung radiation results from the deceleration of a charged particle when deflected by another charged particle. The discussion below is focused in the case of relativistic electrons interacting with a electrons bound to atoms, which generally yields energy up to the multi-GeV range. However, bremsstrahlung of ultra-high energy cosmic-ray nuclei exists and can reach TeV energies.

The energy loss rate of electrons in a medium is proportional to the energy of the particle itself (Longair, 1992):

$$-\left(\frac{{\rm d}E_{\rm e}}{{\rm d}t} \right) = \frac{E_{\rm e}}{\tau_{\rm br}} \tag{2.11}$$

Therefore, there is a characteristic time $\tau_{\rm br}$ after which the electron energy has been divided by e. In the relativistic case, $\tau_{\rm br}$ may be regarded as the time to cover a radiation

length, X_0/c. The radiation length depends on the ambient composition (via the atomic number Z) and the particle density, n:

$$\frac{1}{X_0} = 4\alpha\ r_{\rm e}^2 Z(Z+1)\frac{\ln(183Z^{-1/3})}{1+0.12(Z/82)^2}n \tag{2.12}$$

Therefore, the lifetime of electrons undergoing bremsstrahlung losses is inversely proportional to the medium density. In the case of interaction with hydrogen, the cooling time can be expressed in practical units as:

$$\tau_{\rm br} = 4\times10^7\left(\frac{n}{1\,{\rm cm}^{-3}}\right)^{-1}\ {\rm years} \tag{2.13}$$

This lifetime is energy independent, which implies that bremsstrahlung losses do not change the original electron spectrum. In case the electron spectrum follows a power law of index Γ, the spectrum of bremsstrahlung gamma rays is also a power law with the same index. However, when the electron energy is low enough, ionization dominates over bremsstrahlung. This happens at a critical energy $E_{\rm c} \approx 700 m_{\rm e}c^2 \approx 350\,{\rm MeV}$ in hydrogen. Since both ionization and bremsstrahlung have a loss rate proportional to n, the critical energy is independent of the density. On the other hand, above several MeV, the ionization loss rate does not depend on the electron energy. As a consequence, the steady state spectrum of electrons becomes harder, and correspondingly, the bremsstrahlung gamma-ray photons of several hundred MeV follow a power law of index $\Gamma - 1$.

The electron distribution is thus affected by several losses. At high energies, inverse Compton and synchrotron losses eventually dominate the cooling, depending on how compares the density of the ambient gas to the the energy density of the radiation and magnetic fields:

$$E_{\rm e} \geq 10\left(\frac{1{\rm eV/cm}^{-3}}{u_{\rm r}+B^2/8\pi}\right)\left(\frac{n}{1\,{\rm cm}^{-3}}\right)\ {\rm GeV} \tag{2.14}$$

The synchrotron and inverse Compton loss rates are proportional to the electron energy. Consequently, when these processes dominate, the electron spectrum becomes softer and bremsstrahlung gamma rays follow a power law of index $\Gamma + 1$.

Gamma rays from π^0 decay

The collision of a relativistic nucleus with ambient gas produces pions, kaons and hyperons that eventually decay to gamma rays. The channel providing the most effective conversion of kinetic energy from protons to gamma rays is the production of π^0 mesons, that immediately decay ($t_{\pi^0} = 8.4\times10^{-17}\,{\rm s}$) to two gamma rays. For the production of neutral pions the kinetic energy of protons must exceed $E_{\rm th} = 2m_\pi\ c^2(1+m_\pi/4m_{\rm p}) \approx 280\,{\rm MeV}$. The distinct feature of the π^0-decay gamma-ray spectrum is the maximum at $E_\gamma = m_\pi\ c^2 \approx 67.5\,{\rm MeV}$ independently of the energy distribution of the parent protons.

The proton-proton cross section can be approximated above 1 GeV by (Aharonian, 2004):

$$\sigma_{\rm pp} \approx 30\times[0.95+0.06\ln(E_{\rm kin}/1\,{\rm GeV})]\,{\rm mb} \tag{2.15}$$

The mild logarithmic dependency on energy permits the assumption of an average cross section at very-high energies of about 40 mb. Inelasticity causes protons to transfer, on average, $f \approx 0.5$ of their energy to the target nucleon in every interaction. Under these

conditions the characteristic cooling time of relativistic protons due to inelastic collisions is inversely proportional to the ambient density, and independent of the proton energy:

$$t_{\rm pp} = (n\sigma_{\rm pp} f c)^{-1} \approx 5.3 \times 10^7 \left(\frac{n}{1\,{\rm cm}^{-3}}\right)^{-1} \text{ years} \tag{2.16}$$

The number of secondary particles produced per interaction increases with energy. The $\sim 1/2$ of primary proton energy that is not lost by inelasticity is split between charged and neutral pions, as well as a small fraction of heavier hadrons. About 1/6 of the primary energy is carried by gamma rays produced in π^0 decays. The spectral energy distribution of these secondary gamma rays peaks at about 1/10 of the primary energy (Hinton and Hofmann, 2009). Since $t_{\rm pp}$ is almost energy independent above 1 GeV (where ionization losses are negligible), the information on the acceleration spectrum of protons is transferred to the gamma-ray spectrum: if the distribution of parent protons followed a power law, the gamma-ray distributions is a power law of the same index. However, since the secondary gamma rays have a broad spectrum, some spectral features (e.g. an exponential cutoff) are softened. In any case, this process certainly provides a unique channel of information about the hadronic component of cosmic rays.

2.4 Gamma-ray visibility of supernova remnants

Gamma rays from neutral pion decay are considered the best test for the contribution of supernova remnants to the cosmic-ray flux. If they are the sources of cosmic rays, a rough estimate of the hadronic gamma-ray flux level that can be expected from supernova remnants may be calculated as follows: approximately $W_{\rm CR}^{tot} \approx 10^{50}\,{\rm erg}$ of the typical energy release of $10^{51}\,{\rm erg}$ in a supernova explosion has to be converted into accelerated protons. If the proton distribution follows a power law of index 2 with a cutoff at an energy E_{cutoff} close to the knee, about $W_{\rm CR} \approx 7 \times 10^{48}\,{\rm erg}$ are contained in particles between the GeV and PeV. Taking into account the inelasticity factor f, and the cooling time for protons $t_{\rm pp}$ (equation 2.16), the gamma-ray flux at a distance d of the supernova remnant is of the order of (Gabici, 2012):

$$F_\gamma \approx \frac{W_{\rm CR} f}{4\pi\ d^2 t_{\rm pp}} \approx 10^{-11} \left(\frac{W_{\rm CR}^{tot}}{10^{50}\,{\rm erg}}\right) \left(\frac{n}{1\,{\rm cm}^{-3}}\right) \left(\frac{d}{1\,{\rm kpc}}\right)^2 \text{ erg cm}^{-2}\text{s}^{-1} \tag{2.17}$$

The energy spectrum of particles at a given time and distance from the source depends *i*) on the history of the injection, *ii*) the energy loss rate and *iii*) the particle type, and how is it affected by propagation through the interstellar medium. As mentioned in the previous section, the gamma-ray luminosity from neutral pion decay depends directly on the density of the target medium. This makes molecular clouds potential sources of gamma rays. Several configurations concerning the cloud/accelerator geometry are discussed below.

Cosmic-ray illumination of a molecular cloud

Following equation 2.17, a cloud of mass M at a distance d, illuminated by a Galactic cosmic rays produces a flux per unit of area and solid angle given by (Aharonian, 1991):

$$\Phi(E_\gamma > 1\,{\rm TeV}) = 1.6a \times 10^{-12} \left(\frac{M}{10^6 {\rm M}_\odot}\right) \left(\frac{d}{1\,{\rm kpc}}\right) \text{ cm}^{-2}\text{s}^{-1} \tag{2.18}$$

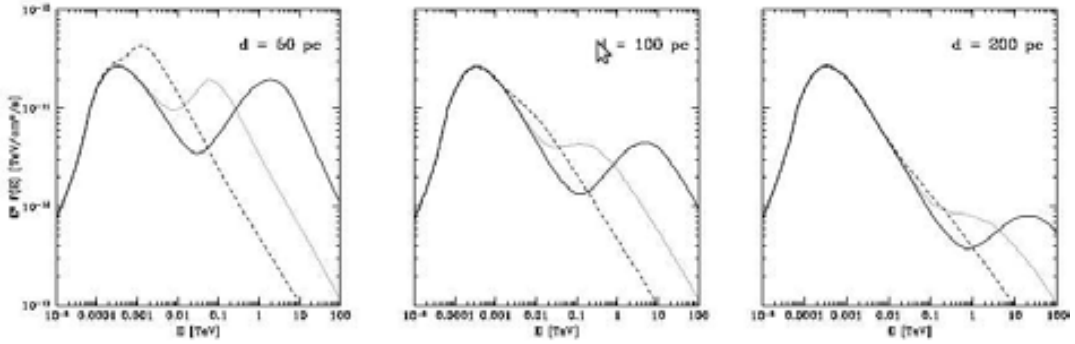

Figure 2.1: Expected gamma-ray emission from a molecular cloud of $10^5\,M_\odot$ located at a distance of 1 kpc. Different separations d between the cloud and the supernova remnant are considered. The solid, dotted, and dashed lines refers to the emission at a time 2000, 8000 and 32000 years after the explosion. Extracted from Gabici (2012).

Where the factor a accounts for possible deviations of the cosmic-ray intensity measured on Earth, for instance near a supernova remnant. The distance at which cosmic rays can isotropically diffuse away from their accelerator in a time t is $R \approx \sqrt{6D(E)t}$ (Aharonian and Atoyan, 1996). 10^4 years after the supernova explosion, cosmic rays diffusing away from their source are more intense than those from the Galactic background in region of 100 – 200 pc radius. Alternatively, if a cloud is at a distance R from the supernova remnant at a time t after the explosion, only protons with energy E_{min} such that $D(E_{min}) = R^2/(6t)$ reach the cloud. As a consequence, the gamma-ray spectrum of the cloud has a low energy cutoff, except for the fact that at GeV energies it is illuminated by the Galactic background cosmic rays. After a sufficiently long time of continuous injection, a steady state spectrum reproduces the spectrum of the source, except for the correction to the spectral index due to spallation (figure 2.1).

This process is very important in disambiguating the very-high-energy gamma-ray emission from supernova remnants near molecular clouds, since the only mechanism expected to produce significant flux in the cloud is neutral pion decay from proton-proton collisions. In addition, molecular clouds located near sources of cosmic rays are, so far, the only way to estimate variations of the diffusion coefficient, which is only known in Galactic average otherwise.

A supernova remnant embedded in a molecular cloud

In the case of an accelerator located at the center of a dense ($n \approx 100\,\mathrm{cm}^{-3}$) cloud, it is assumed that at any time t at which the cloud is observed, there are $W_{49} \sim 10^{49}\,\mathrm{erg}$ in particles diffusing through the cloud and escaping away. The gamma-ray flux above GeV energies is given by (Aharonian and Atoyan, 1996):

$$\Phi(E > E_\gamma) = 10^{-7} g_\alpha \left(\frac{W_{49}}{10^{49}\,\mathrm{erg}}\right) \left(\frac{d}{1\,\mathrm{kpc}}\right)^{-2} \left(\frac{n}{10^2\,\mathrm{cm}^{-3}}\right) E^{-\alpha+1} \eta_A\,\mathrm{cm}^{-2}\mathrm{s}^{-1} \qquad (2.19)$$

Where the factor g_α accounts for different propagation effects affecting different injection spectra, and ranges from $g_{\alpha=2.0} = 0.7$ to $g_{\alpha=2.4} = 1.27$. $\eta_A \approx 1.5$ corrects the contribution of nuclei heavier than that of hydrogen, which may have a somewhat harder injection spectrum. This expression is just a qualitative estimate, since the rapid slow-down of the shock reduces the effectiveness in accelerating particles. The expected spectrum from a

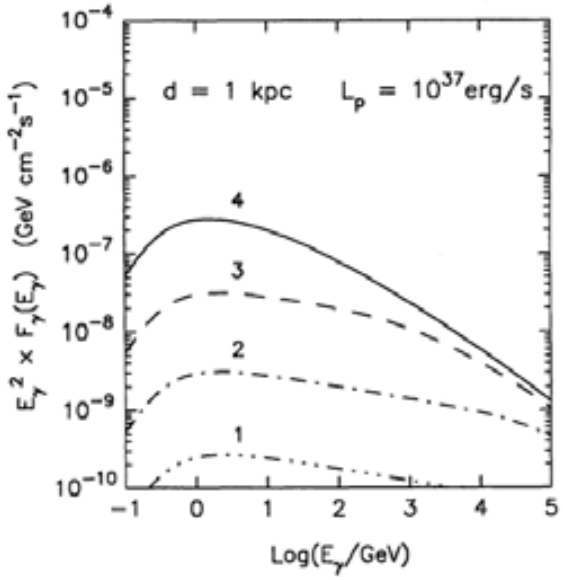

Figure 2.2: Expected gamma-ray emission from a continuous injection of cosmic rays at the center of a cloud of 20 pc radius with a density of 120 cm^{-3} located at a distance of 1 kpc. A power-law dependency of the diffusion coefficient is assumed, with index 0.5 and normalization at 10 GeV $D_{10} = 10^{26}\,\mathrm{cm}^2\mathrm{s}^{-1}$. Curves numbered 1, 2, 3, 4 correspond to fluxes after 10^2, 10^3, 10^4 and 10^5 years of continuous injection. Extracted from Aharonian and Atoyan (1996).

continuous injection of protons of $L_p = 10^{37}$ erg/s taking into account energy-dependent propagation and escape is shown in figure 2.2.

Reacceleration of pre-existing cosmic rays in a crushed cloud

Another possibility to obtain gamma-ray emission from molecular clouds is to consider those clouds that have been engulfed by the supernova blast wave. Blandford and Cowie (1982) showed that reacceleration of pre-existing cosmic-ray electrons results in enhanced synchrotron radiation capable of explaining radio intensity of evolved supernova remnants. The GeV gamma-ray emission from neutral pion decay is enhanced in the same manner: both the density and magnetic field are enhanced due to cooling of pre-existing dense clumps after shock passage (Uchiyama et al., 2010). The high-energy particles accelerated at the shock experience further heating due to adiabatic compression, as the gas density increases until the pressure is magnetically supported.

This model is of interest for supernova remnants like W51C, where there is evidence that the supernova shock has overtaken a cloud (section 6.1). Alternatively, the illumination of clouds described above is to be considered in case of clouds a few parsec apart of the blast wave, like in the case of the supernova remnant W28 and the TeV bright clouds south of it (Aharonian et al., 2008).

2.5 Selection of gamma-ray emitting supernova remnants

As discussed section 1.3, middle-age supernova remnants are plausible sources of cosmic rays up to the knee, since they had enough time for diffusively accelerate particles. On the other hand, the large ammount of material swept-up by the shock in the Sedov phase

may slow-down the shock. In this case, the maximum proton energy is not expected to reach PeV energies, but the gamma-ray luminosity is bigger provided the higher density of the medium (section 2.4). Moreover, it is reasonable to expect significant enhancement of the gamma-ray fluxes caused by the presence of high density environments, e.g. giant molecular clouds in the vicinity of a supernova remnant, not necessarily in touch with the blast wave. The detection of gamma rays from these systems pose strong indications about proton acceleration, especially for the case when the supernova remnant and the cloud are separated, so that the possibility of electrons diffussing so far away from the accelerator can be excluded.

Molecular clouds are the densest and coldest component of the interstellar medium. They are composed mainly by hydrogen in molecular form, with traces of other molecules. Complex ion-molecule chemistry can be enhanced thanks to fact that cosmic rays penetrate the medium, which is otherwise shielded against ionising radiation by dust grains. Vibrational transitions of the H_2 molecule that would be detected at infrared wavelengths are largely mitigated at the typical temperatures of 10 K. An important exception is shocked molecular hydrogen. In this case, H_2 acts as a coolant of the post-shock region, and emits infrared vibrational line emission (Hollenbach and McKee, 1989). Moreover, since the two nuclei are identical fermions, only one combination of nuclear spins is possible for each rotational level within an electronic state to preserve the antisymmetry of the overall wavefunction with respect to exchange of the nucleons. In the ground-electronic state, all the levels with odd J are nuclear triplet states (ortho-hydrogen), and all even J are singlet states (para-hydrogen). Only electric quadrupole transitions may occur, with selection rules $\Delta J = 0, \pm 2$ and the 0-0 transition forbiden. Therefore, at low temperature, rotational transitions are also inexistent (Shull and Beckwith, 1982).

In absence of shocks, the study of the molecular gas in the Galaxy must be mediated by tracer molecules. The most common of them is the CO molecule, which has several rotational transitions that can be excited by the thermodinamical conditions in molecular clouds. The typical wavelength of these transitions is 3.1 mm. The ratio with respect the hydrogen molecule, $CO/H_2 \approx 1.8 \times 10^{-4}$ (Estalella and Anglada, 2008), is variable across the Galaxy, and therefore introduces a systematical uncertainty in the conversion from CO line intensity to hydrogen mass. Moreover, the main isotopic variety, ^{12}CO, is optically thick, and thus cannot trace densities much higher than $\sim 100\,cm^{-3}$. For this purpose, ^{13}CO (with typical abundance of one molecule per 5×10^5 hydrogen molecules) is somewhat less opaque, but it neither can trace the densest clumps. In exceptional regions within molecular clouds, probably linked to embedded star-forming regions, the density can reach values of $10^3 - 10^4 cm^{-3}$. In this case, only the high-density tracer molecules such as NH_3, CS or HCO^+ are detectable. Their global abundace is minimal, but their formation is linked to such high densities, and therefore the contrast with respect to the background is very high.

Dame et al. (2001) presented a compilation of 37 surveys of CO emission covering the whole Galactic plane up to $4^\circ - 10^\circ$ in galactic latitude (depending on the longitude). A systematic approach to search for supernova remnants interacting with molecular clouds is the study of the 3-D spatial coincidence of local maxima of the CO distribution with the position of supernova remnants according to some catalogue (e.g. Green, 2009, Green catalogue hereafter). We did such a search for the 85 supernova remnants with some distance estimate in the Green catalogue: we computed the CO intensity as a function of the radial velocity in a box centered in the catalogue position of the test supernova remnant. The side of the box was defined by the angular size of the supernova remnant

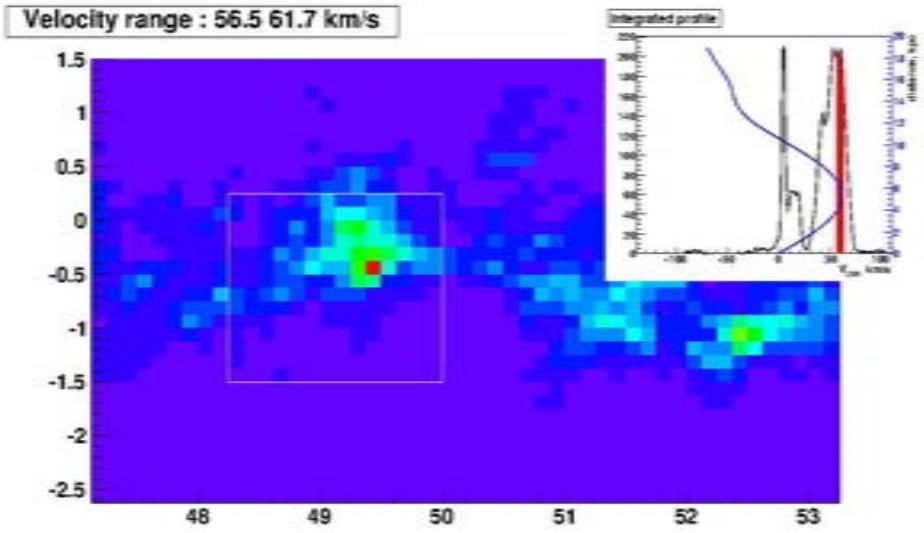

Figure 2.3: CO line emission map from Dame et al. (2001) in Galactic coordinates around the position of the supernova remnant W51C (marked with a white box) in the velocity range from 56.5 to 61.7 km s^{-1}. In the top-right box the integrated intensity profile (black curve, in arbitrary units) is shown. The peak at 59.15 km s^{-1} intersects the rotation curve (in blue) at 4.7 kpc (close distance) and 6.4 kpc (far distance), which are compatible with the distance of 5.5 kpc (Sato et al., 2010) to W51C within the uncertainty of the method. Other peaks at velocities of -87.75, 4.55, 52.65, 40.95 and 16.25 km s^{-1} are also detected along the line of sight, but have no physical relation with the supernova remnant.

plus 30 pc projected at the corresponding distance. The velocity of every intensity peak was converted to distance by means of the Galactic rotation curve. In figure 2.3 an example of such a search is shown for the supernova remnant W51C, where we found a CO intensity peak at 59.15 km s^{-1}. The result for this particular object is quite accurate, provided that higher resolution measurements by Carpenter and Sanders (1998) found that the W51 giant molecular cloud is located at a velocity of 61.0 km s^{-1} with a FWHM[1] of 8.9 km s^{-1}.

All in all, distances to supernova remnants are often poorly known. There is no direct method to evaluate the distance[2] and the only possible estimate comes from the association with another object whose distance can be measured, e.g. by parallax. Moreover, distances to molecular clumps are also inaccurate due to uncertainties in the Galactic rotation curve and possible proper motions deviating from the Galactic rotation. Therefore, we found more convenient a *one by one* approach taking into account high-resolution measurements in the literature. It was particularly useful the compilation of results regarding

[1]The large velocity dispersion is due to the fact that W51 is an exceptionally massive and extended cloud. More details are given in section 6.1.

[2]The old $\Sigma - D$ relation has been proven to be not a fundamental correlation, but an observational bias (Green, 2012).

supernova remnants interacting with molecular clouds by Bing Jiang (2011). From the list by Jiang, we selected objects with certain molecular cloud association and positive declination[3]. In addition, we added the Cygnus Loop, as we considered it could be an object particularly interestig for gamma-ray observations (discussed in chapter 5). The resulting observation summary is listed in table 2.1.

[3]The selection of northern supernova remnants is done because observations were done with the *Fermi*/LAT and the MAGIC telescoes. As discussed in section 3.2, the MAGIC telescopes are located in the northern hemisphere.

Table 2.1: Observation summary of the nine selected objects. Galactic coordinates (in degrees) are given, as well as a flag on whether the object is shell-like (S) or center-filled (C). Because *Fermi*/LAT operates in all-sky survey mode, data for all of them is available. We skipped the analysis of objects for with publications by the *Fermi*/LAT Collaboration at the time the study was started were already available (i.e. W44, W51C and IC443). Only two out of nine objects in the list are not detected. For the observation with the MAGIC telescopes, we participated in proposals to observe W51C, the Cygnus Loop, HB 21 and CTB 109. Among these, a source of very high energy gamma rays was detected in W51 (chapter 6.)

l	b	Type	Name	*Fermi*/LAT	MAGIC	references
34.7	-0.4	C	W44	detected	not observed	Abdo et al. (2010*d*); Uchiyama et al. (2012)
39.2	-0.3	C	3C396	missed	not observed	
41.1	-0.3	S	3C397	missed	not observed	
49.2	-0.7	S?	W51C	detected	detected	Abdo et al. (2009*a*), Chapter 6
54.4	-0.3	S	HC40	detected	not observed	Yang et al. (in preparation)
74.0	-8.5	S	Cygnus Loop	detected	missed	Katagiri et al. (2011), Chapter 5
89.0	+4.7	S	HB 21	detected	missed	Chapter 4, MAGIC Collaboration (in preparation)
109.1	-1.0	S	CTB 109	detected	missed	Castro et al. (2012); MAGIC Collaboration (in preparation)
189.1	+3.0	C	IC443	detected	detected	Abdo et al. (2010*e*); Albert et al. (2007*a*)

Chapter 3

Detectability of supernova remnants at high and very-high energies

To understand the physical processes behind supernova remnants, observations in the whole gamma-ray energy regime are desirable: The maximum energy flux is reached at energies above several hundred MeV, where Fermi/LAT provides unprecedented sensitivity. The maximum proton energy is proved by observations of gamma rays at several TeV. Bridging the highest Fermi/LAT energies and TeV energies, the MAGIC telescopes are a suitable instrument to complement observations in the whole gamma-ray domain.

The peak of the gamma-ray luminosity of supernova remnants interacting with molecular clouds is in the sub-GeV range. Therefore, the detection in this energy range allows a good estimation of the total gamma-ray luminosity and, consequently, the particle acceleration efficiency. The *Fermi* Large Area Telescope (*Fermi*/LAT) is particularly suitable for observations in this energy range. In the TeV range, gamma-ray signals from supernova remnants constrain the maximum energy attainable in these objects, up to energies just one order of magnitude below the knee. Imaging Atmospheric Cherenkov telescopes like MAGIC, H.E.S.S. or VERITAS are appropriate for this purpose. The sensitivity curves of current gamma-ray instruments are shown in figure 3.1. *Fermi*/LAT and MAGIC are the telsecopes used in this work. Detailed descriptions of these instruments are given in sections 3.1 and 3.2.

3.1 The *Fermi* Large Area telescope

The Large Area telescope (LAT) is an imaging, wide ($> 2\,\mathrm{sr}$) field-of-view (FoV) pair-conversion telescope sensitive to gamma-rays in the energy range from 20 MeV to 300 GeV. LAT is oboard the *Fermi* spacecraft, which was launched on June 11^{th} 2008 and started science operations by August 4^{th} 2008. *Fermi* hosts another instrument, the Gamma-ray Burst Monitor (GBM). The GBM is meant for transient phenomena in the energy range from 8 keV and 40 MeV (Meegan et al., 2009), an is not discussed in this work.

The *Fermi* satellite is in a 565 km altitude orbit with an inclination of 25.6°. The orbital period is about 96 minutes, and the orbital pole precesses about the celestial pole

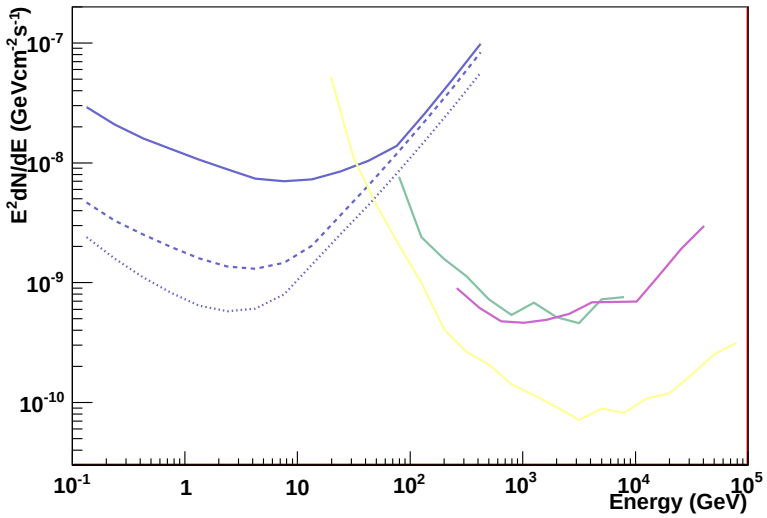

Figure 3.1: Sensitivity curves from MAGIC (Aleksić et al., 2011), green; H.E.S.S. (H.E.S.S. Collaboration, 2008), violet; and the future CTA observatory (Victor Stamatescu, private communication), yellow. The sensitivity of the Cherenkov telescopes is expressed as the minimum flux detectable with a statistical significance of 5σ after an exposure of 50 hours. In blue it is shown sensitivity of *Fermi*/LAT to point-like sources of spectral index $\Gamma = 2$, after three years of all-sky survey (Fermi-LAT Collaboration, 2012). The solid line is for sources in the galactic center; the dashed curve corresponds to sources at $(l, b) = (0, 30°)$; and the dotted curve corresponds for sources at $(l, b) = (0, 90°)$.

every 53.4 days. The 15% of the time, the spacecraft is inside the South Atlantic Anomaly (SAA), which prevents de datataking. In the standard sky-survey mode (in which the *Fermi*/LAT has spent 95% of the mission time), the spacecraft rocks N and S about the orbital plane on alternate orbits. The rocking angle was set to $\pm 50°$ in September 3^{rd} 2009, although it was 35° before. In addition, the spacecraft completes a full azimutal rotation in every orbit. This is done (*i*) for the need to maintain the solar panles oriented toward the Sun, and the radiators away from the Sun, but also because (*ii*) this way the LAT boresight crosses a range of declinations $\pm 25.6°$ relative to the rocking angle, thus covering the whole sky every two orbits.

The LAT sensitivity depends on the sky coordinates (mainly galactic latitude) and the energy (figure 3.1). As a figure of merit, at 1 GeV the LAT has a sensitivity one order of magnitude better than its predecessor, the Energetic Gamma-Ray Emission Telescope (EGRET Thompson et al., 1993). The Point Spread Function[1], ranges from 3.3° at 100 MeV to 0.1° above 1 GeV (figure 3.2). The point-like source location accuracy is in the worst case, i.e. very soft spectrum $\Gamma = 3$, 0.27°. For spectral indices of $\Gamma = 2$ or harder, the point-like sources can be located with a precision of 0.07° to 0.09° depending on the Galactic latitude. The energy resolution is always better than 25%, achieving the greatest performance at a few GeV with resolution of about 8% (figure 3.3).

The LAT is composed by 16 tracker/converters plus calorimeter modules are assembled in a structure of 4×4 *towers* enclosed by an anticoincidence detector. In addition to these systems, a trigger and data acquisition system selects and records the most likely

[1]defined as the 68% containment angle for normally incident gamma rays.

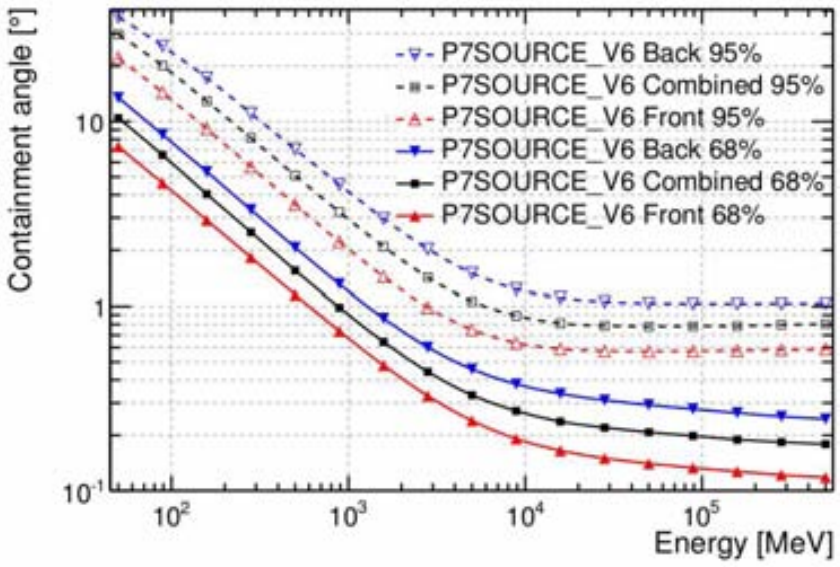

Figure 3.2: Representation of the PSF of the LAT as the 68% and 95% containment angles as a function of the energy for the `P7SOURCE_V6` event class. Curves for the front (red) and the back (blue) tracker/converters are shown, as well as the combination of the two (black). Extracted from Fermi-LAT Collaboration (2012).

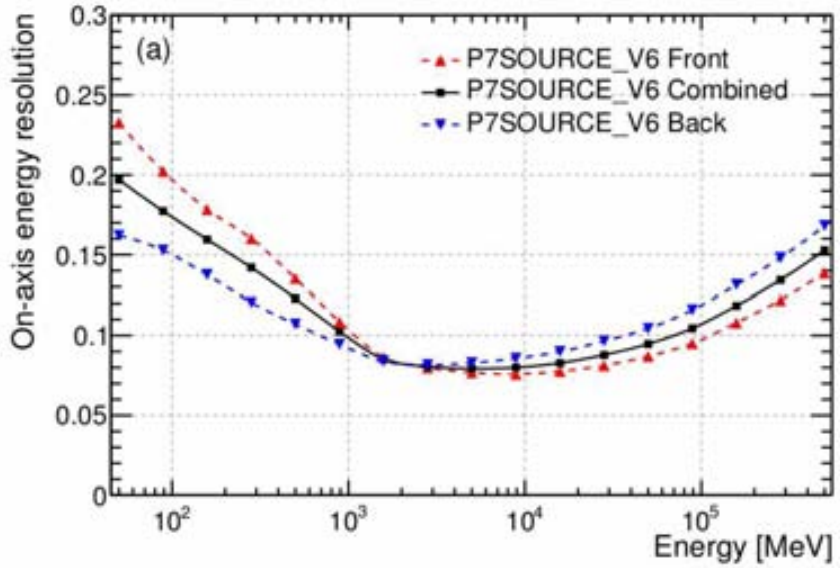

Figure 3.3: Energy resolution of the LAT as a function of the energy for on-axis photons of the `P7SOURCE_V6` event class. Curves for the front (red) and the back (blue) tracker/converters are shown, as well as the combination of the two (black). Extracted from Fermi-LAT Collaboration (2012).

gamma-ray candidate events prior to transmission to the ground. The reconstruction of the tracks and calorimetry of e^+e^- pairs permits an estimation of the energy of the primary particle, as well as its incidence direction. Accurate timestamps for the events are obtained from the Global Positioning System (GPS), which also provides information of the *Fermi* spacecraft.

The tracker/converter consists of 18 layers of paired Silicon Strip Detector (SSD) with interleaved tungsten fouls (Atwood et al., 2007). The outermost 12 paired layers are designed to minimize the effects of multiple scattering by minimizing the separation of the converter foils from the following SSD planes. This section is known as the *front* converter. The next 4 layers are known as the *back* detector, and are similar similar to the front detector, except that tungsten converters are 6 times thicker. This choice balances two different, conflicting requirements: simultaneously obtaining a good angular resolution and a large conversion probability. About the same number of gamma rays are converted in the fron and in the back detector.

The calorimeters are composed of 8.6 radiation lengths of CsI(Tl) scintillation crystals stacked in 8 layers. Since each layer is composed of 12 crystal logs, 3D imaging capability is achieved. Each log is read out via four photodiodes (two at each end). The two photodiodes at each end of a crystal log are of different sizes: *large* ones are good for low energy ($< 1\,\mathrm{GeV}$ per crystal) events, whereas small ones are sensitive to high energy ($< 70\,\mathrm{GeV}$ per crystal) events. In addition, both photodiodes are connected to two different preamplifiers whose output drives a slow-shaping amplifier for spectroscopy, and a fast-shaping amplifier for trigger discrimination. The output of each fast shaper is connected to two different gains, which –combined with the two kninds of photodiode– provides a broad dynamic range, from $< 2\,\mathrm{MeV}$ to $70\,\mathrm{GeV}$ per crystal, which translates in the broad dynamic range of the LAT as a whole.

The recording of gamma-ray events is a three-step procedure:

1. *hardware trigger request*: the LAT detects some trace of particle interaction and starts the triggering process.

2. *hardware trigger accept*: if the event generates an acceptable trigger pattern, then it is read out and passed to the on-board filter.

3. *on-board filter*: a hierarchical sequence of veto tests is performed, with the least CPU-intensive tests first. An event rate of 350 Hz is recorded, which allows to cope with downlink bandwidth limitations.

Event-wise information is transmitted to the ground, and subsequently analyzed at the LAT Instrument Science Operations Center, in Stanford. About a 0.4% of the recorded events pass the quality cuts and are flagged as gamma-rays (Fermi-LAT Collaboration, 2012).

3.1.1 *Fermi*/LAT data analysis

One year after the launch of *Fermi*/LAT, the data became publicly available via the *Fermi* Science Support Center (FSSC[2]) along with a specific software package to analyze it (the so-called *ScienceTools*). A spatial and spectral model of the Galactic diffuse gamma-ray emission, and a spectral template for the isotropic gamma-ray emission are also included

[2] `http://fermi.gsfc.nasa.gov/ssc`

in the ScienceTools. The isotropic gamma-ray emission accounts for the extragalactic background plus a contribution accounting for misclassified charged cosmic rays.

A critical component of the analysis tools is the parametrized representations of instrument performance, which are encoded in instrument response functions (IRFs). The instrument response is factorized in three parts:

1. The effective area, $A_{eff}(E, \hat{v}, s)$, which depends on the energy E, the incidence direction $\hat{v}$ and the efficiency of a given event selection, s.

2. The point spread function (PSF), $P(\hat{v}'; E, \hat{v}, s)$, or probability density to reconstruct an incident direction $\hat{v}'$ for a gamma ray with energy E and direction $\hat{v}$.

3. The energy dispersion, $D(E'; E, \hat{v}, s)$, meaning the probability density to measure an energy E' from an event of energy E from the direction $\hat{v}$.

The IRFs are meant to be used in a likelihood analysis as described in Mattox et al. (1996). Given a distribution of gamma-ray events of energy E and incidence direction $\hat{p}$, $S(E, \hat{p})$, the observed distribution of gamma rays is

$$M(E', \hat{p}', s) = \iiint S(E, \hat{p})\ A_{eff}(E, \hat{v}, s)\ P(\hat{v}'; E, \hat{v}, s)\ D(E'; E, \hat{v}, s)\, \mathrm{d}E\mathrm{d}\Omega\mathrm{d}t \quad (3.1)$$

Where the integrals are over the time range of interest, the solid angle in the LAT reference frame, and the whole energy range of the LAT. The IRFs can change markedly across the LAT FoV. Therefore, it is convenient to compute the exposure for any given energy an direction in the sky:

$$\mathcal{E}(E, \hat{p}, s) = \int A_{eff}(E, \hat{v}, s)\ t_{obs}(\hat{v}; \hat{p})\, \mathrm{d}\Omega \quad (3.2)$$

The IRFs were initially estimated from Monte Carlo simulations of the interaction of gamma rays with the LAT. Data calibrated like this was known as `Pass 6`. After two years of data taking, the IRFs were recalibrated using the LAT dataset as calibration data (Fermi-LAT Collaboration, 2012). In this way, unanticipated features of the LAT data were taken into account in the analysis. Particular attention was paid to increasing effective area below 300 MeV, where the impact of unexpected on-orbit effects was large. Data calibrated this way (dubbed `Pass 7`) were released in August 2011. This work makes use of the `Pass 7` data, which takes into account the latest improvements.

Data were analyzed with the version v9r27p1 of the science tools. We selected class 2 events in the energy range between 100 MeV and 100 GeV in a region of interest (ROI, i.e. the sky region whose LAT photon events are considered) defined as circle of 10° radius. We applied a set of quality cuts, including the requirement for the spacecraft to be in normal operation mode (LAT_CONFIG==1), data to be flagged as good quality (DATA_QUAL==1), and a cut on the rocking angle of the spacecraft (ABS(ROCK_ANGLE)< 52°). In addition, we applied a zenith angle cut of 100° in order to prevent event contamination from the Earth limb. Data were binned in sky coordinates with the `gtbin` tool, using square bins of 0.125° side. We refer later to the two-dimensional histograms resulting from `gtbin` as *count maps*.

For the study of the morphological and spectral properties, we performed a three-dimensional (two spatial dimensions plus the energy) maximum likelihood analysis, using the standard `gtlike` tool. In this method, the likelihood is computed for different models

defined by the position and morphology of the sources producing gamma rays in the ROI. For each source, a different spectral shape may be assumed, and the spectral parameters are left free in the likelihood maximization. Our starting point consists of the standard galactic and extragalactic diffuse emission models provided in the ScienceTools, plus the point-like sources in the second *Fermi*/LAT source catalog (2FGL Nolan et al., 2012) lying up to 15° away of the ROI center. We call the *null hypothesis* a model where the 2FGL sources potentialy related to the source of interest are removed. Next, we compare the maximum likelihood obtained with the null hypothesis to those of several models that include various templates of the gamma-ray emission of the object of interest. For each model, the goodness of the likelihood fit is estimated by means of a test statistic (TS) defined as

$$\mathrm{TS} = -2\log(\mathcal{L}_0/\mathcal{L}), \tag{3.3}$$

where $\mathcal{L}_0$ and $\mathcal{L}$ are the likelihood of the null hypothesis and the tested models respectively. Since TS is a likelihood ratio of two nested models, it asymptotically follows a χ^2 distribution with a number of degrees of freedom equal to the extra number of parameters of the test hypothesis with respect to the null one (Abdo et al., 2010*a*). Despite some caveats (Protassov et al., 2002), it is normally accepted TS = 25 as a detection threshold of a source with two spectral parameters (flux normalization and spectral index), which corresponds to a statistical significance of 4.6 sigma. In all cases, `gtlike` is run in a two-step procedure: first allowing a loose tolerance up to 10% in the fit parameters and using the `MINUIT` method and, second, using the output of `MINUIT` as the initial value for a refitting of the model parameters with a tighter requirement of 0.1% tolerance and using the `NEWMINUIT` method. The output of `gtlike` allows us to generate *synthetic maps* with the expected source shape and brightness, given the model best-fit parameters. These synthetic maps can be subtracted from the counts maps in order to visualize the disagreements between the real data and its parametrization, in the form of a *residuals map*. We then divide, pixel by pixel, the residuals map by the square root of the number of counts in the synthetic map, thus obtaining a measure of the significance of the disagreement in every pixel, which we will call the *signal-to-noise ratio, S/N, map*.

We set up an analysis pipeline through which we processed the publicly available data of the supernova remnants listed in table 2.1 except W51C (Abdo et al., 2009*a*), W44 (Abdo et al., 2010*d*) and IC443 (Abdo et al., 2010*e*), for which detailed analyses by the *Fermi*/LAT Collaboration were already available at the start of this work. Of the six remaining objects, four were detected (Cygnus Loop, HB 21, CTB 109, and HC40) and two were missed (3C396 and 3C397). More details on HB 21 and the Cygnus Loop are given in chapter 4 and chapter 5, respectively. A comprehensive analysis on CTB 109 was recently published in Castro et al. (2012), whereas we foresee to publish the results on HC in Yang et al. (in preparation).

3.2 The MAGIC telescopes

MAGIC consists of two Imaging Atmospheric Cherenkov Telescopes located at the Roque de los Muchachos observatory, on La Palma island, Spain (28°46′ N, 17°53′ W), 2200 m above the sea level. MAGIC has the lowest trigger threshold of all operating IACTs, enabling it to observe gamma rays between 50 GeV and several tens of TeV. Therefore, MAGIC bridges the sensitivity gap between the highest photon energies detectable by *Fermi*/LAT and the ground-based instruments. A single telescope, MAGIC I, was op-

erated since the beginning of the experiment in 2004 until summer 2009, when MAGIC II was completed. The stereo system operated regularly until summer 2011, when an upgrade of the old MAGIC I camera and the electronics of both telescopes was initiated. Despite some months of operation with an intermediate configuration (the old MAGIC I camera with the new electronics), the completion of the upgrade has been completed in summer 2012. The upgraded MAGIC telescopes are starting the comissioning phase by early fall 2012, and are expected to take data regularly by November 1^{st} 2012. In this section we focus on the MAGIC telescopes as they were in the period between fall 2009 and summer 2011, when the data presented in Chapters 5 and 6 were taken.

Structure and reflector The telescopes are mounted on alt-azimuthal frames driven by two synchronous motors per telescope (Bretz et al., 2009). The frame lies on a 20 m diameter circular rail. The structure of the MAGIC telescopes is a light-weight (5.5 ton), stiff carbon fiber-epoxy structure, which allows fast reaction to transient events such as gamma-ray bursts. The reflector of the MAGIC telescopes consists of a 17 m diameter parabolic dish which focusses light from extensive air showers on the pixelized camera. The ratio of the focal length to the diameter of the reflector is $F/D = 1$. The large mirror surface is one of the features allowing the low threshold. In addition, the parabolic shape of the reflector ensures the preservation the temporal structure of the light flashes reflected on the focal plane, which permits to extract timing information from the recorded images (Aliu et al., 2009). The weight of the camera[3] causes some deformation of the structure which could affect the optical properties. However, the reflector is tessellated in 247 individually movable, 1 m^2 mirror panels[4] covering a total surface of 234 m^2 (Doro et al., 2008). The mechanical deformation is compensated by active mirror control (AMC), which automatically readjusts the mirror facets to recover the minimum possible optical PSF. Moreover, the pointing of the telescopes is continuously corrected by means of observations of guide stars in the FoV, and corrected if the catalog position of the identified stars differs from the nominal position of the telescopes.

Camera The performance of the cameras is crytical for the sensitivity of the telescopes. Both cameras are located in the focal plane of the telescopes, sustended by a tubular mast and several stabilizing steel cables anchored to the structure. Pixels consist of photomultiplier tubes (PMTs) of high quantum efficiency, protected behind a plexiglas window. As mentioned above, the MAGIC I and MAGIC II cameras were different until a clone of the MAGIC II camera was installed in MAGIC I in summer 2012.

The MAGIC I camera operating prior to the upgrade had an hexagonal shape with 3.6° FoV. It was equiped with 576 PMTs of two different kinds. The inner 396 PMTs had a diameter of 1 inch, which implied a 0.1° FoV. All together, the inner pixels covered a circle of 1.2° radius in the sky, which comprised the trigger region. The remaining 180 PMTs were bigger, with 0.2° FoV each, and were displayed in 6 double rows at the hexagonal outer edges of the camera. In order to minimize the losses into the death space between the round PMTs, hex-to-round light guides were used. The PMTs had only 6 dynodes and run at a relatively low gain (20000 to 40000) to prevent high anode currents during moonlight observations that could damage the devices. The poor timing performance that this low gain could produce was compensated with fast, high gain amplifiers at

[3]MAGIC I camera weighted about 672 kg, and MAGIC II camera about 885 kg during the considered period.

[4]The mirror panels at the edges of the reflector are smaller than 1 m^2.

the base of the PMTs. Instead, the MAGIC II camera (as well as the new MAGIC I camera) has a circular shape with 3.5° FoV and is uniformly equiped with 1039 PMTs similar to the inner ones in MAGIC I. The camera has a modular design, with PMTs grouped in 169 clusters, of which the 95 located in the inner 2.5° define the trigger region (Borla Tridon et al., 2009).

Calibration system The calibration system consists of a set of LEDs (in MAGIC I[5]) or a laser (in MAGIC II) that provide light pulses of different wavelength and intensity. On the one hand, the calibration system permits the adjustment of the high-voltage in the PMTs so that their gain is uniform throughout the camera. On the other hand, the camera is flashed with calibration signals every few seconds in order to monitor the behavior of the whole electronic chain during the data taking.

Readout and data acquisition systems Electric pulses at the base of the PMTs are converted into optical pulses using Vertical-Cavity Surface-Emitting Lasers (VCSELs). Optical signal are sent through optical fibers 80 m away to a building (affectionately known as the *Counting House*) hosting the rest of the electronics and the operations center. In the Counting House, the optical signals are split into two branches and are back-converted into electronic signals in the *receiver boards*. One branch goes to the trigger system, whereas the other is delayed (in order to wait for the trigger response) is sent to the data acquisition system (DAQ). If the trigger response is positive the DAQ digitizes the electronic signal into *raw* data files.

The digitizing hardware was different in MAGIC I and in MAGIC II. MAGIC I featured an ultra-fast Flash Analogical to Digital Converter (FADC) with fiber optic multiplexing (MUX) which sampled the signals with a resolution of 2 Gsamples/s (Goebel et al., 2007). In MAGIC II the sampling speed was the same, but the almost double number of pixels required a more compact, lower cost set up. This was achieved by means of the MONSTER boards (Tescaro et al., 2009), which are able to process 24 pixels each (instead of the 8 pixels per board of the MAGIC I receivers). In the MONSTER boards the digitalization was performed through the so-called *Domino Ring Sampler 2* (DRS2) chip. Each DRS2 chip hosts 10 input channels, and each channel charges a chain of 1024 capacitors organized as a ring buffer. The DRS2 chip is highly non-linear, is temperature sensitive, and has a dead time of about 10%. Therefore, a calibration of the response of the chip had to be performed about twice per night. Operation of the DRS2 required the use of general purpose motherboards (called PULSAR boards[6]), which hosted 4 custom *mezzanine* boards, on which 2 DRS2 chips were mounted. In total, 80 channels were read out from each PULSAR. Three special PULSAR boards completed the system: a first board, called *digital*, sampled the trigger signal and measured its arrival time; then another board, called *analog*, reacted to the trigger signals and read out the region of interest within the 1024 capacitors of each chip; and finally, the so-called *busy* board, provided a busy signal that inhibited the trigger while the system was processing an event. After the upgrade, both telescopes are equiped with a similar readout to that of MAGIC II, but the DRS2 have been substituted by their evolution DRS4, which are more linear and better performant.

[5]In the pre-upgrade configuration.

[6]PULSAR boards were initially developed for high-energy physics experiments by the University of Chicago.

Trigger The trigger system has the purpose to discriminate signals from Extensive Air Showers (EAS) from fluctuations of the Night Sky Background (NSB). The trigger criterium is that fast (< 5 ns) pulses should appead in a compact region of the camera above a certain intensity. The trigger is composed of four levels: (*i*) Level 0 (L0) trigger is hosted in the receiver boards, and issues a digital signal for each pixel which is above a discriminator threshold (DT). The DT are programable from the central control so that a stable rate is sustained under variable light conditions; (*ii*) Digital signals are sent to a Level 1 trigger (L1), which evaluates the *compactness* of the signal by means of time-coincidence of L0 signals within 19 overalping hexagonal macrocells of pixels in the trigger region. The topology of the coincidence can be selected to, at least, two next-neighboring pixels (2NN), or 3NN, or 4NN; (*iii*) The Level 3 (L3, or stereo) trigger seeks coincidence of L1 triggers on both telescopes, and rejects individual telescope L1 triggers (which are most probably due to NSB). (*iv*) A Level 2 (L2) trigger may be programed to produce some early background rejection of L1 or L3 events (Paoletti et al., 2007). In the present configuration it has no decisional power, but is used only for scaling and merging the signals from L1 and L3 with those generated when calibration pulses are fired, and send them to the readout system.

The trigger is equivalent in MAGIC I and MAGIC II. However, the number of pixels participating in the trigger decision was bigger in MAGIC II. As discussed above, pixels in the inner 2.5° of the FoV of MAGIC II triggered, whereas in MAGIC I only the inner 1.2° contributed. This translated in a somewhat bigger individual telescope trigger rate in MAGIC II. In typical observations the telescopes were set to trigger 3NN deep in the NSB, at L1 rates of about 10 kHz for MAGIC I and 15 kHz for MAGIC II. The resulting L3 rate was 150-200 Hz.

MAGIC I was also capable to operate with an alternative trigger, known as *sum trigger* (Rissi et al., 2009), which permited to lower the threshold of the system down to 25 GeV, while the trigger area was slightly reduced. The sum trigger was specially suitable for the observation of pulsars with a single telescope. The implementation of a stereo sum trigger for the upgraded MAGIC telescopes is foreseen for the winter 2012-2013.

3.2.1 Operation of the telescopes

Observations with the MAGIC telescopes are carried out either in *tracking* or in *wobble* mode. The observation mode determines the background estimation procedure. In the tracking (or ON/OFF) mode, the telescopes track the source on axis. Additional data for background estimation are taken by tracking a region of the sky where no gamma-ray source is expected, under similar conditions regarding the stellar field and zenith angle. However, most of the MAGIC observations are carried out in wobble mode (Fomin et al., 1994), where the telescopes track at least two sky positions slightly offset from the source of interest. In this mode, the region of the camera containing the source rotates (due to the azimuth change) during the observation. The typical setup during the pre-upgrade period consisted of observations 0.4° off the source along the right ascension axis, where the two wobble positions were swaped every 20 minutes. One or more regions of the camera free of gamma-ray emission are used for background estimation. The wobble mode configuration was recently modified, so that now four positions are observed: two of them displaced along the right ascension axis, and the other two along the declination axis.

In addition to the data runs, recording mainly events triggered extensive air showers,

two more kinds of events can be recorded. Calibration runs contain triggers from the calibration system. These are mainly LED or laser flashes that illuminate the whole camera with high intensity and uniformly. In addition, pedestal runs contain random triggers with a very low probability of containing shower events. Both calibration and pedestal runs are used in the calibration described in section 3.2.2.

3.2.2 MAGIC data analysis

The MAGIC Analysis and Reconstruction Software (MARS) is a specific ROOT-based[7] package for the analysis of the MAGIC data (Moralejo et al., 2009). The phylosophy of MARS is to create a software chain, where each program produces the input for the subsequent step. The final data product consists of a list of selected events that can be used for the calculation of the source spectrum or the sky distribution of the events, among other high-level products. The analysis chain relies heavily on Monte Carlo simulations for the background rejection. Thus, before describing the analysis chain we will introduce the Monte Carlo production chain.

The shape of the simulated gamma-ray source can be adjusted to be either point-like or diffuse. The spectral shape is always a power law. The Monte Carlo production is divided in three stages (Majumdar et al., 2005):

Simulation of extensive air showers The development of EAS unleashed by gamma ray are simulated by the CORSIKA 6.019 program, via the `EGS4` algorithm (Heck et al., 1998). The Cherenkov photons produced in the simulated showers that reach the ground are stored to disk.

Simulation of the propagation of Cherenkov photons A dedicated program, dubbed `reflector`, accounts for the Cherenkov light absorption and scattering in the atmosphere, including Rayleigh scattering and Mie scattering. In a second stage, `reflector` simulates the response of the telescope mirrors, and yields the distribution of Cherenkov photons on the camera plane. The output of `reflector` also contains the arrival times of the reflected Cherenkov photons, which will be used later in the analysis.

Simulation of the telescope electronics A third program, dubbed `camera`, smears the distribution of Cherenkov photons according to the optical PSF of the telescope. Next, it simulates the response of the PMTs given a certain level of NSB, and simulates the trigger and DAQ process.

The output of `camera` has the same format as the real data files, and thus can enter the analysis chain as real data would do. The steps for the processing are the following:

Conversion to ROOT format A program dubbed `merpp` converts the raw data files (or the camera files) to ROOT format and includes trees with the information of the telescopes subsystems. ROOT is a compressed format, and eases access to different kinds of data stored in a single file, from pixel charges recorded by the DAQ to air temperature recorded by the telescope weather station.

[7] ROOT is a C++ data analysis software developed at CERN. It is available through `http://root.cern.ch`.

Calibration For the stereo data before the upgrade, the program `callisto` reads raw data files composed of time series of the digitised charge values for each pixel and every triggered event. The recorded signals are sampled in 80 slices by the 2 GSamples/s FADC. The subsequent steps were different, depending on the telescope:

- In MAGIC I, the MUX DAQ stored only 50 samples, since the 15 initial and the 15 final samples of an event contained switching noise. After subtracting the pedestal offset (thanks to dedicated pedestal runs), the Cherenkov pulses are extracted from each pixel by integrating a cubic spline around the peak of the digitised signal. From the signal extraction, the arrival time is computed as the position of the rising edge of the spline at half maximum.
- In MAGIC II, a calibration of the non-linear response of the DRS2 chip is applied first. After subtracting the pedestal offset, the signal peak is found as the window yielding the maximum integral content of a number of consecutive FADC slices. The signal arrival time is defined as the average of the FADC slices time, weighted by the charge content of each of them

After the signal extraction, the F-factor method (Mirzoyan, 1997) is applied to convert DAQ arbitrary units into photoelectrons (phe), which are proportional to the number of Cherenkov photons. The proportionality constant is obtained from calibration events, i.e. short (~ 2 ns), intense light pulses generated by the calibration system. The number of phe per calibration event in every pixel follows a Poissonian distribution with mean N. The measured charge in FADC counts has mean $\langle Q \rangle$ and root mean square (RMS) σ, which is wider than the Poissonian expectation due to the multiplication process of electrons in the PMT dynodes. The relative widths of the two distributions are thus related by the F-factor:

$$F \cdot \frac{1}{\sqrt{N}} = \frac{\sigma}{\langle Q \rangle} \tag{3.4}$$

The F-factor is measurable in the laboratory. Also the electronic chain contributes to the broadening of the measured charge distribution, but its effect can be neglected in comparison to the contribution from the PMTs. Then, the conversion factor C from FADC counts to phe is:

$$C = \frac{N}{\langle Q \rangle} = F^2 \frac{\langle Q \rangle}{\sigma^2} \tag{3.5}$$

The conversion factor changes during the night due to variations in the very unstable response of the VCSELs. To compensate for these variations, calibration events are interleaved at a rate of 25 Hz during the normal recording of EAS. If some isolated pixel cannot be used due to hardware problems, their signals are interpolated by averaging the value of the signal in the neighboring pixels. After the upgrade of the readout system of both telescopes to DRS4 chips, the program `sorcerer` has been developed and optimized to cope with the new requirements posed by the new hardware.

Image cleaning After the calibration, data files contain the charge (figure 3.4a) and the arrival time (figure 3.4b) of the signal extracted in every pixel and every event. The program `star` reconstructs the images produced by EAS. At an initial step, pixels containing information about the showers are identified and the rest are rejected (figure 3.4c). Two charge thresholds are defined to discriminate between *core* (q_{core}) and *boundary* ($q_{boundary} < q_{core}$) pixels of each image. A core pixel is requested to have at least one

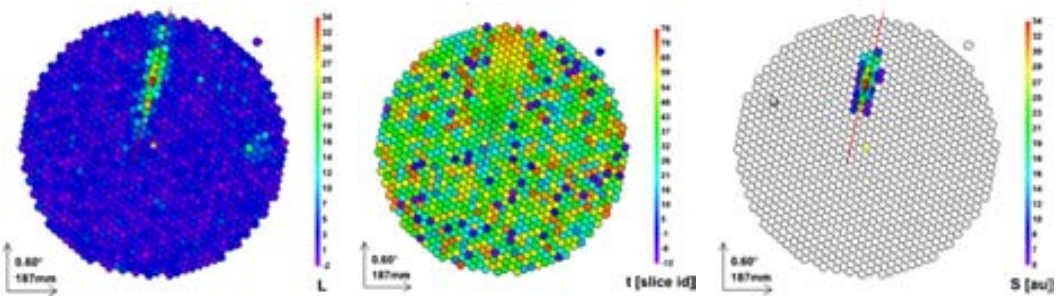

(a) Charge distribution (b) Arrival times (c) Cleaned image

Figure 3.4: Example of image cleaning procedure of an event recorded in MAGIC II. (a) shows the pixel charge of each pixel, and (b) the arrival time. After cleaning with standard requirements (table 3.1) only few pixels survive (c). Taken from Zanin (2011).

Table 3.1: Image cleaning parameters of both telescopes.

telescope	q_{core} (phe)	$q_{boundary}$ (phe)	δt (ns)	Δt (ns)
MAGIC I	6	3	4.5	1.5
MAGIC II	9	4.5	4.5	1.5

neighbor pixel fulfilling the condition. This second requirement avoids that isolated pixels with large charge survive the image cleaning. Boundary pixels must have at least one core neighbor. The two charged thresholds are optimized so that they are low enough to include very dim showers (of events below 100 GeV) without including too much noise from NSB that would distort the image. In addition, a constraints in the signal arrival time are applied: (i) the arrival time of a single core pixel must not differ from the average arrival times of all core pixels by more than a fixed offset, δt; and (ii), the difference between the arrival time of a boundary pixel and that of its core neighbor must not exceed a fixed time difference, Δt (Aliu et al., 2009). The image cleaning parameters of both telescopes optimized for dark conditions are summarized in table 3.1.

Image parametrization The program `star` does another step forward in the analysis. Every image is reduced to a set of parameters describing its shape, orientation and timing parameters. The most relevant parameters are:

- *Hillas* parameters (Hillas, 1985), or the momenta of the 2-D distribution of charge surviving the image cleaning.
  - **Size**: total charge (in phe) contained in the image. It is related to the energy of the primary gamma-ray initiating the shower.
  - **Width**: RMS spread of the light along the minor axis of the shower image. It is related to the lateral development of the EAS.
  - **Length**: RMS spread of the light along the major axis ot the shower image. It is related to the longitudinal development of the EAS.
  - **Conc(N)**: fraction of the charge contained in the N brightest pixels. Images tend to be more compact for gamma-ray induced showers. Typically Conc(2) is used.
- *Timing* parameters.

  - **Time RMS**: spread of the arrival time of Cherenkov photons for the pixels surviving the cleaning.
  - **Time gradient**: linear coefficient of the fitted arrival time projection along the major axis of the ellipse.

- *Quality* parameters.
  - **Leakage***N*: fraction of charge contained in the N outermost pixel rings of the camera. Images with large leakage are likely to be truncated, and this fact must be taken into account in the estimation of the primary gamma-ray energy.
  - **Number of islands**: number of isolated groups of pixels surviving the cleaning in a single event. Gamma-ray showers are expected to produce a single island. Envents with more than one island may have some distortion in the calculation of the Hillas parameters.

Data quality selection The output files of `star` are small (few MB), and contain events from about two minutes of data taking in case of MAGIC I files, and even shorter exposure time for MAGIC II files[8]. As a consequence, `star` files represent a convenient unit for the selection of good quality data.

The data selection has to deal mainly with changing weather conditions and hardware failures. While hardware integrity is constantly checked by the subsystems of the telescopes themselves, the weather conditions are less under control. During the root-format conversion described above, `merpp` includes in the data files reports from a weather station in the telescope site. However, the correlation of the dat quality and the weather parameters is not conclusive. An attempt for a selection procedure of MAGIC I data based on properties of the image parameters was discussed in Reichardt (2009), but the method proposed there was not continued to the stereo data. The most robust, systematic method found so far is the monitorization of the rate of events above a certain *size* cut, after the image cleaning. This *analysis rate*, r, is expected to vary during the observation of a given source due to the change in zenith angle, Z_d:

$$r = r_0 \sqrt{\cos Z_d} \tag{3.6}$$

After the correction of this geometrical effect, `star` files are selected if their rate lies within $\pm 20\%$ of the mean value of the dataset.

Stereo parameter reconstruction Up to this point the analysis chain is applied to the data from each telescope separately. However, in the normal operation mode, only events fulfilling the L3 trigger condition are stored. Therefore, the data from both telescopes are describing the same set of events. The next step is to combine the information from both telescopes and merge it in a single set of events. This is done by a program dubbed `superstar`. The stereoscopic view (figure 3.5) permits the calculation of parameters describing the 3-D development of the particle cascades (Kohnle et al., 1996). The most relevant ones are:

- *Shower axis*, as characterized by:

[8]The shorter exposure time per file is due to the fact that files are recorded with a fixed size at the raw level. The larger amount of pixels in MAGIC II makes the size per event bigger, and consequently the individual files are filled earlier than in MAGIC I.

  - **Shower direction**, is defined by the intersection of the major axes of the two images, once superimposed in the camera plane (figure 3.5b).
  - **Impact point on the ground**, determined by the intersection of the major axes of the two images with respecto to the telescope positions (figure 3.5c).

- **Impact** parameter, or the distance between the camera (of each telescope) and the shower axis, in the direction perpendicular to the telescope axis.

- **Shower maximum heigh**, H_{max}, the altitude at which the maximum of Cherenkov light is yielded during the shower development is obtained using the angle at which the image center of gravity is seen from each telescope. H_{max} depends on the cascade energy. This parameter is used for background rejection, especially at low energies: the H_{max} distribution of gamma rays is Gaussian, but a second peak appears at 2-3 km for low energy ($size < 300$) events (Aleksić et al., 2011). These are single-muon events that can be rejected with a cut in H_{max} (figure 3.6).

- **Cherenkov radius**, r_C is the radius of the Cherenkov light pool on the ground.

- **Cherenkov density**, ρ_C density of Cherenkov photons on the ground.

Gamma/hadron separation The majority of events that trigger the telescopes are extensive air showers initiated by hadrons. The rejection of the majority of this greatly dominant background is possible given that the image parameter distributions differ for gamma-initiated and hadron-initiated showers. The discriminating power of each parameter is encoded in a single global variable called *hadronness*. Gamma-ray events tend to have hadronness close to zero, whereas cascades by charged cosmic rays record events with hadronness tending to one. *Hadronness* is estimated on event basis by means of the Random Forest (RF, Albert et al., 2008), a multi-dimensional classification method based on the construction of decisional trees. Eleven parameters are used to construct *hadronness*: Size, Lenght, Width, Impact, and Time Gradiend from both telescopes plus MaxHeight.

A dedicated RF is to be produced for a given set of observational conditions and hardware configuration. The RF is trained with events from Monte-Carlo simulated gamma rays, and a set of hadron events. The production of Monte-Carlo simulated hadrons is possible, but most often the RF is trained using real data which, in absence of strong gamma-ray souces, is largely dominated by hadrons. The separation power of hadronness is illustrated in figure 3.7.

Improvement of the arrival direction determination The shower direction determined as the crossing of the two semiaxes of the elliptical-shaped shower image on the camera plane entails some dificulties in the case of e.g. very parallel shower images. The arrival direction is better determined by introducing a new parameter, *Disp*, representing the angular distance from the center of gravity of the image to the impact point in the camera (figure 3.8). There are several methods to estimate *Disp* (Lessard et al., 2001, e.g.). The method discussed here consists of introducing all the parameters on which *Disp* may depend in another RF algorithm. The *Disp RF* is trained with a sample of simulated gamma-ray events on known source position, and it grows the corresponding decisional trees to evaluate the correlation between *Disp* and the input parameters. The *Disp* estimation is applied to events of both telescopes separately. This defines two possible arrival

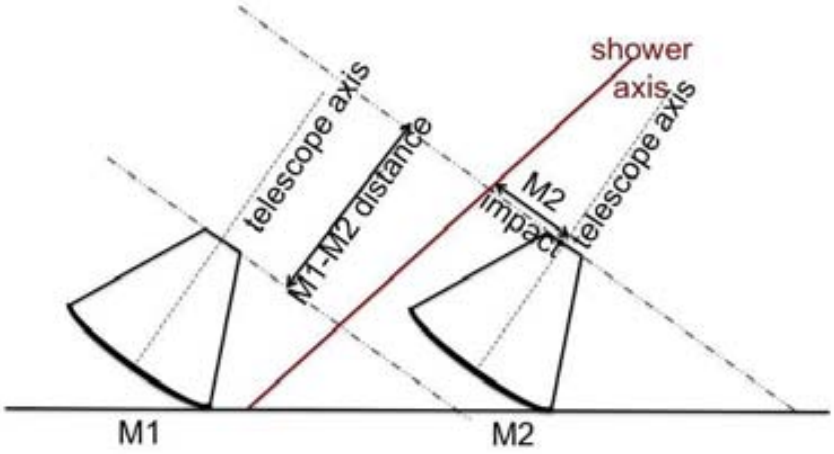

(a) Geometrical definition

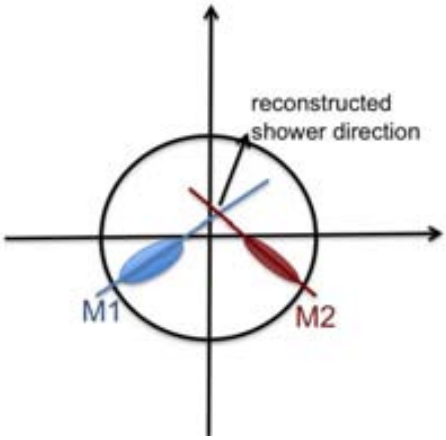

(b) Superimposed cameras

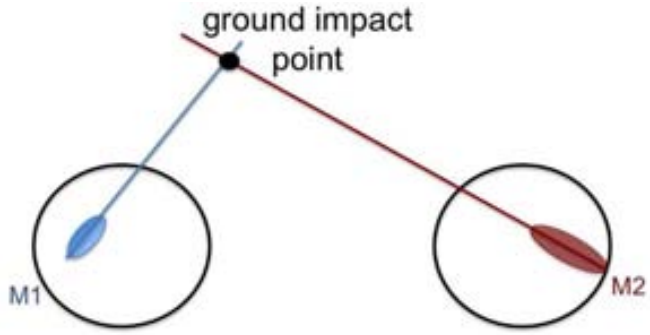

(c) Reconstruction on the ground

Figure 3.5: Sketch of the stereo view of the shower development (a). The intersection of the shower major axes on the camera coordinates (b) defines the incoming direction. The projection on the ground of the shower axes (c) provides the impact point.

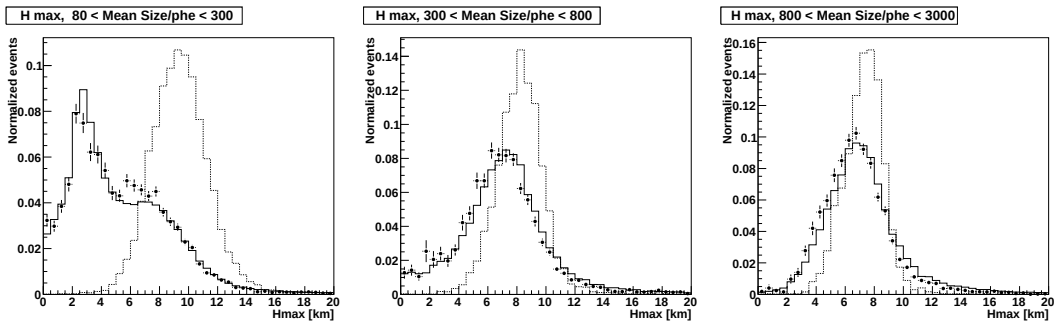

(a) Low energies (b) Medium energies (c) High energies

Figure 3.6: Distributions of the H_{max} parameter in three bins of *size*, corresponding to low, medium and high primary photon energies for Monte-Carlo simulated gamma rays (dotted line), Monte-Carlo simulated protons (solid line), and real data (circles). Extracted from Aleksić et al. (2011).

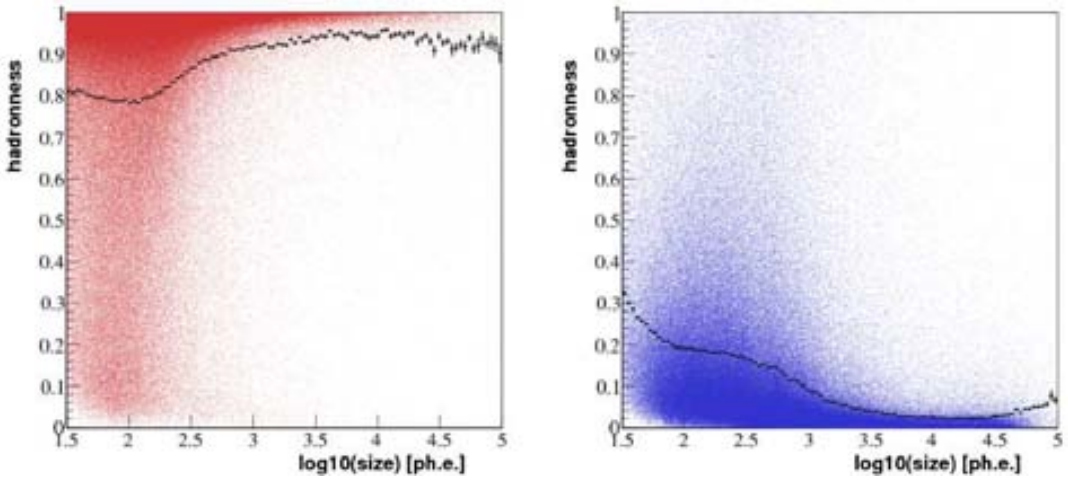

Figure 3.7: *Hadronness* distribution as a function of *size* for a set of real data events (left) and as set of Monte-Carlo simulated gamma-ray events (right), from Zanin (2011).

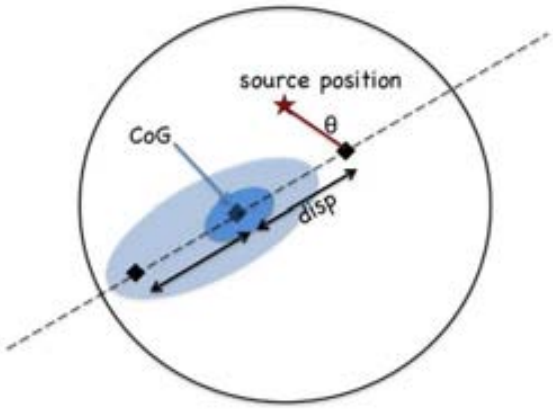

Figure 3.8: Schematical definition of the *Disp* and the θ parameters.

directions along the major axis of the shower image for each telescope. When events are merged, the closest pair is matched, and the reconstructed arrival direction is determined as the weighted average of the chosen pair plus the crossing point of the ellipses.

The estimated arrival direction leads to the definition of a new parameter, θ, as the angular distance between the reconstructed arrival direction and some position of interest. In presence of a source at the position θ, the θ^2 distribution of the events peaks at values close to 0, whereas the background is expected to be isotropic and, therefore, its θ^2 distribution should be flat.

Energy estimation The energy of individual events is estimated using look-up tables (LUTs) generated from gamma-ray Monte-Carlo events of known energy E_{true}. One LUT is built per telescope, based on a simple model describing the distribution of Cherenkov photons on the ground by means of the r_C and ρ_C parameters. For each LUT, the sample of simulated gamma rays with known energy is binned in *size* and $impact/r_C$. The energy of the primary gamma rays is proportional to $size/\rho_C$ (figure 3.9). Therefore, each bin contains the mean value of the distribution of $E_{true} \cdot \rho_C/size$.

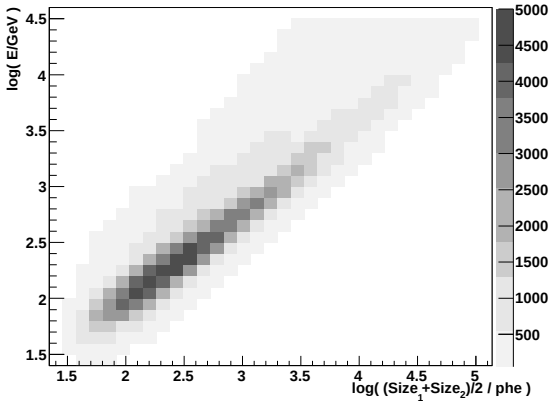

Figure 3.9: Correlation between the average *size* measured by the two telescopes and the true energy from Monte-Carlo simulated gamma-ray events. Extracted from Aleksić et al. (2011).

The application of the RF, the *Disp RF*, and the energy estimation to the `superstar` files is done by the last program in the processing chain, dubbed `melibea`. The outcome of `melibea` are files containing sets events with their stereo and single-telescope parameters, plus a hadronness, *Disp*, and energy estimation. What products to be extracted from these event sets is decided by the analyzer, but there are some tasks are standarized within MARS. The most common of them are discussed below.

Signal evaluation The signal evaluation is often performed by subtracting the θ^2 distributions from two camera directions, one of them containing the possible source (ON region), while the other is signal-free produces a background estimation (OFF region). In the normal observations in wobble mode, the simmetrically opposite direction with respect to the camera center is used to evaluate the background (figure 3.10). The main purpose of the wobble observations is to evaluate the background in the same camera region where the signal is evaluated. Therefore, when a source appears in a position which is not the geometrical center of the multiple wobble pointings[9] this procedure is not strictly correct. In this case the so-called *off from wobble partner* method (figure 3.11) provides a better estimation of the background. The method consists of evaluating the background considering the events of the same region of the camera containg the source, independently on whether they are symmetrical with respect to the wobbling direction. This method was applied for the first time in the analysis described in Chapter 6. The application of the wobble partner method to observations with $n > 2$ wobble pointings allows to calculate the average of the background in $n - 1$ pointings, which translates in a reduction of the statistical uncertainties.

The excess $N_{ex} = N_{ON} - \alpha N_{OFF}$ of gamma-like events is found by subtracting the ON and OFF distributions in a narrow range of θ^2 values close to zero. The normalization factor α accounts for possible differences in the exposure of the ON and the OFF regions, and is evaluated by matching the ON and OFF distributions at large values of θ^2 (figure 3.12). Statistical significance of the excess is evaluated through equation 17 in Li and Ma (1983):

$$\sigma = \sqrt{2}\left[N_{ON}\ln\left(\frac{N_{ON}\,(1+\alpha)}{\alpha\,(N_{ON}-N_{OFF})}\right) + N_{OFF}\ln\left(\frac{(1+\alpha)\,N_{OFF}}{N_{ON}-N_{OFF}}\right)\right]^{1/2} \tag{3.7}$$

[9]This can happen, e.g. in surveys or in case of serendipitous discoveries.

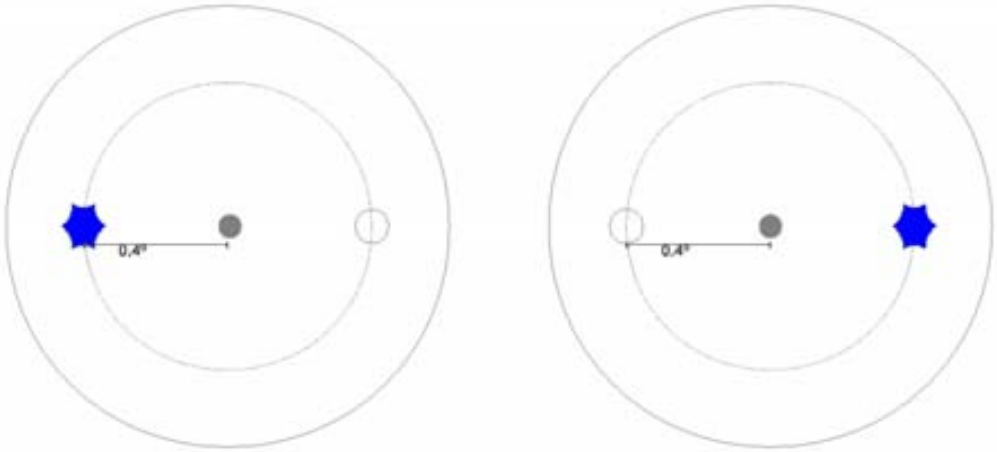

Figure 3.10: Normal off estimation: the telescope is despaced around the center of the observation (gray circle) by, e.g. 0.4° along the right ascension axis. The position ocupied by the source (blue star) in one of the wobble pointings is free of emission (empty circle) in the other wobble pointings. Therefore, a background estimation can be obtained for the same camera position.

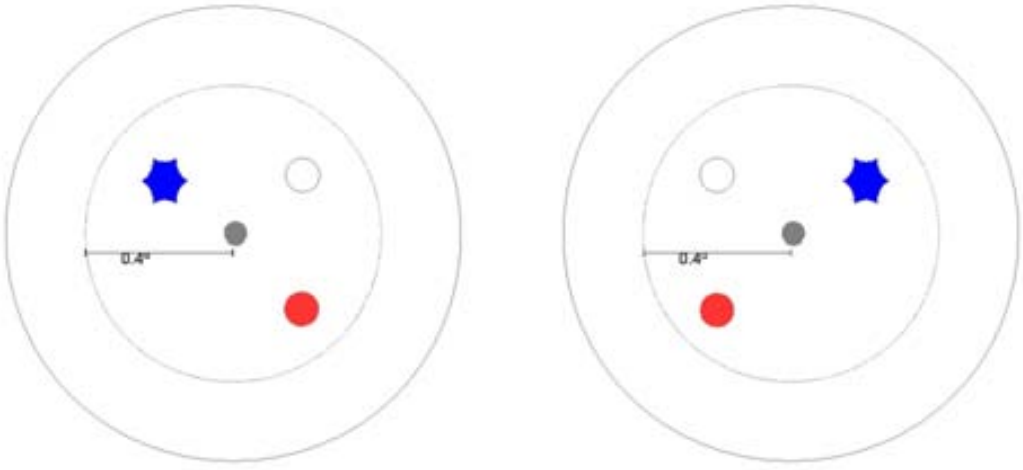

Figure 3.11: Off from wobble partner: when the source (blue star) is not in a position symetrical with respect to wobble displacement, its background estimation is better determined from the same camera position in the complementary wobble pointing (empty circle) than in the symetric position (red circle).

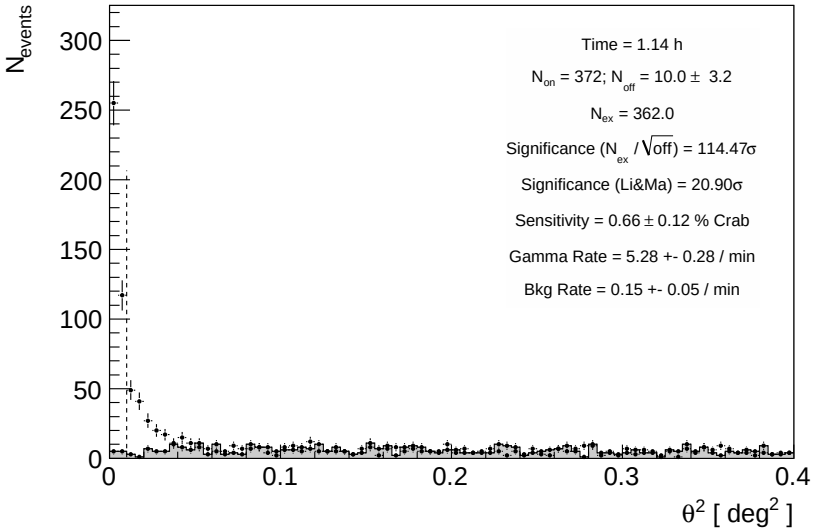

Figure 3.12: θ^2 distributions for ON events (black markers) and OFF events (grey-shaded area) above 250 GeV for an observation of the Crab Nebula from September 7^{th} 2010. The two distributions are normalized for $\theta^2 > 0.15$, while the signal is evaluated for the exces at $\theta^2 < 0.10$.

For the precise evaluation of the detection significance, it is necessary to optimize the analysis cuts so that they provide the maximum sensitivity. The optimization is often carried out based on Crab Nebula observations contemporaneous to the observation of the source of interest. The Crab Nebula is the brightest stable source in the northern sky in the MAGIC energy range, and is observed regularly in order to assess the performance of the telescopes[10]. Hence, the integral sensitivity S of an analysis is expressed in terms of the photon flux (in Crab Units, C.U.) of a point-like source that would lead to a detection with a statistical significance of 5σ after 50 hours of observation. For simplicity, the Gaussian aproximation of the statistical significance is used,

$$S = 5\sqrt{\frac{t_{obs}}{50\,\text{hours}}}\frac{\sqrt{N_{OFF}}}{N_{ex}}\,\text{C.U.} \tag{3.8}$$

The θ^2 distribution of N_{ex} may be fitted with an exponential decay function, $\propto e^{-\theta^2/2D^2}$, where the parameter D may be regarded as the standard deviation of a bidimensional Gaussian distribution in the radial direction, θ. Thus D provides a measure of the extension of the source, to which has been added the instrumental PSF introduced by the telescope and the analysis itself. The intrinsic extension of the source can be computed as $d^2 = D^2 - \text{PSF}^2$. Alternatively, for sources which are known to be point-like like the Crab Nebula itself[11] or distant active galactic nuclei, this procedure provides a measurement of the PSF.

Sky mapping Sky maps are bidimensional histograms in sky coordinates containing the arrival directions of all gamma-ray candidate events (that have survived the event-selection cuts, in particular in hadronness). A background exposure model is constructed

[10] A complete characterization of the Crab Nebula can be found at Zanin (2011).

[11] Imaging Atmospheric Cherenkov telescopes like MAGIC are approaching an angular resolution that may allow to resolve the Crab Nebula in a near future. However, no evidence of extension has been reported so far.

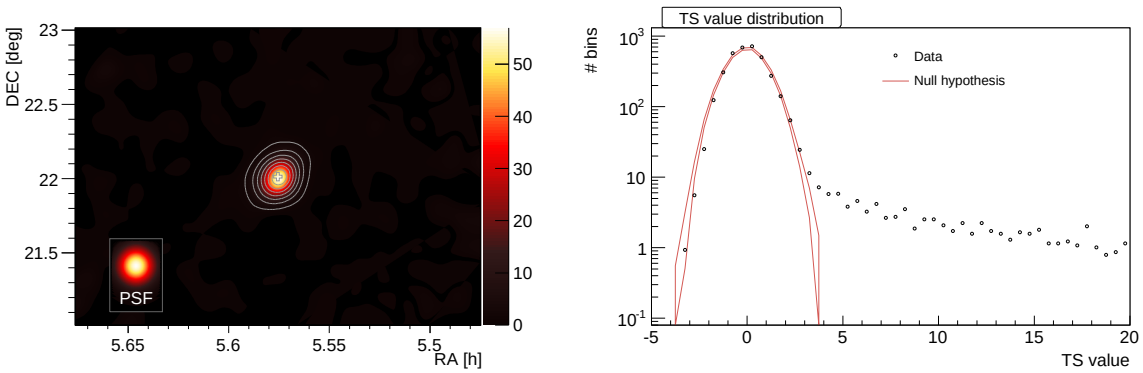

(a) Sky map

(b) Significance distribution

Figure 3.13: Example of application of the sky mapping procedure to the same sample of Crab Nebula data as in figure 3.12. (a) The color scale represents relative flux N_{ex}/N_{bg}, whereas contours are test statistic isocurves in steps of 7, starting at 5. A marker is placet at the location of the source resulting from the fit of a two-dimensional Gaussian. (b) Significance distribution of the sky bins (black circles) with the distribution expected in absence of a source (pink curve).

from the photon-like events in the sky areas opposite to the source position in each wobble data set. Before the subtraction of the background expectation map from the measured events, a Gaussian kernel density smoothing is applied. The width of this kernel is an analysis parameter to be adjusted depending on the measured PSF. The test statistic derived this way resembles that of equation 3.8, except that the null hypothesis distribution may differ slightly from a Gaussian distribution (Lombardi, 2011). The intensity of the signal is visualized by means of the relative event flux, N_{ex}/N_{bg}, where background envents N_{bg} are averaged in a radius of 0.1° (figure 3.13).

Spectrum calculation The differential energy spectrum of the gamma-ray emission is defined as the number of gamma rays N_γ per unit area A_{eff} and effective time t_{eff} and per unit of energy bandwidth.

The effective observation time differs from the wall clock time due to the dead time of the detector, which comes mainly from the readout subsystem. The arrival time of events follows a Poissonian distribution, $\mathrm{d}N/\mathrm{d}t \propto e^{-\lambda t}$, where λ is the phyiscal event rate. λ can be estimated from the distribution of time differences between one event and the next one. Hence, the effective time is $t_{eff} = N_\gamma/\lambda$.

The effective collection area A_{eff} is the geometrical area around the telescopes A_{sim}, where a gamma-ray shower may produce a trigger, downscaled by the efficiency[12] ϵ of the cuts applied to the data set in order to reduce the background. The effective area is energy-dependent, and varies during the observation of a source due to the change in zenith angle. A_{sim} is calculated with a set of Monte-Carlo simulated gamma-ray events, whose energy E_{true} is known. The effective area of the MAGIC telescopes grows rapidly at low energies and saturates somewhat below 1 TeV at a value of about $10^5\,\mathrm{m}^2$ (figure 3.14).

N_γ is evaluated, in each energy bin, as the number of excess events in a region of radius θ, after subtracting the background by one of the methods discussed above. Since statistics may be scarce, especially at high energies, looser cuts in hadronness are applied than in the signal evaluation, so that efficiencies of about 90% are achieved.

[12]Cut efficiency stands for the fraction of surviving events after applying a cut.

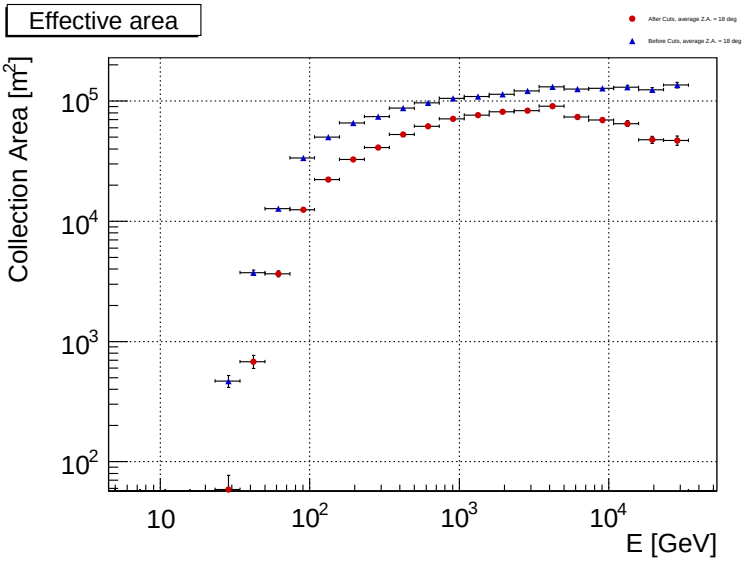

Figure 3.14: Example estimation of the effective area of an observation at low zenith angle. The estimation is done with diffuse Monte-Carlo simulated gamma-ray events

The spectrum obtained by this procedure is affected by distortions in the number of events of each bin due to the finite energy resolution of the detector. In particular, an energy estimation E_{est} has been computed as a function of image parameters, but this energy differs from E_{true}, which is unknown. Let $M(E_{true}, E_{est})$ be the response of the detector, then the measured distribution $g(E_{est})$ is a transform of the true energy distribution, $f(E_{true})$:

$$g(E_{est}) = \int M(E_{true}, E_{est}) f(E_{true})\, \mathrm{d}E_{true} \tag{3.9}$$

To unfold the distribution $f(E_{true})$ it is convenient to treat the problem in energy bins, so that

$$E^i_{est} = M^i_j E^j_{true} \tag{3.10}$$

The matrix M is known as *migration matrix* (figure 3.15), and is elaborated by applying to simulated gamma rays the same energy estimation as for real data.

The unfolding may be applied by assuming some functional shape for $f(E_{true})$ (usually a power law), and minimizing the χ^2_0 values to fit observed distribution $g(E_{est})$. This so-called *forward* unfolding is robust. However, forward unfolding does not provide corrected spectral points but only the parameters of the assumed (biassed) spectral shape. A more accurate method is to invert the migration matrix. However, the inversion requires the introduction of a *regularization* term in order to smear the unfolded distribution and take into account the finite energy resolution of the instrument. The different regularization methods commonly used in the MAGIC analysis are those from Tikhonov and Arsenin (1977), Schmelling (1994) and Bertero (1989).

Upper limit calculation When an excess of gamma-like events does not provide a significant detection[13], upper limitis to the integral or the differential flux of source may

[13]The usual threshold for considering a source significantly detected is $5\,\sigma$ in the sense of Li and Ma (1983). When computing the spectrum of sources significantly detected, individual spectral points are

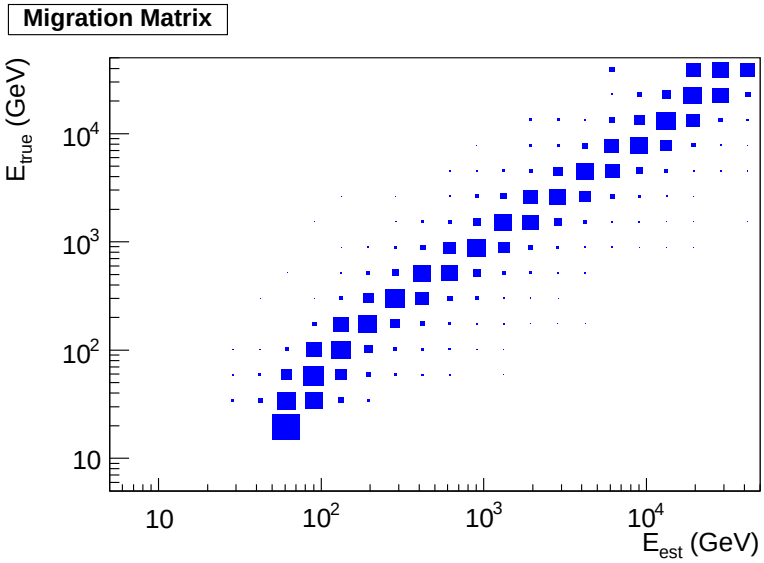

Figure 3.15: Migration matrix for the same example observation from figure 3.14.

be computed. Given a number of observed excess events N (which may be positive or negative), the maximum number of excess events N^{UL} is obtained by the method from (Rolke et al., 2005). The conversion to flux upper limit is done through the assumption of a spectral shape for the source of interest, $\Phi(E) = K \cdot \S(E)$. After calculating the effective time and effective are as discussed above, the normalization constant K for photon energies in a certain range above the analysis threshold is obtained from:

$$K \leq \frac{N^{UL}}{t_{eff} \int_{E_1}^{E_2} S(E) A_{eff}(E) \mathrm{d}E} \tag{3.11}$$

3.2.3 Automated, large-scale data processing

The data from the MAGIC telescopes are processed in the Counting House, and preliminary analysis products such as detection plots are already elaborated during the observations. The files produced by this on-site analyisis (OSA) are sent through a dedicated link to the Port d'Informació Científica (PIC), near Barcelona, where the MAGIC Data Center is located. The analysis products from the OSA are, in principle, final up to the `star` level. Instead, data selection and the subsequent analysis steps are recommended to be performed under close supervision by the analyzers, and the OSA generated files are only used in analyses requiring a fast reaction.

The calibration performed by `callisto` and data reduction and parametrization performed by `star` are the most CPU-consuming processes in the analysis chain and can be run routinarily, with little intervention of the analyzer. Occasionally, improvements or corrections of problems in MARS motivate the reporcessing of large ammounts of data, with typical volumes of 100 TB. The OSA is not foreseen to cope with these large-scale reprocessings, which are carried out using a large CPU cluster at PIC. For this purpose we developed a set of scripts that steer and execute automatically `callisto` and `star`, according to the needs of the collaboration. An early stage of this development dealt

required to have a significance of at least $1.5\,\sigma$.

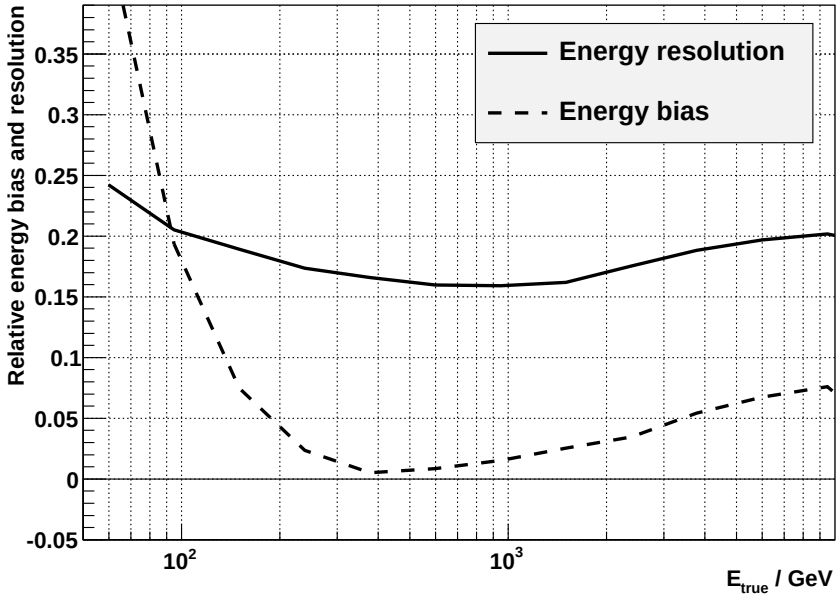

Figure 3.16: Relative energy resolution (solid line) and difference between E_{est} and E_{true} (bias, dashed line) from Monte-Carlo simulated gamma rays. Extracted from Aleksić et al. (2011).

with 115 TB of raw data from the (at that time) standalone MAGIC I telescope in 2008 (Reichardt, 2009). Moreover, we estimated the data volume that should be handled due to the advent of the MAGIC II telescope in late 2009 (Reichardt et al., 2009). A more advanced infrastructure was later established, when PIC decided to adapt its operating system to meet the Grid standards (Firpo et al., 2011). In addition to eventual reprocessings, our duties at the MAGIC Data Center included a support service for the whole collaboration, where queries about the data access were attended.

3.2.4 Performance of the MAGIC telescopes

The performance of the stereo observations MAGIC telescopes, with the analysis techniques described above, is evaluated in different aspects (Aleksić et al., 2011):

Energy resolution is better than 25%, achieving a 16% for energies around 1 TeV (figure 3.16).

Angular resolution is 0.07°, in the highest energy range (figure 3.17).

Sensitivity Integral sensitivity is defined as the minimum flux from a point-like source detectable with a significance of $5\,\sigma$ after 50 hours of observation. The sensitivity above the threshold of the instrument is $(1.99 \pm 0.03)\%$ the Crab Nebula flux, and improves for higher energies. The best value is obtained for energies above 290 GeV, where fluxes of $(0.76 \pm 0.03)\%$ that of the Crab Nebula can be detected (figure 3.18). If computed in narrow energy bins, the *differential* sensitivity provides a way to estimate the detectability of objects with arbitrary spectral shape. The differential sensitivity ranges from 10% the Crab Nebula flux at energies close to the threshold, to 1.5% the Crab Nebula flux at energies of several hundred GeV (figure 3.1).

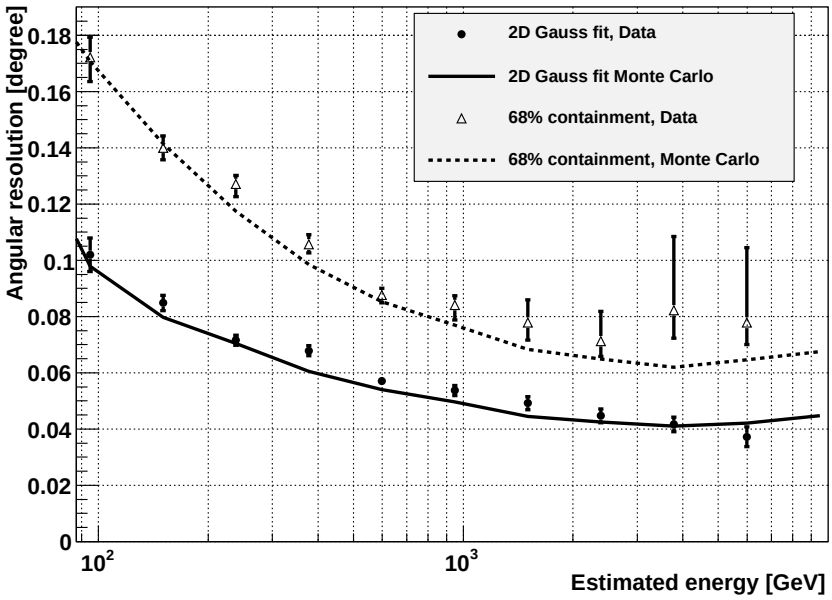

Figure 3.17: Angular resolution as a function of the estimated energy obtained from a sample of Crab Nebula data (markers) and Monte-Carlo simulations (lines). Extracted from Aleksić et al. (2011).

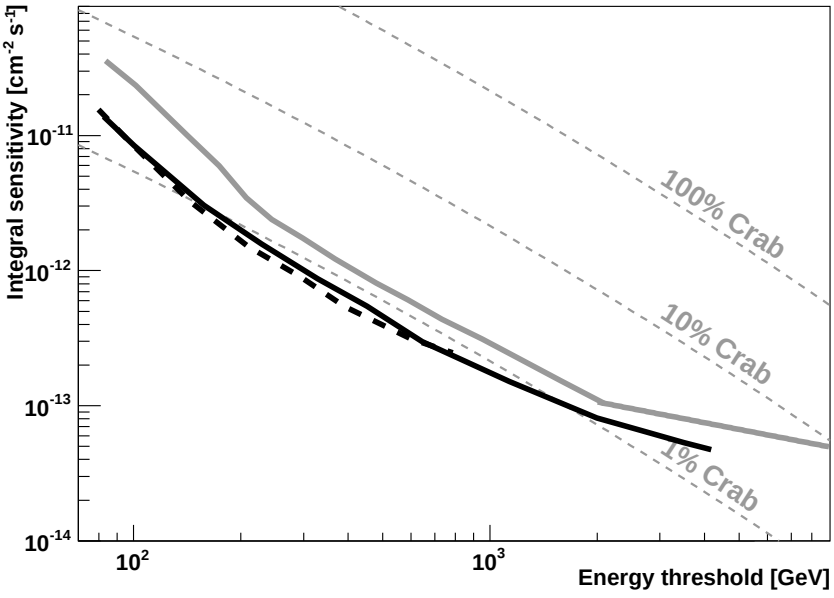

Figure 3.18: Integral sensitivity of stereo observations (black lines) as a function of the energy threshold. The dashed line is a prediction from Monte-Carlo simulations, whereas the solid line is measured from observations of the Crab Nebula. The gray line represents the sensitivity achieved with the MAGIC I telescope in standalone operation. For refference, different fractions of the flux of the Crab Nebula are represented as thin dashed lines. Extracted from Aleksić et al. (2011).

Systematic uncertainties A thorough study of all sources of systematic error that contribute in the measurements with the MAGIC telescope is found in Aleksić et al. (2011). In summary, the energy scale is determined with a precision of 17% at low energies, and 15% at medium energies. A systematic error of 0.15 is estimated to affect the spectral index. At medium energies, the uncertainty in the flux normalization is estimated as 11%. At low energies, the systematic errors are in general larger, and the flux normalization is known with a precision of about 19%. The Crab Nebula spectrum is consisten with other experiments within 20-30%.

Chapter 4

Extended gamma-ray emission from the supernova remnant HB 21

HB 21 is a nearby supernova remnant surrounded by dense clumps of molecular gas. We analyzed 3.5 years of public Fermi/LAT data around the position of the supernova remnant HB 21, where four point-like sources from the 2^{nd} Fermi/LAT catalog are located. We determined that the gamma-ray source is produced by a single extended source, and modeled the observed morphology as a uniform circle. The spectral energy distribution is best described by a curved power law, with a maximum at 413 ± 11 MeV. We divided the circle into three regions defined by previously identified shocked molecular clouds, and found that one of these regions has a softer spectrum. The > 3 GeV gamma-ray emission of the soft spectrum region is bow-shaped and coincident with the supernova remnant shell seen at radio wavelengths. These findings, published in Reichardt et al. (2012) suggest that the gamma-ray emission from HB 21 is a combination of emission from shocked/illuminated molecular clouds, on of them coincident with the supernova remnant shell itself.

4.1 Introduction

HB 21 (G89.0+4.7) is a 19000 year old[1] (Leahy and Aschenbach, 1996) mixed-morphology supernova remnant at a distance of 0.8 kpc (Tatematsu et al., 1990). As seen in radio continuum images, the supernova remnant displays an elliptical shell of $2^\circ \times 1.5^\circ$ (Condon et al., 1994) (mean diameter of ~ 25 pc), slightly tilted in the NW-SE direction. Only weak, center-filling X-ray emission of thermal origin is associated with HB 21 (Lazendic and Slane, 2006).

The interaction of HB 21 with the surrounding interstellar medium (ISM) has been intensively studied. Given the absence of OH masers around HB 21 (Frail et al., 1996), the evidence of interaction between the blast wave and the ISM is established by means of local dynamic effects that broaden emission lines (figure 4.1). Evidence of shocked molecular gas was found by Koo et al. (2001) in the northern and in the southern parts of the shell. The northern cloud (cloud N hereafter) consists of several small, bright clumps plus a diffuse component extending to the E. The southern cloud (cloud S) presents

[1] We quote here the commonly accepted age for this object, but we note that there are indications that HB 21 could have an age of the order of 5000 years (Lazendic and Slane, 2006)

a complex filamentary structure, with a velocity spread of up to 40 km s^{-1} for some particular clumps, and it is coincident with a mass of shocked atomic gas detected by Koo and Heiles (1991). Cloud S and N show evidence of molecule reformation after a J-type shock passage (Shinn et al., 2012). There is also a shocked cloud at the NW rim of the radio shell (cloud NW) (Byun et al., 2006). The central thermal X-ray bright area is occupied by small evaporating clouds. There is also a gas componend (cloud E in figure 4.1), but its velocity range shows that it is not physically associated to HB 21 (Byun et al., 2006).

The so-called clouds A, B, and C (Tatematsu et al., 1990) are aligned N-S in the approximately straight E rim of the supernova remnant. These clouds may be regarded as overdensities of the giant molecular cloud of the Cyg OB7 association (Huang and Thaddeus, 1986), which provides the distance estimate for HB 21. Clouds A, B, and C are located where the eastward blast wave apparently collides with the so-called *wall*. The wall consists of a sharp edge of otherwise smoothly distributed atomic gas, which extends beyond the supernova remnant boundary, both N and S. Therefore, the wall seems to be a pre-existing structure that affects the evolution of the supernova remnant and not the other way around. Probably, the wall is the border of the cavity resulting from a former HII region around the HB 21 progenitor, which might be a former member of the Cyg OB7 association (Tatematsu et al., 1990). Clouds A, B, and C most likely already existed at the time of the supernova remnant explosion, shown no broad emission lines (they are not shocked), and their velocity is not significantly different from that of the wall (Tatematsu et al., 1990). Therefore, there is also the possibility that the coincidence of the A, B, C clouds and the wall with the supernova remnant eastern edge is a projection effect, and both structures are not physically related. Byun et al. (2006) suggested that the HB 21 could be as far as 1.7 kpc, in which case the whole Cyg OB7 complex would be in the foreground. However, the lack of broad line emission is also the case for clouds related to the supernova remnant 3c391, where the interaction is certain (Reach et al., 2002). Moreover, cloud A coincides with a concavity of the supernova remnant shell. The coincidence of cloud A with this feature in the radio continuum emission suggests that the overtaking of this cloud leads to retardation of the shock front in comparison to the surrounding, although high-resolution CO maps from Koo et al. (2001) did not find such evidence. There is still the possibility that the shock is dissociative, and molecules have not been reformed (thus being omitted in the search of broad line emission regions). In fact, Koo et al. (2001) mentions a diffuse component connecting clouds N and A. But the shock velocity of 20 km s^{-1} observed by Koo is in principle not enough for molecule dissociation (which typically requires 25–50 km s^{-1}).

According to Nolan et al. (2012) three point-like sources (2FGL J2041.5+5003, 2FGL J2043.3+5105 and 2FGL J2046.0+4954) in the second *Fermi*/LAT source catalog (2FGL catalog hereafter) are coincident with the extended radio emission of HB 21. Two point-like sources (1FGL 2042.3+5041 and 1FGL J2046.0+4954) were already detected in the first *Fermi*/LAT source catalog (Nolan et al., 2012). Therefore, the gamma-ray emission related to HB 21 is rather bright.

4.2 Data analysis

We analyzed *Fermi*/LAT data corresponding to the period between August 4^{th} 2008 (start of science operations) and February 2, 2012. HB 21is located at $(\alpha, \delta) = (20^h45^m, 50°35')$ (Ferrand and Safi-Harb, 2012), almost 5° off the galactic plane. This fact allows

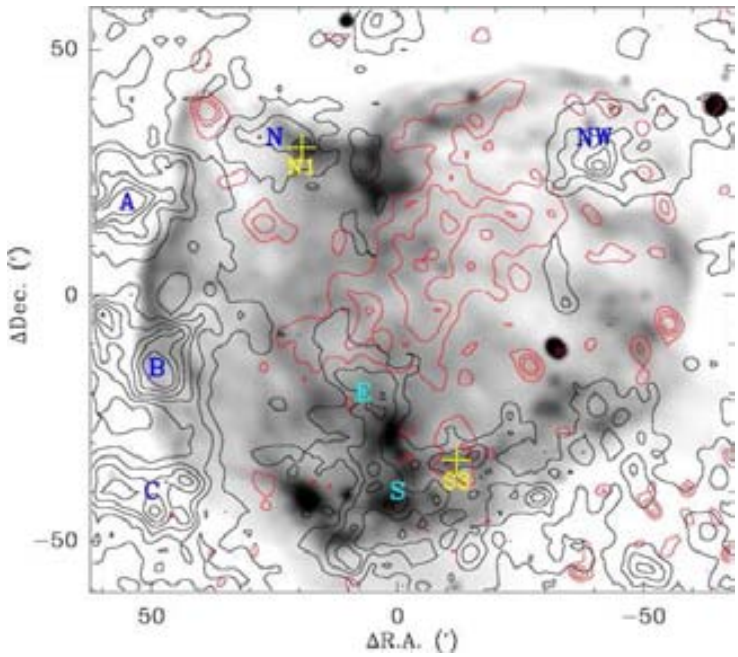

Figure 4.1: ^{12}CO $J = 1 - 0$ map integrated in the rage -20 to $+5\,\mathrm{km\,s^{-1}}$(black contours) overlaid on the 1420 MHz continuum image of HB 21 (gray scale). Red contours depict the X-ray emisson detected by ROSAT. The position of the clouds A, B, C, N, NW, S, and E (discussed in the text) is marked in blue letters. Yellow crosses mark the position of shocked clumps. Reproduced from Byun et al. (2006).

for a notably background-reduced analysis with respect to the sources found at lower galactic latitudes if the center of the ROI is displaced away from the Galactic plane, so that less Galactic background emission enters the ROI. For this purpose, we defined the ROI as a circle of 10° radius centered on the position $(\alpha, \delta) = (20^h41^m05^s, 51°15'58'')$, which is displaced by 1° toward positive galactic latitudes with respect to the catalog position of HB 21. To this data set, we applied the analysis pipeline discussed in section 3.1.1.

The null hypothesis for the likelihood analysis consisted of the standard galactic and extragalactic diffuse emission models provided in the *ScienceTools*, plus the point-like sources in the 2FGL catalog lying up to 15° away of the ROI center. From these, we excluded 2FGL J2041.5+5003, 2FGL J2043.3+5105, 2FGL J2046.0+4954 and 2FGL J2051.8+5054, as we cosidered that they were associated to HB 21. We note that according to Nolan et al. (2012), the source 2FGL J2051.8+5054 is not associated to HB 21, but it lies very close to the NE edge of the supernova remnant shell, in remarkable coincidence with the above-mentioned cloud A (see figure 4.2a). For this reason, we considered 2FGL J2051.8+5054 as part of the gamma-ray emission related to HB 21. We compared the maximum likelihood obtained with the null hypothesis to those of several models that included various morphological descriptions of the GeV emission from HB 21. First, we included the four point-like sources mentioned above. Next, we explored the possibility that the observed emission is from an extended, resolved source. For this, the four point-like sources associated to HB 21 were replaced by extended source templates. For each model, TS was evaluated as

$$\mathrm{TS} = -2\log(\mathcal{L}_0/\mathcal{L}), \tag{4.1}$$

where $\mathcal{L}_0$ and $\mathcal{L}$ are the likelihood of the null hypothesis and the tested models respectively.

Table 4.1: TS of the spatial models above different minimum energies. N is the number of additional parameters of the model with respect to the null hypothesis accounting for the spectral index and normalization factor of each additional source or component.

Model	N	TS_{100}	TS_{500}	TS_{1000}	TS_{3000}
1. 2FGL sources	10	959	610	245	48
2. Circle	2	832	626	279	53
3. 4850 MHz	2	780	613	275	42

After the selection of the spatial template yielding greater TS, we proceeded with the spectral analysis, in which the different spectral shapes were assumed for the source model for HB 21. The convenience of each spectral shape was evaluated with the likelihood ratio $-2\log(\mathcal{L}_{pl}/\mathcal{L}_{model})$, where $\mathcal{L}_{pl}$ is the maximum likelihood obtained by modeling the spectrum as a power law, and $\mathcal{L}_{model}$ is the maximum likelihood of the tested model, which contains additional spectral parameters.

4.3 Results

4.3.1 Morphology

To visualize a possible gamma-ray source associated to HB 21, we produced the S/N maps of the null hypothesis in different energy ranges (figure 4.2). At the lowest energies (figure 4.2a) it is not possible to distinguish any structure beyond a more or less flat emission extended throughout the supernova remnant shell. Above 500 MeV (figure 4.2b) and above 1 GeV (Fig. 4.2c) a shell-like structure may be intuited. Above 3 GeV (figure 4.2d) several structures become visible. The most remarkable feature is the NW arc, which coincides with the supernova remnant shell and the position of cloud NW. There is also a bright spot close to cloud A, which seems to become more prominent with increasing energy. The center of the supernova remnant does not show especially bright emission, whereas the S part of the shell presents an enhancement roughly coinciding with cloud S. We show below that the emission above 3 GeV is still significant (table 4.1).

To evaluate the morphological properties of the source, several scenarios were considered:

1. The four point-like sources from 2FGL coincident with HB 21;

2. The 4850MHz map from (Condon et al., 1994), where the quasar 3c418.0 was removed from the radio map (see discussion below);

3. A circle of flat emission centered on the catalog position of HB 21.

All the templates were rebinned to match the field of view and the pixel size of the *Fermi*/LAT maps. In table 4.1 we show the TS values for each model in several energy regimes, as well as the number of additional parameters in each model. The point-like sources model introduces additional degrees of freedom for the flux normalization of each of the four sources, plus the spectral indices. 2FGL J2043.3+5105 and 2FGL J2046.0+4954 contain an additional parameter β which allows an energy-dependent spectral index $-\alpha - \beta\log(E/1000\mathrm{GeV})$. The spectrum of the circle and the 4850 MHz templates are described by a power-law function at this stage.

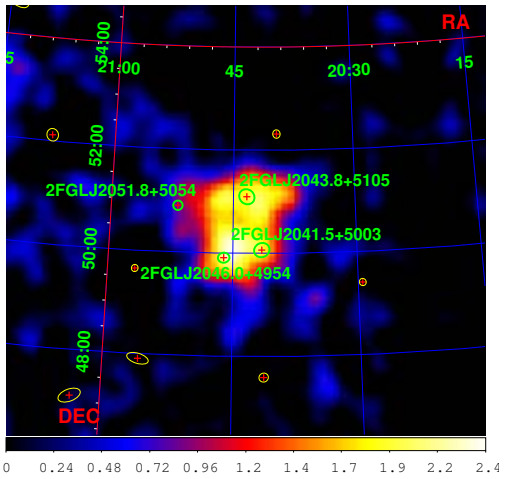

(a) S/N map above 100 MeV. Red crosses are the point-like sources from 2FGL catalog surrounded by their 95% position uncertainty ellipses. Sources highlighted with green ellipse are those ones we consider related to HB 21 and are removed from the model when computing the null hypothesis map.

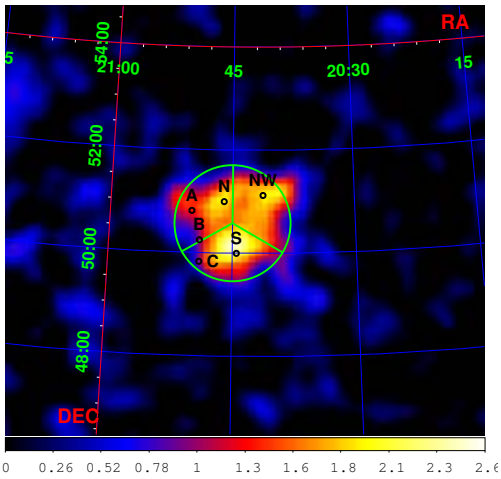

(b) S/N map above 500 MeV. The circle used for the spectral modeling is shown, as well as the divisions discussed in table 4.2. Symbols A, B, C, NW, N, and S mark the position of the relevant clouds, mentioned in section 4.1. The size of the markers is not related to the extension of the clouds.

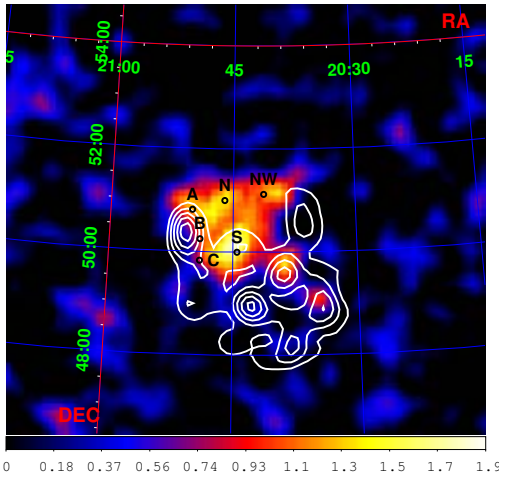

(c) S/N map above 1 GeV. White contours represent the large-scale CO distribution from Dame et al. (2001) integrated between 0 and -20 km s^{-1}. Symbols A, B, C, NW, N, and S mark the position of the relevant clouds, mentioned in section 4.1.

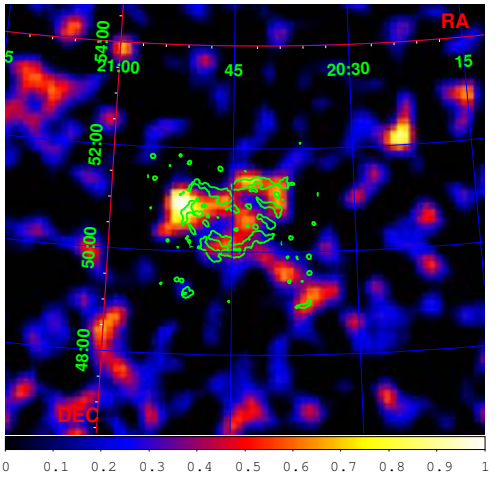

(d) S/N map above 3 GeV. Green contours depict the 4850 MHz radio continuum emission (Condon et al., 1994).

Figure 4.2: S/N maps above 100 MeV, 500 MeV, 1 GeV, and 3 GeV. The color scale represents signal-to-noise ratio (defined as real counts minus model counts divided by square root of model counts) for the null hypothesis. Different multiwavelength information is included in each panel.

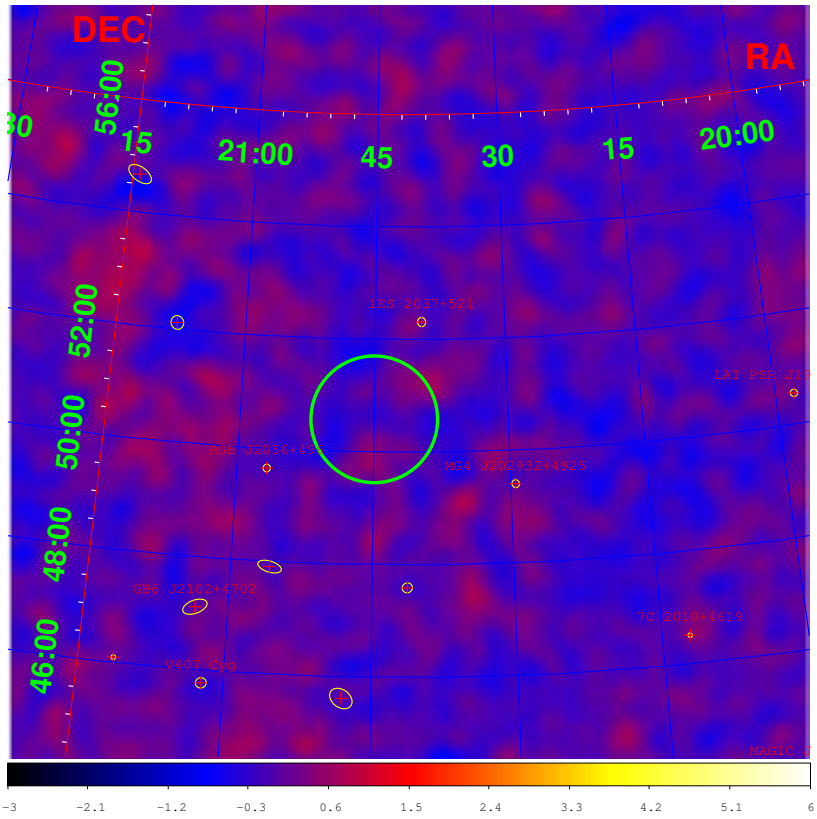

Figure 4.3: S/N map of the ROI defined around HB 21 after including the model (2) for energies between 100 MeV and 100 GeV. The circle modeling HB 21 is shown in green, whereas the rest of the sources in the model are marked as red crosses with their counterpart name, if it is known. Yellow ellipses represent the uncertainty in the position of the point-like sources. All the S/N values for the pixels in the ROI are cointained in the range of ±1.

All the models listed above provide a good description of the HB21 field compared to that of the null hypothesis. The S/N maps are flat after including any of these modelizations (e.g. figure 4.3). Thus, one or more sources are detected in the HB 21 region with high significance, even at energies above 3 GeV. However, we discarded the description by means of point-like sources, since it provides the highest TS only at the lowest energies (table 4.1), where the broad PSF of *Fermi*/LAT does not allow disentangling any substructure. The model with the point-like sources introduces ten degrees of freedom. Therefore we considered that the improvement in TS at low energies came from the greater number of parameters, and not from the point-like source model being a better description of the morphology. With only two degrees of freedom, the overall emission was well described at all energies by a circle of radius 1.125° centered on the catalog position of the supernova remnant. The radius of the circle was chosen to provide the highest TS after varying it from 0.75 to 1.375° in steps of 0.125° (one pixel). Initially, we assumed a simple power-law function as spectral model.

To further investigate the possibility of a limb-brightened morphology we produced the radial profiles of the excess (real counts minus model counts, for the null hypothesis) in each energy range, and we compared this profile with the one expected from models (2)

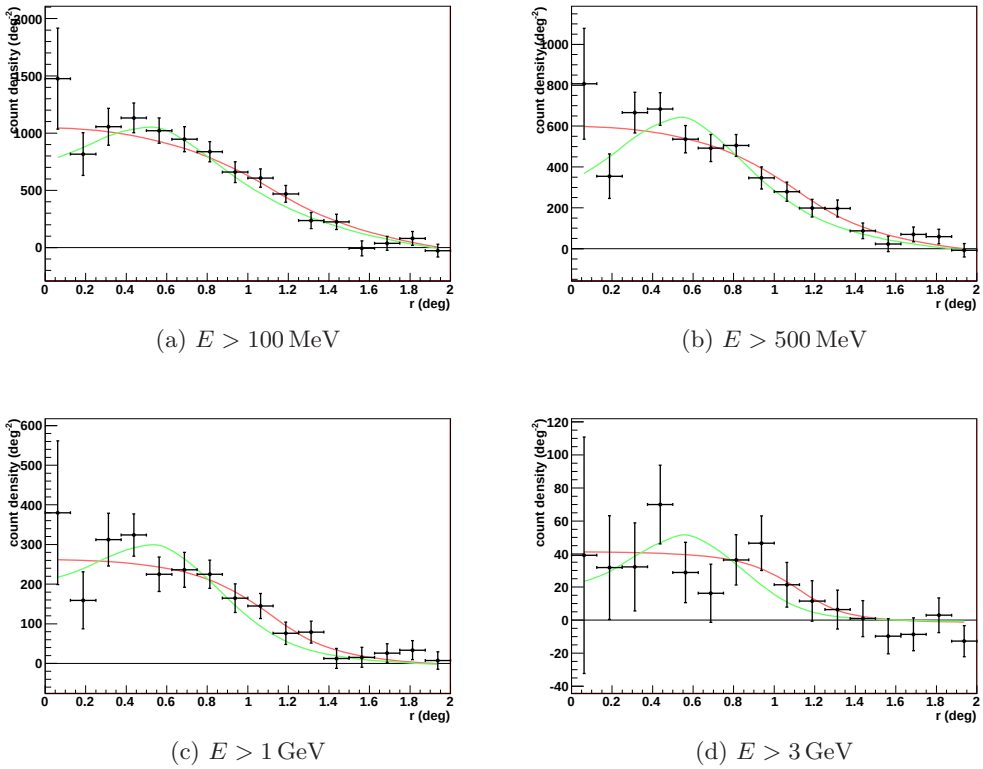

(a) $E > 100\,\mathrm{MeV}$ (b) $E > 500\,\mathrm{MeV}$

(c) $E > 1\,\mathrm{GeV}$ (d) $E > 3\,\mathrm{GeV}$

Figure 4.4: Radial profile of the excess (real counts minus model counts generated with the null hypothesis model). Red curve represents the profile expected from a flat circular emission region of 1.125° radius. Green curve represents the profile expected from a gamma-ray emission following the radio continuum emission at 4850 MHz.

and (3) (figure 4.4). In view of the profiles, we concluded that the combination of broad PSF at low energies and scarce statistics at high energies does not permit to distinguish both morphologies in angular scales of less than two degrees. However, given the hints obtained so far, we considered this possibility by testing several ring-shaped models with various inner and outer radii. The outer radius is varied within the same range as for the optimization of the flat circle, whereas we considered inner radii ranging from 0 (circle) to 0.75°, also in steps of 0.125. The best combination at all energies is 0.125° for the inner radius and 1.125° for the outer radius. However, the difference in TS with respect to the flat circle is about 0.1 at all energies. In addition, we consider that smearing by the PSF would prevent such a narrow hole (of only two pixels) from being distinguished if used, so we continued to use the flat circle for the subsequent analysis.

We addressed the possibility of having additional point-like sources besides the above-mentioned ones. First, the NW corner of the radio shell reveals a bright point-like radio source due to the presence of the quasar 3c418.0 at $z = 1.6865$ (Paturel et al., 2002). We considered the possibility that this quasar contributes to the gamma-ray emission. To do so, we looked for variability in the GeV signal by means of an aperture analysis within a radius of one degree around 3c418.0. After several temporal binnings we did not find any significant variability in the photon rate around the quasar. Therefore, we concluded that if this object has any contribution, we would not disentangle it from that of the supernova remnant with the current data set. Secondly, in the 1 GeV map (figure 4.2c) two spots

appear SW of the supernova remnant. Comparing with the CO large-scale distribution around the supernova remnant we found that these spots are roughly coincident with local maxima of the gas distribution. Taking this possibility into account, we repeated the likelihood analysis adding two sources at the position of the gas overdensities. None of these sources were significant, whether in the analysis above 100 MeV energies or above 1 GeV, so they were not included in the final model.

4.3.2 Spectral energy distribution

We divided the considered energy range (100 MeV to 100 GeV) into twelve bins and computed the spectral energy distribution of the whole source by extracting its flux in each bin (figure 4.5). Only those bins with TS$>$ 10 ($\sim 3.2\sigma$) are shown as spectral points. The last significant bin is the one from 3.2 GeV to 5.6 GeV. In addition we show 95% confidence level upper limits for the explored energy range, up to 100 GeV. The upper limits correspond to the flux providing a likelihood value such that $2\Delta \log \mathcal{L} = 4$.

We noticed that the spectrum deviates from a power-law function and suggests the presence of a peak at few hundred MeV. We tested the possibility that the gamma ray emission is described by a smoothly broken power law of the form

$$\frac{dN}{dE} = N_0 \left(\frac{E}{100\mathrm{MeV}}\right)^{\gamma_1} \left(1 + \left(\frac{E}{E_b}\right)^{\frac{\gamma_1-\gamma_2}{0.5}}\right)^{-0.5}, \tag{4.2}$$

or a curved power law (log-parabola)

$$\frac{dN}{dE} = N_0 \left(\frac{E}{1000\mathrm{MeV}}\right)^{-\alpha-\beta\log\frac{E}{1000\mathrm{MeV}}}, \tag{4.3}$$

or a power law with a cut-off

$$\frac{dN}{dE} = N_0 \left(\frac{E}{1000\mathrm{MeV}}\right)^{-\gamma} \exp\frac{E}{E_{cutoff}}. \tag{4.4}$$

The likelihood ratios for equations 4.2 (two extra degrees of freedom), 4.3, and 4.4 (one extra degree of freedom) are 143, 146, and 130, respectively. Provided that the log-parabola introduces an additional parameter (β) to the simple power law, we concluded that the chance probability of the log-parabola being a better description of the spectrum is 1.5×10^{-33}. The TS of the flat circle (with log-parabolic spectral shape) with respect to the null hypothesis is 988, which roughly corresponds to a detection significance at the level of 31 standard deviations. The best fit parameters are $\mathrm{N_0} = (17.5 \pm 0.2)10^{-12}\,\mathrm{cm^{-2}s^{-1}MeV^{-1}}$, $\alpha = 2.596 \pm 0.013$, $\beta = 0.338 \pm 0.008$, where uncertainties are only statistical. The total energy flux is $(1.10 \pm 0.03) \times 10^{-4}\,\mathrm{MeV\,cm^{-2}s^{-1}}$, with a maximum in the spectral energy distribution at 413 ± 11 MeV.

To explore possible spectral differences throughout HB 21, we divided the circle in three pieces covering 120° each and let them acquire different values for the N_0, α and β. In this way, segment NE covers clouds A and N; segment NW covers cloud NW and segment S covers cloud S. We used the likelihood ratio $-2\log(\mathcal{L}_{segment}/\mathcal{L}_{circle})$, where $\mathcal{L}_{segment}$ refers to the segmented circle without the tested segment. With this likelihood ratio, two thirds of the circle may be regarded as part of the null hypothesis, thus providing a measure of the significance of the tested segment. All three segments contribute

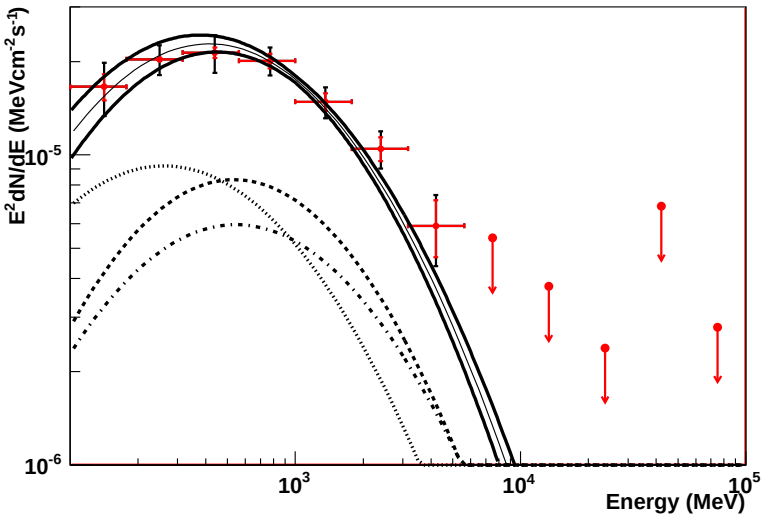

Figure 4.5: Spectral energy distribution of the gamma-ray emission from HB 21 modeled as a flat circle of 1.125° radius. Red error bar is statistical uncertainty. An additional systematic uncertainty of 10% ($E < 560$ MeV) and of 5% ($E > 560$ MeV) is represented by the black error bar. The solid thin black curve is the log-parabola (equation 4.3) used to model the overall spectrum. Curves with extreme values of α and β, within statistical uncertainty are also shown (solid thick black curves). Dotted, dashed, and dash-dotted curves are the best spectral descriptions for segments NW, S, and NE respectively (see table 4.2).

Table 4.2: Spectral analysis of the different circle segments above 100 MeV.

Segment	LR	Flux $[10^{-8}\mathrm{cm}^{-2}\mathrm{s}^{-1}]$	$\alpha\,(a)$	$\beta\,(a)$	E_{max} [GeV] (b)
Global	0	17.5 ± 0.2	2.596 ± 0.013	0.338 ± 0.008	0.413 ± 0.011
North-East	90	4.0 ± 0.9	2.41 ± 0.16	0.33 ± 0.09	0.54 ± 0.14
North-West	116	7.6 ± 1.2	2.87 ± 0.15	0.32 ± 0.07	0.26 ± 0.06
South	151	5.3 ± 1.0	2.49 ± 0.13	0.39 ± 0.09	0.53 ± 0.10

(a) Spectral parameters of the log-parabolic spectral shape (equation 4.3).
(b) Energy at which the energy flux is maximum.

significantly to the overall emission. The likelihood ratio values of each of these segments are summarized in table 4.2, along with the flux corresponding to each segment and their spectral parameters. The maximum energy flux is attained at $E_{max} = e^{\frac{2-\alpha}{2\beta}}$ GeV. To evaluate the uncertainty in E_{max}, the uncertainties in α and β were taken into account, as well as their covariance. We found that the segment NW has a softer spectrum, peaking at lower energies than the other two regions (see also figure 4.5).

4.4 Discussion

The luminosity between 100 MeV and 5.6 GeV is $L = (1.34 \pm 0.03_{\mathrm{stat}}) \times 10^{34} (d/0.8\mathrm{kpc})^2$ erg/s. Unless $d = 1.7$ kpc is confirmed, HB 21 belongs to the group of low-luminosity, GeV-emitting supernova remnants, such as Cygnus Loop (Katagiri et al., 2011, and Chapter 5) or S147 (Katsuta et al., 2012), which are clearly less luminous than the first GeV-emitting

supernova remnants that were discovered. For instance, W51C (Abdo et al., 2009*a*), IC443 (Abdo et al., 2010*e*), W49B (Abdo et al., 2010*c*), or Cas A (Abdo et al., 2010*b*) have luminosities $L > 10^{35}$ erg/s. Also the break in energy is found at lower energy in HB 21 than in the case of the luminous supernova remnants.

The absence of nonthermal X-ray emission favors a hadronic origin of the observed gamma-ray emission. Moreover, the rapid steepening of the spectrum above few GeV is the kind of signature expected from the re-acceleration of pre-existing cosmic rays (Blandford and Cowie, 1982; Uchiyama et al., 2010), where high energy cosmic rays escape from the supernova remnant confinement region (Zirakashvili and Aharonian, 2010).

To check the viability of the leptonic and hadronic scenarios from the energetics point of view, we considered the energy from the supernova explosion that is converted into accelerated particles, $W = L \times \tau$. In this expression, L is the gamma-ray luminosity and τ the characteristic cooling time of the dominant accelerated particle type. When the gamma-ray luminosity is *hadronic*-dominated, τ_p is given by equation 2.16, i.e. is basically dependent of the ambient medium density n. According to Koo et al. (2001), cloud S has density $\sim 7000\,\mathrm{cm}^{-3}$, and central evaporating clouds have densities $\sim 4 \times 10^4\,\mathrm{cm}^{-3}$. Moreover, Tatematsu et al. (1990) quote a density of about $100\,\mathrm{cm}^{-3}$ for cloud A. We computed our own estimate of the average density of the region. To estimate the total mass we used the CO data from CfA 1.2 m Millimeter-Wave Telescope (Dame et al., 1987). We assumed a standard linear relationship between the velocity integrated CO intensity, I_{CO}, and the molecular hydrogen column density, $N(\mathrm{H_2})$:

$$N(\mathrm{H_2})/\mathrm{I_{CO}} = (1.8 \pm 0.3) \times 10^{20}\mathrm{cm}^{-2}\mathrm{K}^{-1}\mathrm{km}^{-1}\mathrm{s}^{-1} \tag{4.5}$$

as derived by Dame et al. (2001). This equation yields $M_{\mathrm{CO}}/M_\odot = 1200 S_{\mathrm{CO}} d^2_{kpc}$, where d_{kpc} is the distance to the cloud in kpc, and S_{CO} the CO emission integrated over velocity and the angular extent of the cloud in K km s^{-1} arcdegree^2. We concluded that there are as many as 12000 solar masses of molecular gas coinciding with the gamma-ray emission in the velocity range from -20 to 0 km/s[2]. Assuming that this gas is in a spherical volume of 25 pc diameter, we obtained an average density of about 60 protons per cubic centimeter, and therefore $W_p \sim 4 \times 10^{47}$ erg.

Alternatively, in case the gamma-ray luminosity is *leptonic*-dominated, equation 2.13 leads to a live time $\tau_{brems} \sim 7 \times 10^5$ years for the cooling via bremsstrahlung interactions. The energy budget required to sustain the luminosity of HB 21 is similar to the hadronic interactions, $W_e \sim 3 \times 10^{47}$ erg. If the dominant process was inverse Compton scattering, the application of equation 2.9 to a $E_{e^-} = 3\,\mathrm{GeV}$ electron[3] in a photon field with $\sim 1\,\mathrm{eV\,cm}^{-3}$ energy density, leads to an estimated energy budget for electrons of $W_{IC} \sim 4 \times 10^{50}$ erg. Similarly, the cooling time of electrons due to synchrotron losses is given by equation 2.7. Therefore, an $E_{e^-} = 3\,\mathrm{GeV}$ electron in a typical interstellar magnetic field of $3\,\mu$G would have a live time of $\tau_{sync} \sim 5 \times 10^8$ years. Only with a magnetic field as high as $80\,\mu$G, could the synchrotron losses become efficient enough to make them comparable to the losses due to bremsstrahlung.

Although detailed modeling is needed, our order-of-magnitude estimates favor the view that the high matter density regions surrounding the supernova remnant are more

[2]Byun et al. (2006) show that the majority of the emission is concentrated in the range -20 to 0 km/s. Although there is some emission at higher velocities, at about 3 km s^{-1}, telluric CO emission corrupts the spectra. To avoid this issue, and for simplicity, we took the velocity range -20 to 0 km/s.

[3]Equation 2.9 is meant for inverse Compton scattering in the Thomson regime, which is the case for an electron of 3 GeV as tested here.

likely to dominate the emission process. This is supported further by the coincidence of the gamma-ray bright regions with dense clumps of molecular gas (figure 4.2). In any case, energy budget considerations are not sufficient to distinguish between electron-dominated and proton-dominated scenarios under the assumption that the supernova explosion has a typical energy release of about 10^{51} erg.

Northeast of the circle there is a spot that becomes bright with increasing energy (figure 4.2). There is the possibility that this comes from a somewhat harder gamma-ray emission related to cloud A. As mentioned in section 4.1, cloud A is somehow different to the shocked clouds like N or S. In addition, it is not clear whether cloud A is at 0.8 kpc (as the usual distance assumed for HB 21), or in the background, at 1.7 kpc or more. If we assume that the gamma-ray brightness of cloud A is due to runaway protons from HB 21, we can estimate the maximum distance between the two objects by the relation $R_d = \sqrt{4Dt}$, where $D \sim 10^{28}\,\mathrm{cm^2 s^{-1}}$ (Gabici et al., 2009, equation 11) is the diffusion coefficient of cosmic rays protons of 10 GeV (which originate 1 GeV gamma rays). In this case the separation between cloud A and HB 21 would be roughly 50 pc. Since the distance to cloud A is fairly well known, the physical relation with HB 21 implies that both objects would be nearby, at about 0.8 kpc Byun et al. (and not at 1.7 kpc as suggested by 2006). We note that D is completely unknown, and the 50 pc is not to be taken as a measure of the separation between the cloud and the supernova remnant, but only a suggestion that cloud A is indeed close to the supernova remnant. We cannot conclude the same about the two other clouds (B and C) on the eastern rim detected by Tatematsu et al. (1990). These are dark in gamma rays and therefore they may be more separated from HB 21.

From the $E > 3$ GeV map (figure 4.2d), we see that the majority of the emission in this region comes from a bow-shaped structure that resembles the supernova remnant shell itself. We suggest that the gamma-ray emission from this region originates in the shell itself, or from a molecular cloud (probably cloud NW) that was overtaken at an earlier stage than those producing the emission in the remaining two thirds of the remnant.

Spectral breaks are expected in middle-aged supernova remnants like HB 21 due to the escape of CRs from the confinement region. In HB 21 the break occurs at lower energies than in other similar objects. This could be related to the proximity of very dense molecular clouds to the supernova explosion progenitor, which could have slowed down the shock rapidly (Ohira et al., 2011). Notably, the spectrum from the region related to the bow-shaped emission in the NW peaks at lower energies than the spectrum from clouds N and S. This fact matches the understanding that the most energetic particles related to the supernova remnant may have already escaped the NW region, due to a smaller confinement volume, or because cloud NW was shocked at an earlier stage than clouds N or S. Moreover, in the S/N map above 3 GeV, we see how a spot coincident with cloud A that becomes relatively brighter than the other clouds with increasing energy. We suggest that this is because cloud A is separated from the supernova remnant, and it is now reproducing the spectrum of the supernova remnant at an earlier stage due to particles that diffused away from the shock (Aharonian and Atoyan, 1996).

Therefore, given that HB 21 appears as an extended object even for gamma-ray telescopes, it provides the opportunity to observe the production and diffusion of accelerated particles (most likely protons), from the supernova remnant shell to distant molecular clouds acting as targets.

Chapter 5

Observations of the Cygnus Loop with *Fermi*/LAT and MAGIC

The Cygnus Loop is among the closest supernova remnants to Earth. Its angular size of about 3 degrees poses an observational problem for instruments with a relatively narrow field of view, like the MAGIC telescopes. We found GeV gamma-ray emission from this object with Fermi/LAT coincident with the X-ray shell, and suggested the best candidate region where MAGIC should locate very-high-energy gamma-ray emission. However, in the latter case, we did not detect the object and we placed an upper limit instead.

5.1 Introduction

The Cygnus Loop is the remnant of a core-collapse supernova explosion occurred 14000 year ago (Levenson et al., 1998) at a distance of 540^{+100}_{-80} pc (Blair et al., 2005). In general, the Cygnus Loop blast wave is not breaking out a dense cloud, but running into a wall of atomic gas related to the cavity in which the supernova occurred. While some portions of the shock proceed unimpeded through low density intercloud medium, overdensities in the wall slow down the shock and emit optical emission lines (figure 5.1). Because this emission is diffuse, it becomes more obvious when the line of sight through the front is long, i.e. in the projected edges. The reflected shock propagates through the hot interior, which enhances the X-ray emission in correlation with the optical emission (Graham et al., 1995; Levenson et al., 1996).

X-ray emission from reflection-shocked gas is particularly bright in the east, in the southernmost region of the structure known as NGC 6992 and in the northern part of the Carrot (Miyata and Tsunemi, 2001). The optical emission of NGC 6992 is characterized by an unusual photoionized region in its south, with plasma densities $\sim 60\,\mathrm{cm}^{-3}$ (Levenson et al., 1998). The photoionization implies the presence of soft UV photons related to a slow shock, indicating that the blast wave collided with the cavity in earlier times in this region. Elsewhere in the SNR (except in the breakout) the collision with the wall must have been more recent, so that the SNR has not yet reached the radiative phase. This should be the case in the other bright region at optical wavelengths, NGC 6960. In the west edge of it is where ISM appears to be densest due to the presence of two molecular clouds with mass $\sim 100\,\mathrm{M}_\odot$(Scoville et al., 1977). These clouds almost depict indentations of the west edge of NGC 6960 (figure 5.2), thus suggesting the interaction. The southernmost region of NGC 6960 and southwest quadrant of the supernova remnant

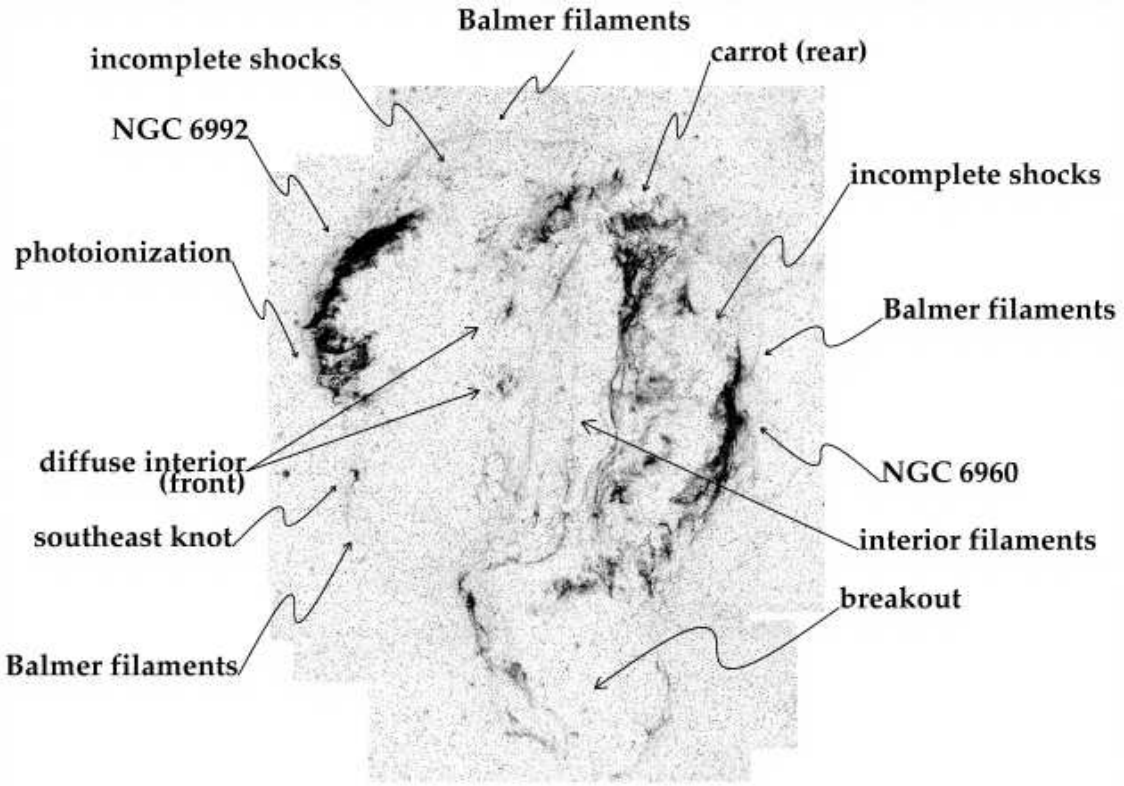

Figure 5.1: Main features of the optical line emission of the Cygnus Loop (Levenson et al., 1998).

presents evidence of a more clumpy interstellar medium (Levenson et al., 1998).

In contrast to the previous two regions, an example of a region with great advance of the blast wave throug a low density medium is the so-called *breakout*, to the south of the supernova remnant. However, Patnaude et al. (2002) reported the presence of a shocked molecular cloud in the western part of the breakout that started to be engulfed by the blast wave as recently as 1200 years ago. Since it breaks tha apparent spherical simmetry of the Cygnus Loop, the breakout also been suspected to be a second SNR. Uyanıker et al. (2002) found that the polarization of the 2695 MHz emission was much higher there with respect to the north of the shell, and suggested that both SNRs could be physically interacting.

Also within the breakout, *Suzaku* and *XMM-Newton* X-ray images revealed what could the neutron star remaining after the progenitor collapse and its pulsar wind nebula (Katsuda et al., 2012). There is yet another compact X-ray object nearby, AX J2049.6+2939, that could be related to the Cygnus Loop, but it is not firmly established as neutron star (Miyata et al., 2001). Pulsations are not detected for any of these objects. In addition, a very high transverse proper motion of $\sim 1300\,\mathrm{km\ s^{-1}}$ is needed if it is assumed that one of these candidate neutron stars departed from the geometric center of the Cygnus Loop 14000 years ago. However, this could be solved if the neutron star was related to the second SNR suggested by Uyanıker et al. (2002).

Provided the proximity, the evolutionary stage, and the interaction with the interstellar medium discussed above, the Cygnus Loop represents a good target for gamma-ray observations. The detection GeV gamma-ray emission from the Cygnus Loop was published in Katagiri et al. (2011). The *Fermi*/LAT counts maps reveal an extended source,

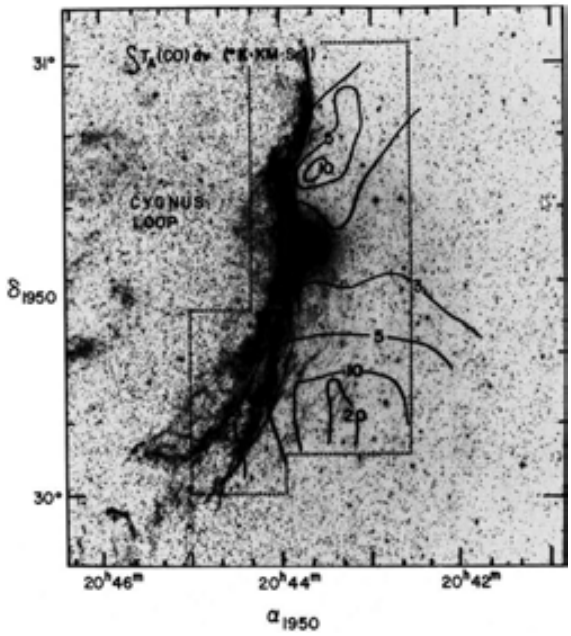

Figure 5.2: Original figure from Scoville et al. (1977), with a detailed view of the the West rim of the Cygnus Loop (marked as NGC 6960 in figure 5.1). Contours represent the molecular hydrogen density as traced by the CO $J = 1 \rightarrow 0$ line emission.

well correlated with the shell seen at other wavelengths (figure 5.3). The spectral modelling reveals a plausible hadronic origin of the observed emission. We discuss this result in section 5.2, in comparison with our own analysis of the public *Fermi*/LAT data. Afterwards, in section 5.3 we report observations with the MAGIC telescopes of a region containing NGC 6960 and the clouds reported by Scoville et al. (1977).

5.2 Observations with *Fermi*/LAT

We analysed *Fermi*/LAT Pass-7 data corresponding to the period between August 4^{th} 2008 (start of science operations) and August 8^{th} 2012. Like in section 4.2, we defined the ROI as a circle of 10° radius centered at the position $(\alpha, \delta) = (20^h58^m11^s, 29°23'56'')$, which is 2° displaced towards negative galactic latitudes with respect to the catalog position of the Cygnus Loop. This is done in order to be less affected by the diffuse emission from the Galactic plane. Data were processed with the version v9r27p1 of the *ScienceTools*. We selected class 2 events in the energy range between 100 MeV and 100 GeV, with the recommended quality cuts (including the requirement for the spacecraft to be in normal operation mode, LAT_CONFIG==1, data to be flagged as good quality, DATA_QUAL==1, and a cut on the rocking angle of the spacecraft, ABS(ROCK_ANGLE)< 52°). In addition, we applied a zenith angle cut of 100° in order to prevent event contamination from the Earth limb. Data were binned in sky coordinates with the `gtbin` tool, using square bins of 0.125° side.

We performed a binned likelihood analysis with a model containing the standard galactic and extragalactic diffuse emission models provided in the *ScienceTools*, plus the sources in the 2FGL catalog lying up to 15° away of the ROI center. The Cygnus Loop is included in the 2FGL catalog as a uniform ring. However, the extended source template

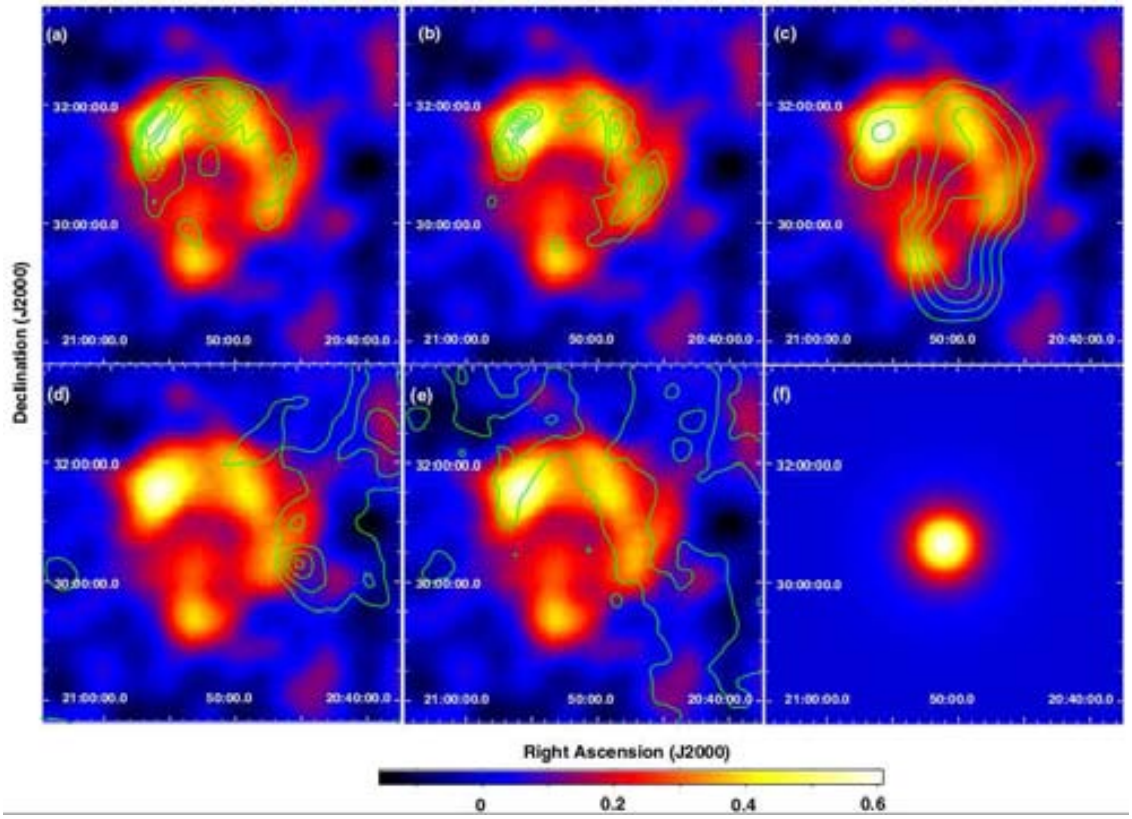

Figure 5.3: Residuals map of the Cygnus Loop between 0.5 and 10 GeV, extracted from Katagiri et al. (2011). Green countours represent the emission at other wavelengths: a) ROSAT X-ray count map from 0.1 to 2 keV; b) Hα image from the plate POSS-II F (red) of the Digital Sky Survey; c) 1420 MHz ratio continuum emission (Reich, 1982); d) ^{12}CO ($J = 1 \rightarrow 0$) integrated for velocities from -25 to +30 km s^{-1} (Dame et al., 2001); e) The 100 μm infrared intensity map from IRAS (Beichman et al., 1988); f) The LAT PSF in the energy band of the residuals map assuming a spectral index of 2.5.

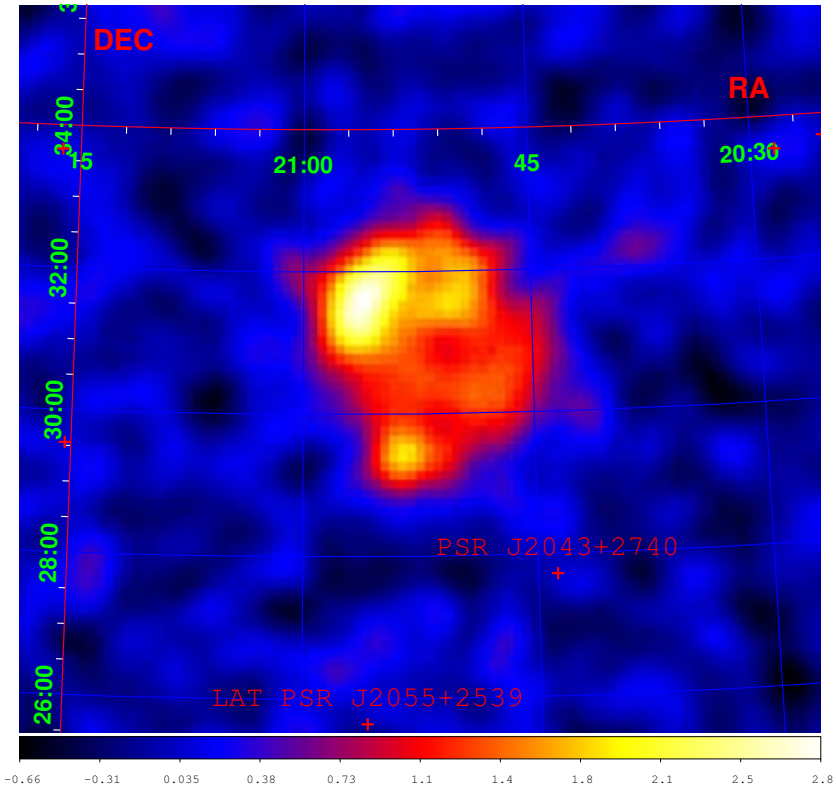

Figure 5.4: S/N map of the null hypothesis at energies above 500 MeV. The map was smeared with a 0.5° Gaussian kernel for better comparison with figure 5.3. Red crosses represent sources in the vicinity of the Cygnus Loop included in the 2FGL catalog.

provided in the *ScienteTools* is centered at a position displaced 0.2° north of the catalog position of the Cygnus Loop and another 0.2° west with respect to the 2FGL catalog position, which was optimized in Katagiri et al. (2011). We relied on the position and size of the ring suggested by Katagiri et al. (2011), and produced our own template adapted to the pixel size of this analysis. The outer/inner radii of the ring are 1.6/0.7 degree, centered at $(\alpha, \delta) = (20^h51^m, 30°50')$.

We produced the S/N maps including the sources mentioned above and we realised that there was a residual signal on the Galactic plane, close to the edge of the ROI, more than 4° away from the southwest rim of the Cygnus Loop. To avoid any possible interference with the analysis of the Cygnus Loop, we added a point-like source in the model at the position $(\alpha, \delta) = (20^h27^m18^s, 27°58'43'')$. This source by itself has a TS = 37 in this analysis, and its position (which was not optimised so far) is consistent with the cataclysmic variable star QU Vul. Although we acknowledge the importance of this possibility, the nature of the additional source will not be addressed in this work.

The model with the point-like sources (including the newly found one) plus the Galactic and extragalactic backgrounds was regarded as the *null hypothesis*. The S/N maps produced with the null hypothesis are shown in figures 5.4 and 5.5. Next, we compared the maximum likelihood obtained with the null hypothesis to those for several models including different morphological and spectral descriptions of the Cygnus Loop. The optimisation procedure was done in two steps as in section 4.2.

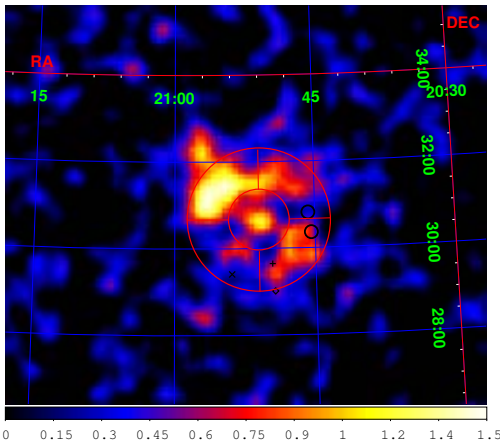

(a) 100 MeV$< E <$ 500 MeV

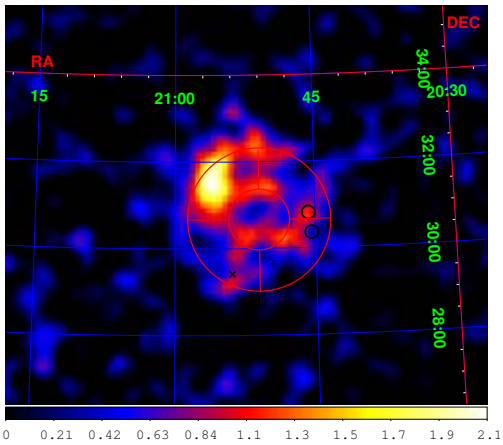

(b) 500 MeV$< E <$ 1000 MeV

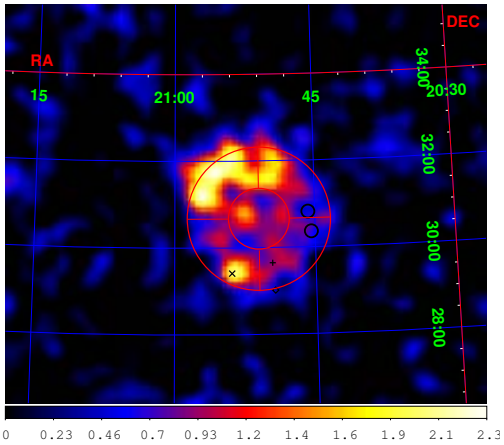

(c) 1000 MeV$< E <$ 5000 MeV

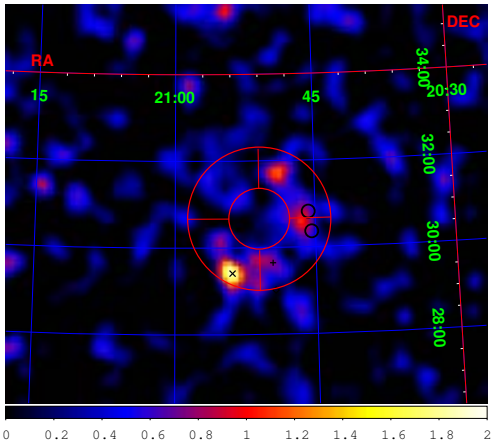

(d) $E >$ 5000 MeV

Figure 5.5: S/N maps of the null hypothesis in different energy ranges. The ring used in the modelling, as well as its divisions are shown in red. Black circles represent the positions CO density peaks extracted from figure 5.2. The $\diamond$ and the $+$ symbol mark the position of the compact X-ray sources discovered in Katsuda et al. (2012) and Miyata et al. (2001) respectively. The $\times$ symbol marks the point-like source J2053.9+2924 (see discussion in the text).

Table 5.1: Spectral analysis of the different arcs of the ring above 100 MeV. The likelihood ratio $-2\log(\mathcal{L}_{arc}/\mathcal{L}_{ring})$ of each arc was evaluated with respect to the likelihood of the whole segmented ring. α and β are the spectral parameters of the log-parabolic spectral shape (equation 4.3). The integral flux and the energy at which the energy flux is maximum (E_{max}) are also shown. To evaluate the uncertainty in E_{max}, the uncertainties in α and β were taken into account, as well as their covariance. The parameters of J2053.9+2924 were obtained by substituting the SE arc by a point-like source.

Arc	LR	Flux $[10^{-8}\mathrm{cm}^{-2}\mathrm{s}^{-1}]$	α	β	E_{max} [GeV]
Whole ring	0	11.4 ± 0.6	2.15 ± 0.03	0.18 ± 0.03	0.66 ± 0.06
NE	507	4.4 ± 0.5	2.31 ± 0.07	0.39 ± 0.06	0.67 ± 0.07
NW	172	4.0 ± 0.7	2.21 ± 0.08	0.09 ± 0.05	0.3 ± 0.3
SW	116	2.3 ± 0.6	2.11 ± 0.10	0.06 ± 0.05	0.4 ± 0.5
SE	80	0.8 ± 0.3	1.68 ± 0.17	0.16 ± 0.08	2.8 ± 1.2
J2053.9+2924	118[a]	0.8 ± 0.3	1.88 ± 0.16	0.09 ± 0.07	1.8 ± 1.2

[a] For this point-like source, its TS as independent source is shown instead of the likelihood ratio.

We first tested the ring template. In the 2FGL catalog, a power-law with exponential cutoff (equation 4.4) spectrum is suggested as spectral shape (Nolan et al., 2012). However, Katagiri et al. (2011) found that a log-parabolic shape (equation 4.3) achieved the best fit. We tested both possibilities, resulting in a TS of 1476 for the exponential cutoff versus 1501 for the log-parabola (for the same number of degrees of freedom). Therefore, we adopted the log-parabola as global spectral shape for the rest of the analysis. The spectral parameters of the global emission are $\alpha = 2.15 \pm 0.03$, $\beta = 0.17 \pm 0.03$, which means that there is a maximum in the spectral energy distribution at $E_{max} = (0.66 \pm 0.06)$ GeV. The total flux in the *Fermi*/LAT energy band is $(1.14 \pm 0.06) \times 10^{-7}\mathrm{cm}^{-2}\mathrm{s}^{-1}$.

Following Katagiri et al. (2011), we also considered possible spectral variations of different parts of the shell. For that, we divided the ring in four arcs of 90 degree each (NE, NW, SW and SE). In a first step we tested the four arcs together with fifth region corresponding to the inner circle of 0.7 degree radius and verified that interior does not contribute significantly by itself (TS$\sim$ 7). Therefore, we proceeded by adding the four arcs alone, which means adding 12 parameters (α, β and flux normalisation for each arc) to the null hypothesis. The TS of the source modeled with these additional degrees of freedom is 1657. The spectal parameters of each section are summarized in table 5.1. These results are not straightforward to compare with the equivalent analysis from Katagiri et al. (2011), who opted for computing the spectral index of a simple power-law above 500 MeV. However, we note that the maximum of the emission occurs at an energy higher than this, and therefore we consider that our approach is more meningful.

The highly curved global spectral shape (figure 5.6) is dominated by the bright emission of the arc NE at low energies. This region emits a flux of $(4.4 \pm 0.5) \times 10^{-8}\mathrm{cm}^{-2}\mathrm{s}^{-1}$ above 100 MeV, which represents a 39% of the emission of the whole ring. However, we note that the other three arcs have a β parameter less than 2 sigma away from zero. In these parts of the ring, the less curved spectrum made the location of the maximum energy, E_{max}, more uncertain. Special attention was paid to the SE arc, which shows completely different spectral parameters compared to the rest of the shell. This fact, together with the morphology observed above 5 GeV (figure 5.5d) made us consider the possibility that the emission from the southeastern region comes from a point-like source, precisely at the location of the breakout, where the shell emission at all wavelenths is more tenuous.

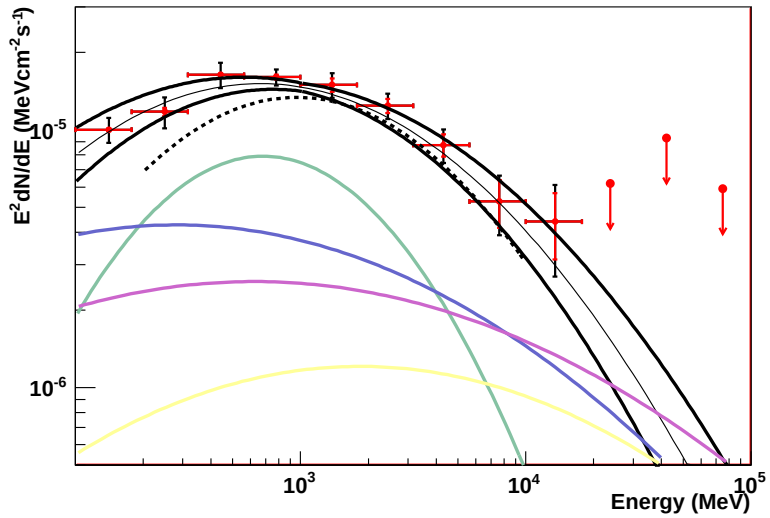

Figure 5.6: Spectral energy distribution of the Cygnus Loop modeled as a uniform ring (red points). Black error bars represent the systematic uncertainty, to be added to the statistical uncertainty (in red). Those bins where the Cygnus Loop has TS< 10 are converted to upper limits. The black, solid curve is the log-parabola obtained from the global fit, and the thicker curves the range allowed by the statistical uncertainty in the spectral parameters. The spectral energy distribution obtained by Katagiri et al. (2011) is shown as a dashed curve. Color curves are the best log-parabolic fits to the spectra of the NE (green), NW (blue) and SW (violet) arcs. The spectrum obtained J2053.9+2924 is shown in yellow.

We located the the point-like source at $(\alpha, \delta) = (20^h53^m55^s,\ 29°24'45'')$ using the tool `gtfindsrc`. The estimated uncertainy in the position is 0.01°. Substituting the SE arc by this point-like source (which we tentatively name J2053.9+2924), the global TS improved from 1657 to 1690 (for the same number of degrees of freedom). Moreover, J2053.9+2924 obtains TS = 120 if considered as an independent source. The spectral parameters are compatible within uncertainites with those from arc SE. A baricenter-corrected Fourier analysis with the tool `gtpspec` did not reveal any peak in the frequency power spectrum that could indicate the presence of a pulsar. The scanned range was between 0.01 and 50 Hz with a frequency resolution of 0.0001 Hz. We also checked the long-term variability by means of a lightcurve bined in one month intervals. The emission during the four years of observations remained completely stable, with a fit to a constant returning $\chi^2 = 45.1$ for 48 degrees of freedom.

We performed a dedicated likelihood analysis above 3 GeV considering the three spots remaining in figure 5.5d as point-like sources. One of the point-like sources is the J2053.9+2924 discussed above. The other two, which we name J2046+3033 and J2049+3141, were placed at $(\alpha, \delta) = (20^h46^m34^s,\ 30°33'00'')$ and $(\alpha, \delta) = (20^h49^m06^s,\ 31°41'13'')$ respectively. A power-law spectrum was assumed in all cases. J2046+3033 coincides with the high-density molecular clouds discussed in Scoville et al. (1977), whereas J2049+3141 is placed in the North, on a bright X-ray knot where the presence of reflection-shocked gas was reported (Miyata and Tsunemi, 2001). We find that J2053.9+2924 and J2046+3033 are still significant at these high energies (TS equal to 66 and 33, respectively), whereas J2049+3141 is at the edge of detection (TS = 21). The fluxes and spectral indices Γ for the three sources are listed in table 5.2. We note that the spec-

Table 5.2: TS, photon flux and spectral index of the point-like sources defined from the residual emission in figure 5.5d.

Source	TS	Flux[b] $[10^{-10}\mathrm{cm}^{-2}\mathrm{s}^{-1}]$	Γ
J2046+3033	33	2.8 ± 0.5	2.13 ± 0.07
J2049+3141	21	2.1 ± 0.5	2.60 ± 0.09
J2053.9+2924	66	3.3 ± 0.5	2.16 ± 0.06

[b] Photon flux above 3 GeV.

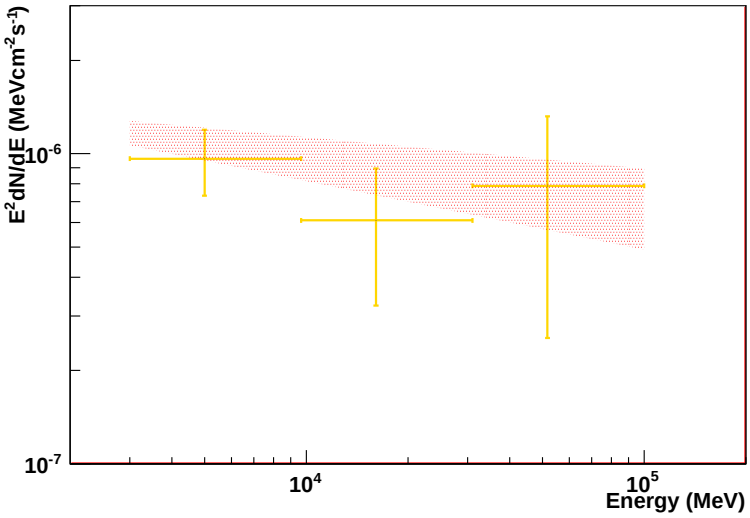

Figure 5.7: High energy power-law tail of the emission of the point-like source J2053.9+2924 (shaded area). The TS of each point, from low to high energy, are 40, 14 and 11. In the last point, the flux is only about 1.5 times the uncertainty.

trum of J2049+3141 is relatively steep, whereas J2046+3033 and J2053.9+2924 present a nearly flat spectral energy distribution.

The possibility to measure parts of the Cygnus Loop emiting at energies close to the VHE regime lead us to divide the energy band from 3 GeV and 100 GeV in three bins in energy and attempt a flux measurement of J2046+3033 and J2053.9+2924 in these bins. The flux of J2046+3033 is measurable (TS$>$ 10) only in the first bin, up to $\sim$ 10 GeV. This result is discussed in section 5.3 together with the MAGIC observations. Remarkably, J2053.9+2924 was measured up to 100 GeV (figure 5.7).

5.3 Observations with the MAGIC telescopes

The Cygnus Loop was observed with the MAGIC telescopes between July and November 2010. Given the large angular diameter of the Cygnus Loop, a very time-consuming scan would be needed in order to map it completely. Instead, we proposed to observe the region where VHE gamma-ray emission could be most probably expected, before knowing the results from *Fermi*/LAT (Katagiri et al., 2011) and the detection of a possible PWN (Katsuda et al., 2012). This region is the West rim of the supernova remnant, including the molecular clouds possibly interacting with it.

A crude estimate of the flux that could be expected from that region was guessed as follows: assuming that the Cygnus Loop is similar to IC 443 in terms of evolutionary stage and supernova explosion energy, the luminosity in gamma rays from neutral pion decay is approximately proportional to the proton density in ambient medium (section 2.3.3). The density in Scoville's clouds is about $100\,\mathrm{cm}^{-3}$, whereas in IC 443 it is one order of magnitude higher (Rosado et al., 2007). On the other hand, the distance to IC 443 is 1.5 kpc (Welsh and Sallmen, 2003), which is a factor 3 farther away than the Cygnus Loop. Therefore, the intrinsically lower luminosity of the Cygnus Loop should be compensated by the lower geometrical dilution, and the flux received on Earth should be of the same order. According to previous MAGIC observations, the VHE flux of IC 443 is $\sim 6.5\%$ that of the Crab nebula above 100 GeV (Albert et al., 2007*a*). With such a flux, a point-like source of gamma-rays should be readily detectable with the MAGIC telescopes.

As mentioned in section 3.2, the normal data-taking mode in MAGIC is the so-called *wobble* mode, where the telescopes point towards a direction slightly offset from the source of interest. This allows a symultaneous background estimation in the same field of view. In this case we planned the observations so that the telescopes would wobble around the position $(\alpha, \delta) = (20^h45^m34^s, 30°35'33'')$ along the right ascension axis. Scoville's clouds (figure 5.2) are approximately oriented North-South, equidistant $\sim 0.24°$ to the central position. Since we the exact position where the gamma ray emission could arise was not know, we decided to redefine the telescope pointing position after the first two months of data taking. The new position $(\alpha, \delta) = (20^h45^m41^s, 30°33'00'')$ is just $\sim 0.18°$ southwest to the previous one, and was defined by the highest positive fluctuation in the significance map produced with the data from July and August.

Data were often taken in adverse weather conditions, especially during summer. A total 31 hours (live time) of data passed quality cuts. A threshold of 190 GeV was estimated from Monte-Carlo simulation of diffuse gamma-rays. The relative flux map resulting from the whole observation (at all energies above the threshold) is shown in figure 5.8a.

Since no signal was detected, we computed an upper limits to the gamma-ray emission from a region of 0.25° radius centered at the above mentioned source J2046+3033 (figure 5.9). This region contains the *Fermi*/LAT residual emission above 5 GeV, as well as a big fraction of the high density material found by Scoville et al. (1977).

5.4 Discussion

We performed the measurements of the gamma-ray emission from the Cygnus Loop in the widest energy range measured so far for this object. Our analysis of the *Fermi*/LAT data shows that the lumnosity of the Cygnus Loop in gamma rays above 100 MeV is $L = (5.58 \pm 0.13_{\mathrm{stat}}) \times 10^{33}(d/540\mathrm{pc})^2\,\mathrm{erg/s}$. This estimate is a factor 5 higher than the reported in Katagiri et al. (2011). The energy at which we measure the maximum emission from the Cygnus Loop is (0.66 ± 0.06) GeV. This energy is significantly lower than the one found by Katagiri et al. (2011), who found the maximum at (0.96 ± 0.05) GeV. To explain these discrepancies, we note the main differences between the two the two analyses, namely: a) we have doubled the ammount of data analyzed; b) we have used Pass 7 events with updated instrument response functions, whereas at the time of the analysis by Katagiri et al. (2011) only Pass 6 were available; c) we have used the latest models for galactic background (which include the Fermi bubbles and other spatial features not included in the outcome of Galprop), and we have modeled the background sources relying in the 2FGL catalog, whereas Katagiri et al. (2011) had to use the First Year catalog,

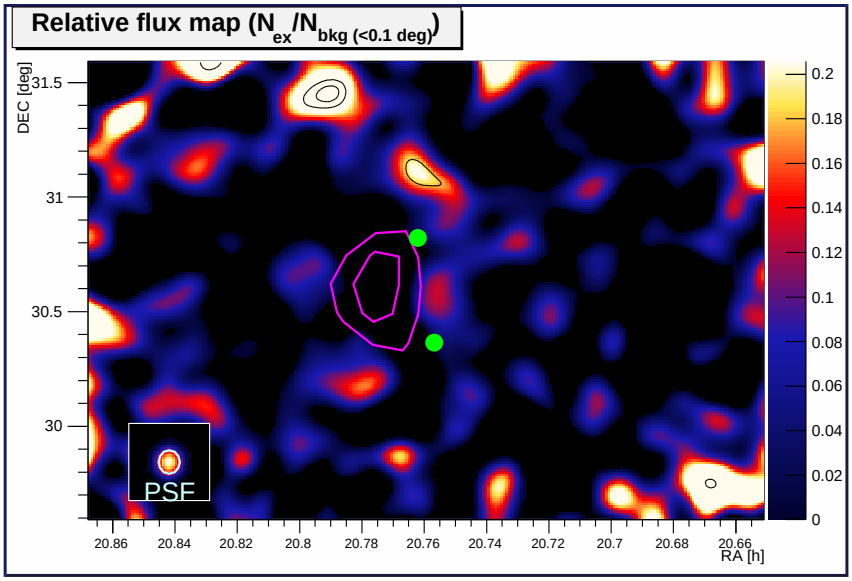

(a) Relative flux map (number of excess events over the background in a 0.1° region) above 190 GeV. Black contours represent test statistic starting at starting at 3 and increasing by 0.5 per contour. Magenta contours depict the residual emission detected above 5 GeV in the *Fermi*/LAT observations (figure 5.5d). Green circles mark the position of the peaks of the CO distribution shown in figure 5.2.

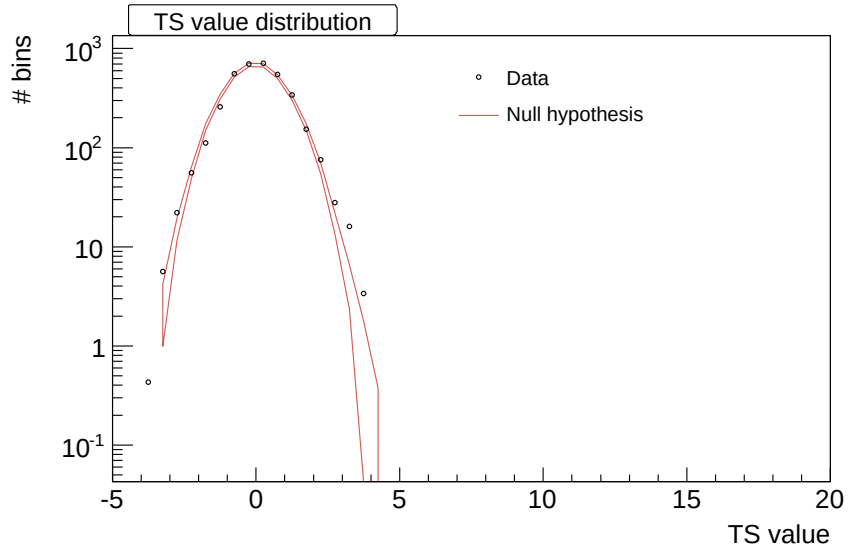

(b) Distribution of the test statistic used to evaluate the significance of the excess of gamma-like events. This test statistic is Li&Ma significance applied on a smoothed, modelled background distribution. In pink is shown the distribution expected from the null hypothesis, which reduces to a Gaussian function when Li&Ma assumptions are fulfilled. The distribution of significances of the map above (black points) do not deviate significantly from the null hypothesis.

Figure 5.8: Relative flux map and test statistic distribution of the MAGIC observations of the southwest rim of the Cygnus Loop.

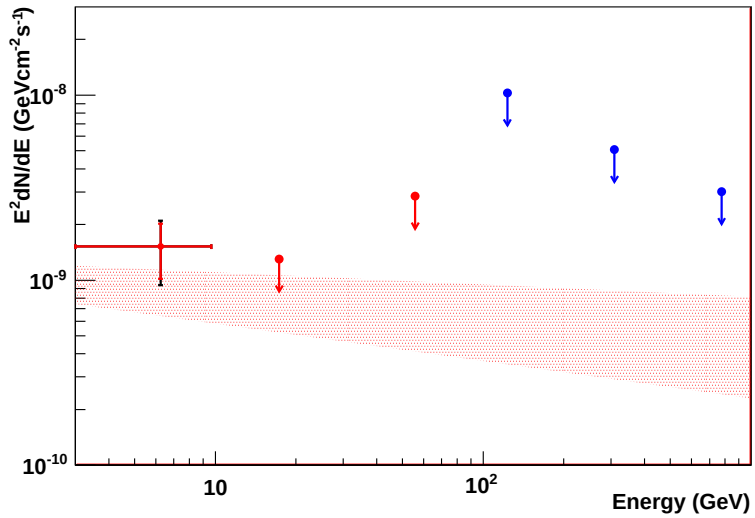

Figure 5.9: Upper limits to the VHE gamma-ray emission from the sothwest rim of the Cygnus Loop resulting from the observation with the MAGIC telescopes (blue markers). Red markers show the highest energy measurements of J2046+3033 with *Fermi*/LAT. The first *Fermi*/LAT point has TS = 22. The second and the third *Fermi*/LAT points have TS = 8 and TS = 3, respectively, and are converted to upper limits. The red shaded area represents the extrapolation of the power law measured from 3 to 100 GeV.

1FGL. We consider that for these reasons our modelling is potentialy more accurate. Especially points (b) and (c) afect the background estimation at low energies, which is where the discrepancy between the two analyses is bigger, and where the maximum emission occurs.

We verified that the central region of the Cygnus Loop does not contribute significantly to the overall emission, thus confirming the limb-brightened morphology that is observed at other wavelengths. The gamma-ray emission is dominated up to a few GeV by the northeast of the SNR. This part shows clearly distinct properties from those of the western half of the remnant. Since the modelling by Katagiri et al. (2011) favored an hadronic origin of the observed emission, we suggest that the observed spectral differences between different parts of the remnant are originated by differences in the interstellar medium. In particular, the blast wave in the northeast must have been heavily damped by an early collision with high density material, probably related to the progenitor cavity wall. As a consequence, the SNR may have evolved more rapidly there, and may be approaching the radiative phase, as suggested from the optical observations (Levenson et al., 1998). The spectrum is noticeably curved in the northeast, with a low energy break like that of HB 21. On the other hand, the west rim has a flatter spectrum, nearly compatible with a power-law of index 2, which meets the prediction from standard nonlinear shock acceleration (Malkov and O'C Drury, 2001). Remarkably, the emission remaining above 5 GeV coincides with a molecular cloud which is not shocked, but is probably in the vicinity of the SNR.

The southeast region deserves a special consideration. We consider that the emission in that region is dominated by the point-like source that we have named J2053.9+2924. This position is not coincident with any particular know feature of the interstellar medium,

such as a compact, shocked molecular gas clump. Neither J2053.9+2924 coincides with previous X-ray sources claimed to be the compact object related to the Cygnus Loop supernova event (Katsuda et al., 2012; Miyata et al., 2001). However, the additional point-like source we propose is coincident with the unidentified X-ray and infrared source 2E 2051.7+2911 (Haakonsen and Rutledge, 2009). We checked the possibility that J2053.9+2924 is a pulsar, with negative results. Moreover, we were able to measure the flux up to 100 GeV, and (althoug statistics are poor) there is no indication that it deviates from power-law spectrum of index 2.16 ± 0.06. We note that a cutoff or a spectral steepening is to be expected above a few GeV. The coincidence with an X-ray and infrared object, raises the possibility of an AGN or a binary system in the background. No long term variability was observed so far, but other time scales are possible. The check of this possibility requires the existence of short, bright flares that could distinguish this faint source clearly above the diffuse background generated by the SNR.

The observed luminosity confirms the Cygnus Loop as the least luminous SNR observed so far at gamma-ray energies. The supernova explosion was probably unleashed by a modest B0 star of $\sim 15\,M_\odot$, and released 2×10^{50} erg (Levenson et al., 1998). This represents about $1/10^{th}$ of the typical energy release of a type Ia supernova explosion. Also the X-ray source identified as the PWN associated to the Cygnus Loop has a low spin-down power, $\dot{E} \sim 2.6 \times 10^{35} (d/540\mathrm{pc})^2\,\mathrm{erg/s}$ (Katsuda et al., 2012). The limited amount of energy available after this supernova has to have a relation with the limited energy budget of the accelerated particles generating the gamma-ray emission. However, this limitation does not seem to have an impact in the spectrum, which is as hard as expected from the nonlinear diffusive shock acceleration theory (except in the northeast of the shell).

The assumption that the Cygnus Loop could have similar properties as IC 443 (which is a much more powerful SNR) lead to the overestimation flux that could be detected with the MAGIC telescopes, especially taking into account that the emission from the whole SNR could not be observed due to its large extension. All in all we consider that the best candidate spot where VHE emission could arise was correcly identified, provided the data available at the time of the observation with the MAGIC telescopes. An upper limit to the VHE emission of the Cygnus Loop was placed for the first time. After the analysis of the *Fermi*/LAT data reported here, the hard source J2053.9+2924 represents a better target for Cherenkov telescopes, although it may be unrelated to the SNR.

Chapter 6

A cosmic-ray acceleration site in the supernova remnant W51C

The W51 complex was observed with the MAGIC telescopes from May 2010 and June 2011. Gamma-ray emission from this region was discovered by Fermi/LAT(between 0.2 and 50 GeV) and H.E.S.S.(> 1 TeV). Observations from these two instruments could not pinpoint the location of the emission to any particular object in the region. However, the modeling of the spectral energy distribution presented by the Fermi/LAT collaboration suggested an hadronic-dominant emission mechanism. The MAGIC observations added further evidence to the hadronic nature of the emission mechanism, and located the centroid of the VHE gamma-ray source in the interaction region between the supernova remnant W51C and the dense molecular gas in the star-forming region W51B. This result (published in Reichardt et al. (2011); Aleksić et al. (2012)) is now considered among the best evidences for a pion decay spectrum generated by cosmic rays.

6.1 Introduction

W51 is a massive molecular complex located at the tangential point ($l = 49°$) of the Sagitarius arm of the Galaxy, at a distance of $\sim 5.5\,\mathrm{kpc}$ (Sato et al., 2010). As seen in 21 cm radio continuum images, three main components are identified: the star-forming regions W51A and W51B and, attached to the SE boundary of W51B, the synchrotron-dominated shell of the SNR W51C (figure 6.1). The estimated age of this SNR is 30000 years (Koo et al., 1995).

The X-ray emission of W51C is center-filling and thermal except for a hard, compact feature in the SW of the shell 6.2a. This object (named CXO J192318.5+140305) was first resolved by *ASCA* (Koo et al., 2002) and later confirmed by *Chandra* (Koo et al., 2005). It consists of a core elongated N-S with an extent of $0.5' \times 1'$, or $0.8 \times 1.6\,\mathrm{pc}$ at a distance of 5.5 kpc. At the center of the core, there is a central compact source (inset in figure 6.2b). The core is located in the middle of the envelope, which has an extent of $4.0' \times 1.5'$ ($\sim 6 \times 2\,\mathrm{pc}$). The spectrum can be fitted by a power law with index 1.82. Both the morphology and the spectrum are consistent with a pulsar wind nebula. If the pulsar was born near the geometrical center of W51C, the age of 3×10^4 years implies a transverse velocity of $360\,\mathrm{km\,s^{-1}}$. Making use of the empirical relation from Seward and Wang (1988), the estimated rotational energy loss is $\dot{E} = 1.5 \times 10^{36}\,\mathrm{erg\,s^{-1}}$. Both the estimated lumminosity and the trasverse velocity have values such that it is

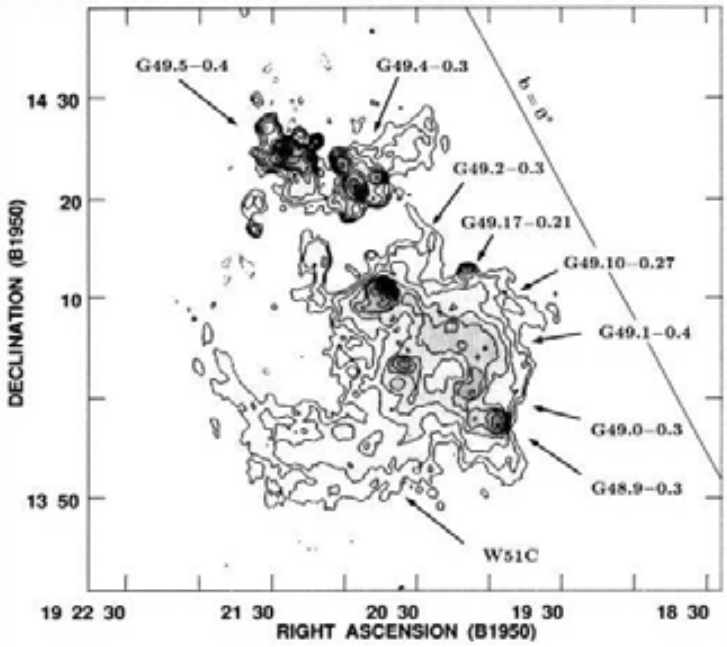

Figure 6.1: 21 cm radio continuum image of the W51 complex from Koo and Moon (1997*a*). HII regions appear as compact radio sources in the star-forming regions W51A (Northern part) and W51B (Eastern part). The shell of the SNR W51C is evident in the SW of the map, and collides with W51B in its Eastern rim.

plausible that CXO J192318.5+140305 is associated to the supernova remnant.

There is conclusive evidence of the interaction between W51B and W51C provided by the detection of about 10^3 solar masses of atomic gas at a velocity shifted between 20 and 120 km s^{-1} with respect to its ambient medium (Koo and Moon, 1997*a*). The high-velocity atomic gas exhibits a counterpart in high density molecular gas clumps. These clumps are spatially coincident with the atomic gas and are also shifted in velocity (Koo and Moon, 1997*b*). The shocked gas is displayed in a thin layer in the interface between the SNR shell and the *unshocked* molecular gas (figure 6.3). This can be taken as the existence of a J-type shock penetrating the dense gas in a particular region of W51B (Koo and Moon, 1997*b*). In the densest regions, the shock becomes continuous (C-type) and 1720 MHz OH masers are detected (Green et al., 1997). Moreover, recent measurements (Ceccarelli et al., 2011) showed over-ionization of the gas in W51B in certain locations close to W51C coinciding with the shocked gas. This excess in ionization implies the existence of an intense flow of freshly accelerated CRs that, through proton-proton collisions, ionize the hydrogen in the adjacent cloud.

An extended source of very high energy gamma rays was first detected by the H.E.S.S. telescopes with an integral flux above 1 TeV of about 3% that of the Crab Nebula (Fiasson et al., 2009). However, the morphological and spectral information was not enough to distinguish the origin of the emission. Also, the Large Area Telescope (LAT) on board the *Fermi* satellite detected an extended source between 200 MeV and 50 GeV coincident with the H.E.S.S. source (Abdo et al., 2009*a*). The modeling of the spectral energy distribution favoured an hadronic origin of the observed gamma-ray emission. Moreover, the reanalysis of the archival MILAGRO data after the release of the first *Fermi* catalog revealed a 3.4σ excess with median energy of 10 TeV coincident with the

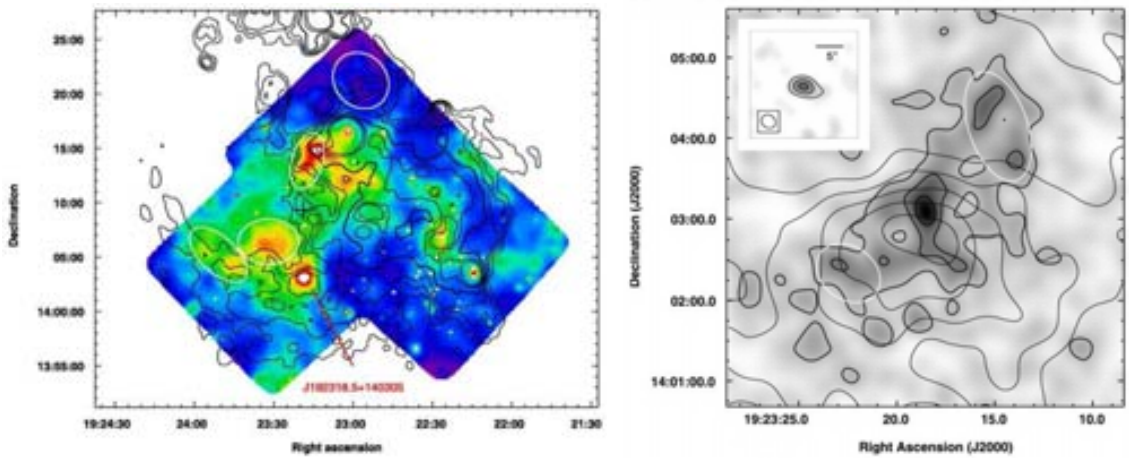

(a) Chandra X-ray intensity image of W51C and W51B (color scale).

(b) Zoom of the hard (2.5-8.0 keV) X-ray emission from the source CXO J192318.5+140305.

Figure 6.2: (a) Overview of the W51 complex in X-rays. The only non-thermal source of X-rays comes from the object marked as J192318.5+140305, which lies on the S edge of the SNR shell. The inset shows the central $20'' \times 20''$ area of the core. In both panels, black, thin contours are 21 cm radio continuum contours (from figure 6.1). White ellipses mark areas used for spectral analysis in Koo et al. (2005).

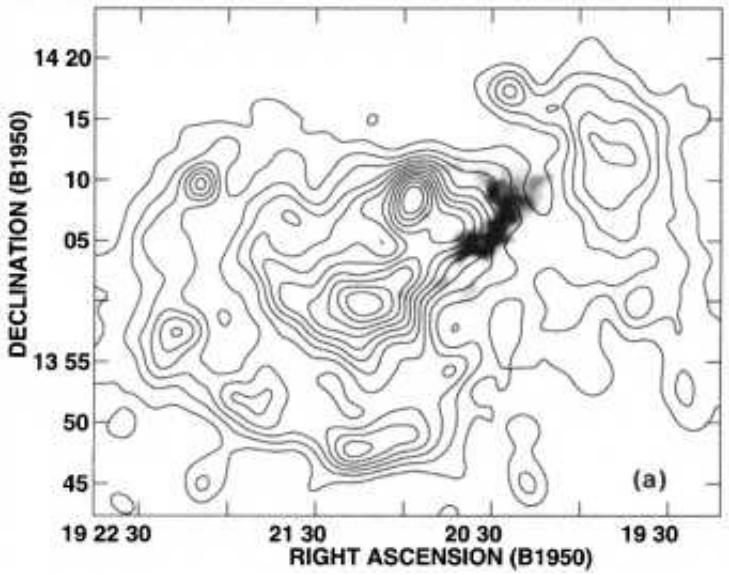

Figure 6.3: X-ray emission of the W51 region from ROSAT observations (contours) together with the high velocity HI in the W51B/C interface (grayscale). Figure extracted from Koo and Moon (1997*a*).

Fermi/LAT source (Abdo et al., 2009*b*). Since W51C is one of the most luminous Galactic sources at *Fermi*/LAT energies, observation of gamma rays up to several TeV have important implications regarding the SNR contribution to the Galactic CRs: such an observation would show that SNRs are not only capable to provide a sufficient flux, but could also shed light on the question of the maximum energy of CRs achievable in such a medium age SNR.

6.2 Observations with the MAGIC telescopes

MAGIC observed the W51 complex in 2010 and 2011. In the first period of observations between May 17 and August 19 2010 about 31 hours effective time remained after quality cuts. Between May 3 and June 13 2011 additional 22 hours effective time of good quality data were taken, resulting in a total amount of 53 h effective dark time. The zenith angle ranged from 14 to 35 degrees. All data were taken in stereoscopic mode, as described in section 3.2.1. The telescopes were pointed to six *wobble* positions around the center of the *Fermi*/LAT source W51C (RA = 19.385 h, DEC = 14.19°), with a *wobble* offset of 0.4°, as it is regularly done in MAGIC observations. Four of the pointing positions accounted for $\sim$ 12 hours each, whereas the remaining two were observed for about two hours each. The data were processed using the standard MAGIC software as explained in section 3.2.2.

6.3 Results

6.3.1 Detection

MAGIC detected the extended gamma-ray source previously reported in the W51 field. Figure 6.4 shows the relative flux map above an energy threshold of 150 GeV produced with the standard MAGIC skymapping tool. The angular resolution of MAGIC at these energies is 0.085° (Aleksić et al., 2011). The map was smeared with a two-dimensional Gaussian function with a sigma equivalent to that of angular resolution. The centroid of the emission, as derived by the fit of a 2 dimensional symmetrical Gaussian function to the map (prior to the smearing), is located at RA= 19.382±0.001 (h); DEC= 14.191±0.015 °. This deviates by 0.04° from the position reported by *Fermi*/LAT, $\mathrm{RA}_{Fermi} = 19.388$, $\mathrm{DEC}_{Fermi} = 14.145$.

The gamma-ray signal was evaluated from the difference in number of gamma-like events *ON* and *OFF* the source. ON means reconstructed within a region defined by an angular distance cut ($\theta^2 < 0.07$ square degrees[1]) around the *Fermi*/LAT emission centroid; and OFF are those events reconstructed in the same region of the camera plane when the telescopes point to each of the other *wobble* pointing positions. For each of the four main pointing positions, an OFF sample was obtained from the average of the 3 OFF regions observed at the same focal plane coordinates but from the complementary pointing positions. This procedure reduces the statistical uncertainty in the OFF estimation. The remaining two positions were observed for a shorter time. We estimated their background separately in order to avoid the introduction of big scaling factors between ON and OFF due to differences in the observing time with respect to the main pointing positions. As a consequence, for these two positions only one OFF sample (from the complementary

[1]This radius is selected in order to include the emission observed in the relative flux map (figure 6.4).

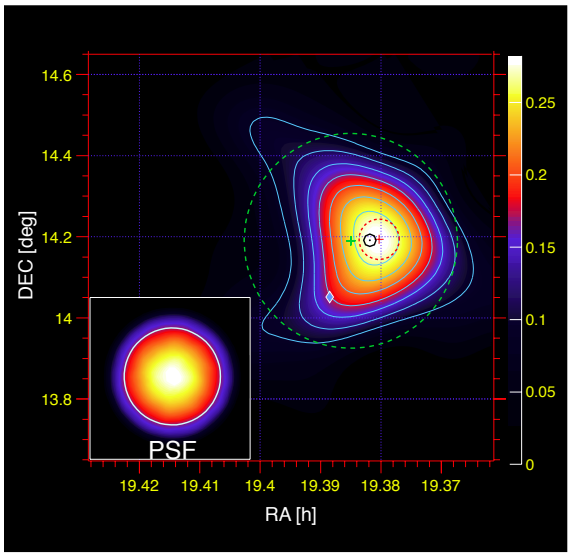

Figure 6.4: Relative flux map above 150 GeV of the W51 field. Test statistics contours are shown in cyan, starting at 3 and increasing by one per contour. The map was smoothed with a Gaussian kernel of 0.085°. The green cross represents the center of the observations (i.e. the centrod of the *Fermi*/LAT source), while the green dashed circle represents the integration area used in figures 6.5 and 6.6. The black dot is the fit position of the centroid, with the statistical uncertainties shown by the surrounding black ellipse. The region of shocked atomic and molecular gas (Koo and Moon, 1997*a*,*b*) is represented by the red dashed ellipse. The blue diamond shows the position of the candidate PWN CXO J192318.5+140305. For reference, the left lower corner inset shows the appearance of a point-like source under a PSF of 0.085° plus the applied Gaussian with a sigma equal to the PSF.

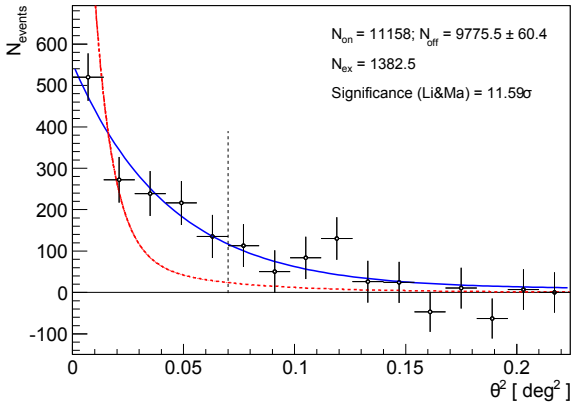

Figure 6.5: θ^2 distribution of the excess events towards the centroid of the emission (back dot in figure 6.4). The excess found in the data was fitted by an exponential function (blue curve) to determine the extension. For comparison, the shape of a point-like source with the same excess determined from Monte-Carlo simulations is shown (red curve).

wobble) was used. An excess of 1371.7 ± 122.5 events was determined from the stacked θ^2 distribution of the six pointing positions. This excess corresponds to a Li&Ma significance of 11.4σ.

To determine the extension of the source, we produced the distribution of excess of gamma-like events in bins of θ^2 (figure 6.5) and we fitted if with an exponential function (corresponding to a Gaussian-shaped source). For comparison, the shape of a point source with the same excess was extracted from Monte-Carlo simulations. After correcting for the angular resolution of the instrument the intrinsic extension of the source was determined to be $0.12 \pm 0.02_{\mathrm{stat}} \pm 0.02_{\mathrm{syst}}$ degrees.

6.3.2 Spectrum

The energy spectrum of the gamma-ray emission between 75 GeV and 5.5 TeV follows a power law of the form:

$$\frac{dN}{dE} = N_0 \left(\frac{E}{1\,\mathrm{TeV}} \right)^{-\Gamma} \tag{6.1}$$

The photon index is $\Gamma = 2.58 \pm 0.07_{\mathrm{stat}} \pm 0.22_{\mathrm{syst}}$, and the normalization factor at 1 TeV is $N_0 = (9.7 \pm 1.0_{\mathrm{stat}}) \times 10^{-13} \mathrm{cm}^{-2} \mathrm{s}^{-1} \mathrm{TeV}^{-1}$, with $\chi^2/\mathrm{NDF} = 5.26/6$ (figure 6.6). The spectral index measured by MAGIC agrees with the one measured by *Fermi*/LAT above 10 GeV, $\Gamma = 2.50 \pm 0.18_{\mathrm{stat}}$ (Paneque D. et al., 2011). The integral flux above 1 TeV is about $\sim 3\%$ of the flux of the Crab Nebula above the same energy, as reported by Fiasson et al. (2009).

In order to derive the spectrum, the effective area was estimated using a Monte-Carlo data set with photons simulated uniformly on a ring of 0.15 to 0.55°distance to the camera center. This accounts for variations of the acceptance across the area of the source. The effect of using this ring Monte-Carlo compared to standard point-like introduces variations in the spectral parameters smaller than the statistical uncertainties. The spectrum was unfolded in order to take into account the finite energy resolution and the energy bias of the instrument (Albert et al., 2007*b*). The systematic error on the flux normalization is 15%, which includes the systematic uncertainties of the effective area (11%) and the

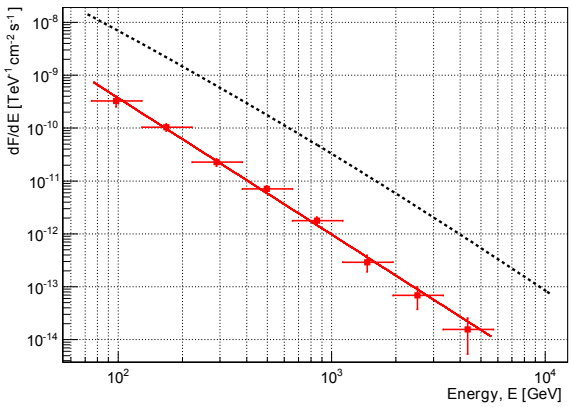

Figure 6.6: Differential energy spectrum of W51 observed by MAGIC. The red points represent the differential flux points after unfolding. The red line represents a power law fit to the data. The error bars represent the statistical uncertainties only. For comparison, the dotted line represents the spectrum of the Crab Nebula as shown in Aleksić et al. (2011).

background calculation. In addition, the systematic uncertainty in the energy scale is estimated to be 17 % at low ($\sim$ 100 GeV) and 15 % at medium ($\sim$ 250 GeV) energies.

6.3.3 Detailed morphology

In order to investigate the detailed morphology of the gamma-ray source in W51, we produced sky maps in two energy ranges: between 300 GeV and 1 TeV, and above 1 TeV (figure 6.7). MAGIC reaches its best sensitivity in the energy range from $\sim$300 to $\sim$1000 GeV. At energies of 300 GeV the angular resolution of MAGIC is 0.075 °and it improves until reaching the saturation value of 0.054 °at energies above 1 TeV (Aleksić et al., 2011).

The source presents an elongated shape, with a tail towards the SE. The maximum of the emission coincides with the shocked-gas region. The determined centroid and extension agree within statistical errors with those found above 150 GeV. Above 1000 GeV the centroid and extension of the emission are in agreement with those obtained at lower energies. The SE tail of the source becomes more prominent, in coincidece with the possible PWN CXO J192318.5+140305. However, the main part of the emission is still coincident with the shocked gas region. We note that, in any case, the VHE emission does not strictly follow the SNR shell (as seen from the 21 cm continuum emission represented by green contours in the right panels), nor does it follow the molecular gas with the velocity expected due to Galactic rotation, as traced by the ^{13}CO (green contours, left panels).

In order to investigate underlying structures, we projected the unsmeared excess event distribution of the source along a line (figure 6.8). The line is 2°long divided in 40 bins with 0.05°width. The orientation of the line is defined by the position of the PWN candidate and the centroid of the shocked clouds identified by Koo and Moon (1997*b*), RA = 19.380 h, DEC = 14.19°. Events within a distance of 2 gaussian sigma of the instrumental PSF to the line were projected. Since the angular resolution is energy dependent, the width of the projected rectangle is 0.3°and 0.216°for the energy ranges from 300 to 1000 GeV and above 1000 GeV, respectively. Background events were estimated from the background model.

The fit the projected event distribution yelds χ^2/d.o.f. of 28/17 for one Gaussian

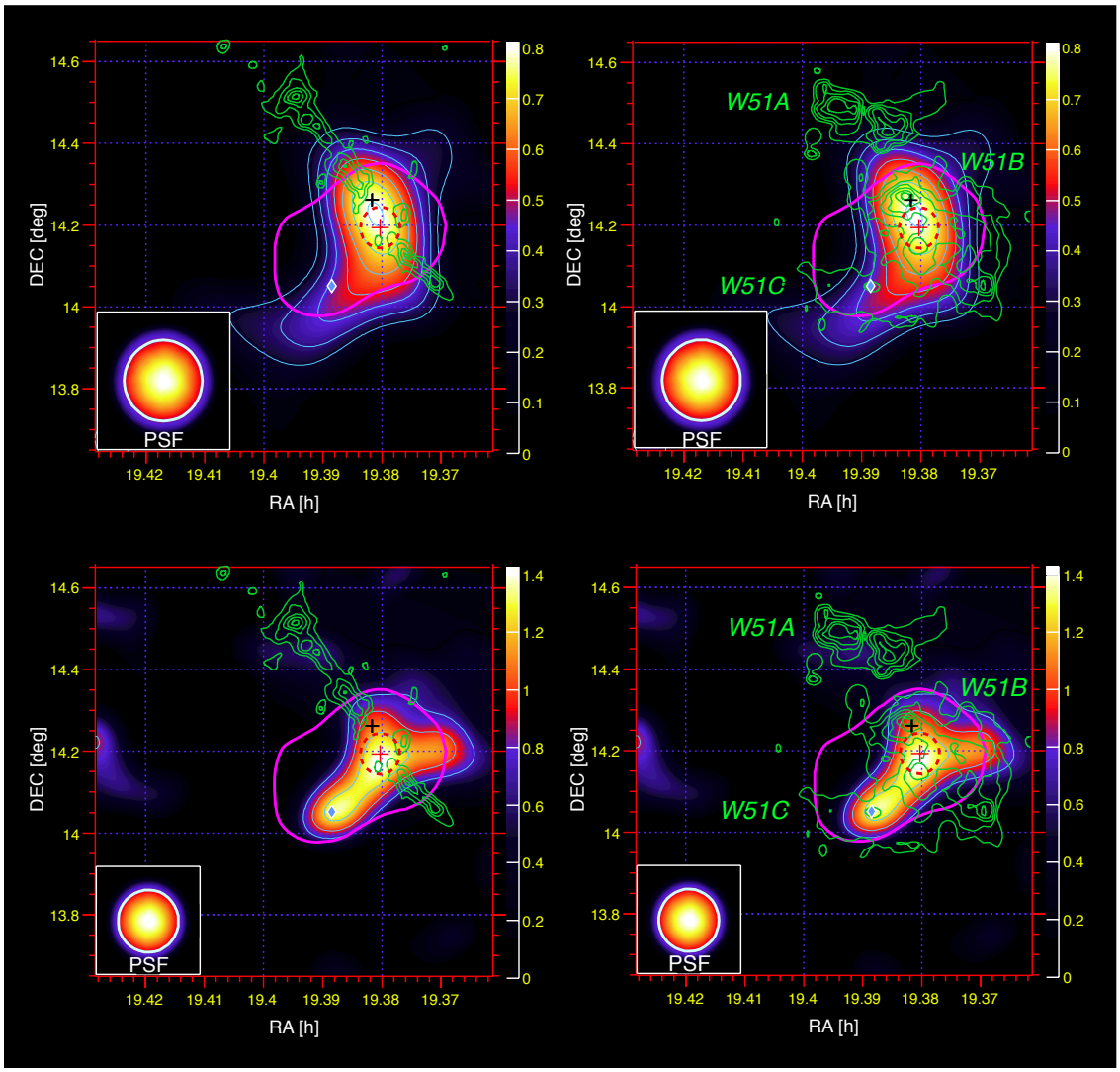

Figure 6.7: Relative flux maps (blue to red color scale) measured with MAGIC. Top panels are maps from 300 GeV to 1000 GeV, and bottom pannels > 1000 GeV. TS contours (cyan) are shown starting at 3 and increasing by one per contour. On the left hand side the MAGIC data are combined with the ^{13}CO (J=1-0) intensity maps from the Galactic Ring Survey (see http://www.bu.edu/galacticring/new_index.html) integrated between 63 and 72 kms^{-1} shown as green countours. On the right hand side the green contours represent the 21 cm radio continuum emission is shown from (Koo and Moon, 1997*a*). In all maps the blue diamond represents the position of CXO J192318.5+140305 and the black cross the position of the OH maser emission (Koo et al., 2005; Green et al., 1997). The red dashed ellipse represents the region of shocked atomic and molecular gas (Koo and Moon, 1997*b*,*a*). The 3 counts contour above 1 GeV determined by *Fermi*/LAT is displayed by the pink contour. All maps were smeared with a Gaussian kernel of a width equal to the angular resolution of the instrument in each energy range. For reference, the gaussian sigma of a point-like source (PSF) after the applied smearing is shown.

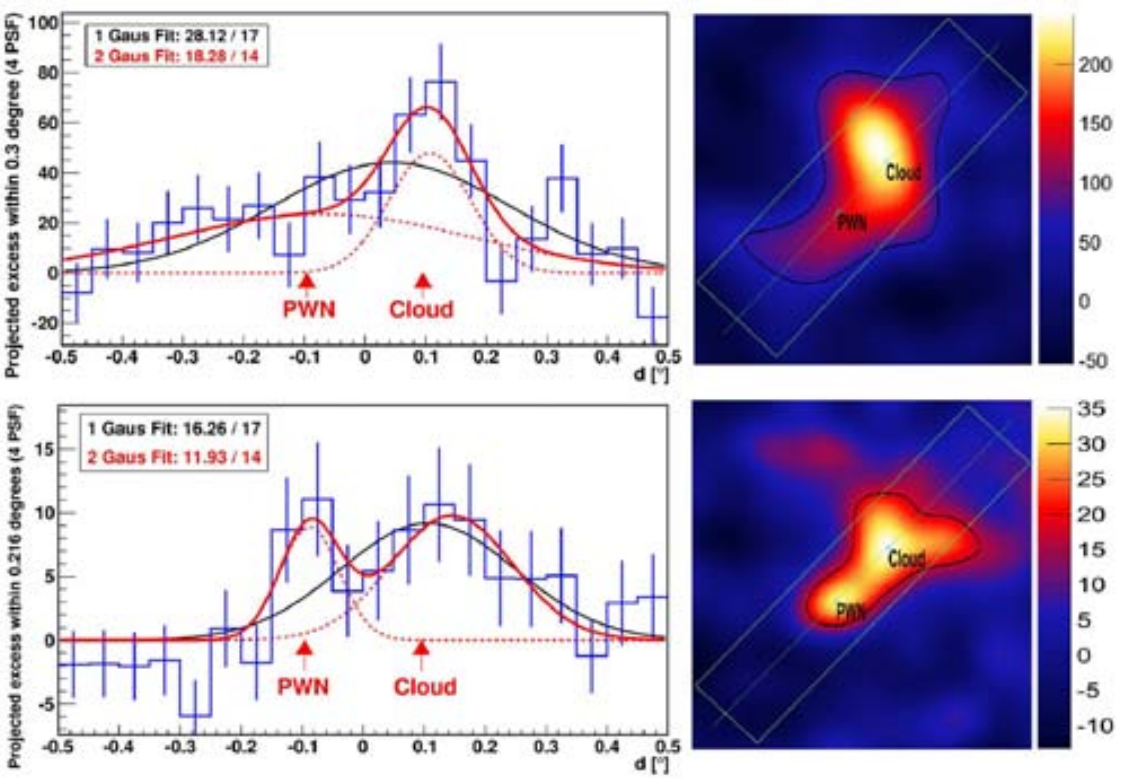

Figure 6.8: Projection of the excess inside the marked box in both differential sky maps: 300 GeV to 1000 GeV (top) and above 1000 GeV (bottom) along the direction connecting the PWN and the shocked-gas region described in Koo and Moon (1997*b*). The projection was done with the unsmeared distribution, although the smeared relative flux maps are shown on the right hand pannels for reference. The black contour stands for the TS=3 isocurve. The excess events distribution was fitted with one (black) and two (red) Gaussian curves. The positions of the shocked gas and the PWN are marked with red arrows. The box has a length of 1°and a width of 4 gaussian sigma of the instrumental PSF.

Table 6.1: Number of excess events determined for the *PWN*-region and the *cloud*-region and their contribution to the overall emission. We did not detect a significant energy dependence on their contributions to the overall excess within the statistical uncertainties.

E[GeV]	*cloud*	*PWN*	*cloud*/all [%]	*PWN*/all [%]
> 300	200 ± 30	132 ± 25	30 ± 5	19 ± 4
> 500	116 ± 17	79 ± 17	32 ± 6	22 ± 5
> 1000	48 ± 10	27 ± 10	43 ± 12	24 ± 10

fuction, and 18/14 for the sum of two Gaussians in the medium-energy range; and 16/17 (one Gaussian) versus 12/14 (two Gaussians) for the high-energy events. In the case of the fit with two Gaussian functions, the centroid of each term coincides within statistical errors with the position of the shocked gas and the PWN. Nevertheless, statistics are not sufficient to clearly discriminate between an extended source of Gaussian excess, an extended source of a more complicated shape, or two individual sources. However, the fact that there is no region of dense gas close to the PWN makes it difficult to explain the enhancement of TeV emission in this area under the assumption of uniform CR density.

6.3.4 Energy spectra of individual regions

A possible scenario of two emission regions could manifest in different spectral behaviours. To quantify the results obtained from the projections, we investigated in more detail the spectral properties of the detected signal in two regions of the source. The first was defined to cover the shocked cloud region with centroid at RA $= 19.380\,\mathrm{h}$, DEC $= 14.19°$; this was called the *cloud* region. The second one was defined by the position of CXO J192318.5+140305 and was called the *PWN* region. To avoid contamination from the surrounding emission, and their possible spread due to the worse angular resolution at lower energies, we used an integration radius of 0.1°. We compared the same analysis on data of the Crab Nebula and found that such a region contained at least 70% of the excess from a point-like source above 300 GeV. The distance between the chosen positions was 0.19°. There was an overlap of only 1.7% in the integration area of each region and, therefore, they were treated as independent. The combined areas of both regions represented about 57% of the area used to determine the overall spectrum.

We determined the amount of excess events of each region above three different energies, and calculated the contribution to the overall emission. The small distance between the regions and the very similar distance to the camera center permitted us to assume the same acceptance of gamma-like events for both regions, at least within 5%. The resulting values are shown in table 6.1. Excesses used to calculate these ratios show a significance of at least 2.9σ.

The contribution to the excess arising from the cloud region is about 30% and shows no dependence on energy. Its spectrum above 350 GeV can be well described by a power law with a flux normalization constant at 1 TeV of $N_{\mathrm{cloud}} = (4.3 \pm 0.9_{\mathrm{stat}}) \times 10^{-13}\mathrm{cm}^{-2}\mathrm{s}^{-1}\mathrm{TeV}^{-1}$. The integrated flux above 350 GeV is equivalent to 1.2% of the flux of the Crab Nebula. The spectral index of the cloud region is $-2.4 \pm 0.5_{\mathrm{stat}}$, which agrees within statistical uncertainties with the spectral index of the overall emission. Under the same assumption of point-like source emission, the flux from the *PWN* region above 350 GeV is equivalent to 0.7% of the flux of the Crab Nebula and represents about 20% of the total flux. The emission between 350 GeV and 2 TeV can be well described by

a power law with a spectral index of $-2.5 \pm 0.6_{\rm stat}$ and a flux normalization at 1 TeV of $N_{PWN} = (2.3 \pm 0.8_{\rm stat}) \times 10^{-13}{\rm cm}^{-2}{\rm s}^{-1}{\rm TeV}^{-1}$. Therefore, the contribution to the excess from each of the regions shows no dependence on energy.

Despite the garish differences in the relative flux map above 300 GeV and above 1 TeV (figure 6.7), we showed that the gamma-ray source presents no objective morphological neither spectral changes between both energy ranges under the availabvle statistics and angular resolution. The apparent increase in brightness of the SE spot must be due to the difference in angular resolution and signal-to-noinse ratio between both energy ranges.

6.4 Discussion

The luminosity of W51C in the energy range 0.25 GeV – 5.0 TeV, which is roughly the energy range of the *Fermi* and MAGIC data, is $L_\gamma \approx 1 \times 10^{36} (d/5.5\,{\rm kpc})^2\,{\rm erg\,s}^{-1}$, which is one of the highest among gamma-ray emitting SNRs. This estimates matches the estimated rotational energy loss rate of the PWN, $\dot{E} = 1.5 \times 10^{36}\,{\rm erg\,s}^{-1}$ (Koo et al., 2005). As a consequence, it seems unlikely that the PWN alone is the source of all gamma-ray emission, since it would require an extremely high efficiency in the conversion from rotational energy into gamma rays. As showed in section 6.3.4, the *PWN* region can account for the 20% of the gamma-ray emission confined in a point-like source. However the brightest part is the *cloud* region. Therefore, we considered justified to adopt the approach of a one-zone model for the total gamma-ray emission, dominated by the particles emitting gamma rays in the *cloud* region. The contribution of an additional particle population related to the PWN, if any, shall be considered as an error in the flux normalization of about 20%. This error is within statistical and systematic uncertainties of the MAGIC measurement.

6.4.1 Model description

We modeled the SNR as a sphere homogeneously filled with hydrogen, helium and electrons, with respective average number densities $n_{\rm H}$, $n_{\rm He}$ and n_{e^-}. We assumed the cosmic abundance ratio of helium $n_{\rm He} = 0.1\,n_{\rm H}$. The electron ratio was assumed under the hypothesis of full ionization of the medium, such that $n_{e^-} = 1.2\,n_{\rm H}$. Koo et al. (2010) derived an upper limit for the magnetic field of $B_\parallel < 150\ \mu$G, but Brogan et al. (2000) measured a local magnetic field as high as 1.5–1.9 mG towards the maser sites. In our case, the magnetic field B was assumed to be homogeneous inside the sphere.

The gamma-ray morphology does not follow the $\sim 30'$ partial radio shell (Moon and Koo, 1994) neither the center-filling thermal X-ray emission (Koo et al., 1995). Instead, the maximum of the gamma-ray emission is located at the interaction region of remnant and the molecular cloud, which means that the size of the remnant is not physically related to the size of the VHE emission region. We adopted the intrisnic extension determined in section 6.3.1 to determine the radius of a spherical emission zone. Assuming a distance to W51C of 5.5 kpc (Sato et al., 2010; Moisés et al., 2011), the radius of the sphere was estimated to be 24 pc. This sphere is partially embedded in a molecular cloud of $m_{\rm cloud} = 1.9 \times 10^5\,{\rm M}_\odot$ (Carpenter and Sanders, 1998).

The multi-wavelength data considered in the fit to the spectral energy distribution included radio continuum measurements (Moon and Koo, 1994), high-energy observations with *Fermi*/LAT (Abdo et al., 2009*a*) and VHE observations by MAGIC shown in section 6.3.2. The radio measurements in Moon and Koo (1994) indicate a spectral index

of $\alpha_r \approx -0.26$ (as defined by $S_\nu \propto \nu^{\alpha_r}$). This can be attributed to electrons emitting synchrotron radiation and fixes the initial power-law index of the electron spectrum to $s \approx 1.5$. We adopted this value for both electrons and protons. In absence of measurements of the synchrotron peak in X-rays, we considered the integrated thermal X-ray flux of the whole remnant as measured by *ROSAT* (Koo et al., 1995) as an upper limit to the non-thermal X-ray emission (after converting it into a differential flux in the sub-keV range).

The modeling was performed by folding an input spectra of accelerated particles with cross sections of processes yielding photons; this includes synchrotron radiation, inverse Compton scattering (IC), non-thermal bremsstrahlung and π^0 decay (Blumenthal and Gould, 1970; Baring et al., 1999; Kelner et al., 2006). For IC, we considered three seed photon fields: the cosmic microwave background ($kT_{\rm CMB} = 2.3 \times 10^{-4}$ eV, $u_{\rm CMB} = 0.26\,{\rm eV\,cm^{-3}}$), infrared ($kT_{\rm IR} = 3 \times 10^{-3}\,{\rm eV}, u_{\rm IR} = 0.90\,{\rm eV\,cm^{-3}}$) and optical ($kT_{\rm OPT} = 0.25\,{\rm eV}, u_{\rm OPT} = 0.84\,{\rm eV\,cm^{-3}}$), with temperatures and energy densities for the infrared and optical components adopted from Abdo et al. (2009*a*). Bremsstrahlung was computed on a target of electrons and ions. For the π^0 production cross section, we used the parametrization of Kelner & Aharonian (2006) with a constant nuclear enhancement factor of 1.85 (Mori, 2009). We considered separate scenarios in which each emission process dominates over the others. The models discussed here were obtained using as equilibrium particle spectra a broken power law with an exponential cut-off, both for electrons and protons, of the form:

$$\frac{dN_{e,p}}{dE_{e,p}} = K_{e,p} \left(\frac{E_{e,p}}{E_0}\right)^{-s} \left[1 + \left(\frac{E_{e,p}}{E_{\rm br}}\right)^{\Delta s}\right]^{-1} \exp\left[-\left(\frac{E_{e,p}}{E_{{\rm cut},e,p}}\right)\right] \tag{6.2}$$

The spectral index of each particle population changes from s to $s + \Delta s$ at a break energy $E_{\rm br}$ smoothly. A spectral break in the particle spectrum at these energies had been traditionally thought to be inconsistent with both standard and non-linear diffusive shock acceleration theory (Malkov and O'C Drury, 2001). However, Malkov et al. (2011, 2012*a*) proposed a mechanism which can also explain a spectral break in the cosmic ray spectrum of $\Delta s = 1$ caused by strong ion-neutral collisions in the surroundings of a SNR, which leads to a weakening in the confinement of the accelerated particles. Note also that other authors have proposed scenarios in which the CR spectrum, and consequently the gamma-ray spectrum, can show one or more spectral breaks. For example, due to finite-size acceleration or emission region (Ohira et al., 2011) or energy dependent diffusion of run-away CRs from the remnant (Gabici et al., 2009; Aharonian and Atoyan, 1996). On the other hand, the exponential cut-off at $E_{{\rm cut},e,p}$ reflects the roll-off of the particle spectrum near the maximum energy, arising from the acceleration and confinement mechanism, as well as energy losses.

6.4.2 Adjustment of model parameters

We first considered the case where the emission is dominated by leptonic emission mechanisms. We found the same problems already reported by Abdo et al. (2009*a*), namely that the radio and gamma-ray data cannot be fitted simultaneously. Furthermore these models needed an unusually high electron to proton ratio of the order of 1. When we modeled the emission with pion decay as the dominant process, the parameters resulting from the model adjustment (table 6.2) matched those of the interstellar medium around W51, and both radio and gamma-ray emission were reasonably reproduced (figure 6.9).

Table 6.2: Parameters used in the modeling of the multi-wavelength spectral energy distribution of W51C for the hadronic scenario. The power-law index before the break is $s = 1.5$ for both protons and electrons. $E_0 = 10$ GeV. The total kinetic energy of the particles was integrated for $E_{\rm kin} > 100$ MeV both for electrons and protons.

Parameter	Value
K_e/K_p	1/80
Δs	1.2
$E_{\rm br}$ [GeV]	10
$E_{{\rm cut},e}$ [TeV]	0.1
$E_{{\rm cut},p}$ [TeV]	120
B [μG]	53
n [cm^{-3}]	10.0
W_e [10^{50} erg]	0.069
W_p [10^{50} erg]	5.8

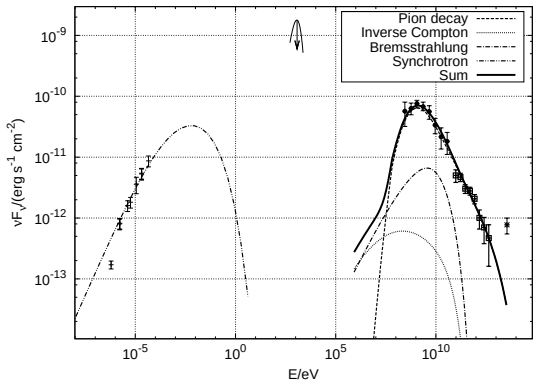

Figure 6.9: Broadband view of the model. The dashes with error bars are 21 cm radio continuum, circles represent *Fermi*/LAT data, squares are the data obtained with the MAGIC telescopes and the star represent the MILAGRO data point. The upper limit in the X-ray regime was obtained from *ROSAT* data as discussed in the text.

Note that the lowest energy radio data point may be affected by free-free absorption (Copetti and Schmidt, 1991), which we did not consider. However, this single point did not affect the fitting of the radio data. One data point by MILAGRO (Abdo et al., 2009*b*) is also shown at an energy of 35 TeV. The MILAGRO measurement has a significance of 3.4 σ, and was derived assuming a gamma-spectrum $\propto E^{-2.6}$ without a cut-off.

The break energy $E_{\rm br}$ was fixed from the *Fermi*/LAT data, while the MAGIC data allowed us to better determine the spectral steepening after the break, $\Delta s = 1.2$ (and, as a consequence, the underlying particle distribution). This value is not far off the prediction from Malkov et al. (2012*a*), giving a hint that this mechanism might be responsible for the observed break. The index we obtained is harder than 1.4, as suggested in Abdo et al. (2009*a*). In order to fit MAGIC data, the cutoff energy must be at energies of at least $E_{{\rm cut},p} \geq 100$ TeV. The precise cut-off energy of the electron spectrum $E_{{\rm cut},e}$ was not well constrained, since the synchrotron peak is not resolved. Therefore, the energy $E_{{\rm cut},e}$ is only a lower limit, as enforced with the radio data. A detailed view of the high energy and VHE region is shown in figure 6.10.

The volume-averaged hydrogen density was obtained as a parameter of the fit. From

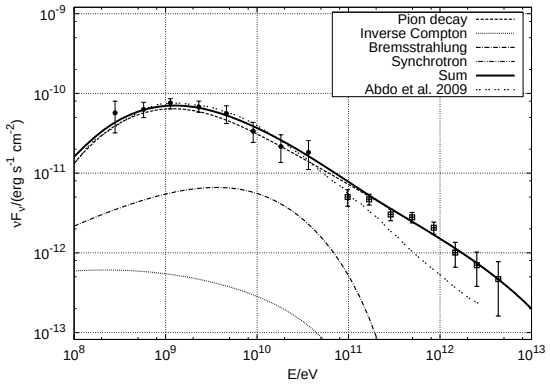

Figure 6.10: Detailed view of the hadronic model in the high energy and VHE region. The hadronic model by Abdo et al. (2009*a*) is shown as double dotted line for comparison.

that, we computed the volume filling factor f, i.e. the fraction of the mass of the molecular cloud that is contained inside the SNR interaction volume (defined as volume of the emission zone) as $f = n_{\rm H} V \left(m_{\rm H}^{\rm atom} + 0.1 m_{\rm He}^{\rm atom}\right) / m_{\rm cloud} \approx 0.11$. This implies that around 11% of the mass of the molecular cloud is contained in the emission volume and is interacting with the SNR. This value is consistent with the filling factors of around 8–20 % for other SNRs interacting with molecular clouds, obtained by other authors (Uchiyama et al., 2010).

Provided that the total energy release in the supernova explosion is $E_{\rm SN} = 3.6{\times}10^{51}$erg (Koo et al., 1995), the total amount of kinetic energy in electrons and protons is about 16 % of the explosion energy of the supernova. This fraction is just slightly higher than the value normally assumed, of around 10 %, of the explosion energy converted into CRs to maintain the observed flux of Galactic CRs (Hillas, 2005). The proton to electron ratio is not far from value observed at earth of $K_p/K_e \approx 50$ (Simpson, 1983).

Since the hadronic gamma-ray emission is proportional to the product of the kinetic energy in protons and the density of the medium, this parameters are striclty correlated. Assuming that the complete mass of the molecular cloud acted as target material (f=1), a density of n=100 cm^{-3} would be needed. Therefore the lower limit of the energy in relativistic protons is about 1.6 % of the supernova explosion energy. Such a scenario would need either a higher magnetic field ($B \sim 150$ μG) or a much lower electron to proton ratio ($K_e/K_p \sim 1/800$) to still reproduce the broadband emission. In addition, the morphology presented in figure 6.7 shows that only a fraction of the molecular cloud is emitting VHE gamma emission. Therefore, we conclude that the amount of kinetic energy in protons is clearly above this lower limit and in the order of 10–20%.

6.4.3 Consequences of the modeling

In the scenario we investigated all the gamma-ray emission was attributed to explained in terms of hadronic interactions of high-energy protons with the molecular cloud and subsequent decay of neutral pions. It was not possible to model the broadband emission with a purely leptonic scenario. However, that could also point to problems in the modeling, especially to oversimplifications concerning the homogeneity of the medium and of the magnetic field. Under these circumstances, it was not possible to decide what process causes the hint of emission observed by MILAGRO which, if confirmed at this flux level,

would require the introduction of an additional component at the highest energies.

As mentioned in section 2.3.3, there are two non-exclusive scenarios which yeld gamma rays from neutral pion decay. These are: cloud illumination by runaway CRs and acceleration of CRs in the shock wave propagating through the cloud. In the first case, an average, isotropic Galactic CR diffusion coefficient at 10 TeV of the order of $\sim 3 \times 10^{29} \mathrm{cm}^2\mathrm{s}^{-1}$ is to be assumed (Gabici et al., 2010). Being the W51 complex at a distance of 5.5 kpc, a sphere of radius $\sim$ 350 pc would be filled with 10 TeV protons, responsible of 1 TeV gamma rays (assuming that the high-energy particles escape the SNR early enough such that the diffusion time can be approximated to be the age of the SNR). The distance between the maximum of the emission measured by MAGIC above 1 TeV and the assumed center of the SNR (RA=19.384 h, DEC=14.11°) is about 8 pc. The distance to other parts of the SNR/cloud complex W51C/B is of similar order. This implies that the complete cloud should be uniformly illuminated by CRs. As can be seen in figure 6.7, we do not detect the complete W51B/C complex at energies above 1 TeV: parts of the outer regions, both on the side towards the SNR and on the northernmost side, do not emit gamma rays. Therefore, a scenario of runaway CRs cannot explain the incomplete illumination of W51B/C, especially towards the outer regions.

Concerning the acceleration of CRs in the shocked cloud scenario, the gamma radiation should be originated very close to the acceleration site of the radiating particles due to the high density of the surrounding medium. This is in agreement with the morphology described in this work. The unusually high ionization reported by Ceccarelli et al. (2011) close to the maximum VHE emission region indicates the presence of freshly accelerated low-energy protons. The missing emission towards the edges of the cloud could be explained with a lower diffusion coefficient in the shocked cloud region, or with a shielding effect, either of which is possible in a surrounding medium of high density. This suggests that the particle distribution, whose gamma emission we observe, may represent the source spectrum of cosmic rays currently being produced in W51C.

6.5 Summary

MAGIC performed a deep observation of a complex Galactic field containing the star-forming regions W51A and W51B, the SNR W51C and the possible PWN CXO J192318.5+140305. As a result of this observation, emission of gamma rays above 150 GeV was detected with 11 σ statistical significance. The low energy threshold of MAGIC allowed us to almost connect the spectrum to the highest energy *Fermi*/LAT points (Abdo et al., 2009*a*). We measured a power law with a photon index of 2.6 between 75 GeV and 4 TeV, which is compatible with what *Fermi*/LAT had measured between 2 and 40 GeV. The spectrum measured by MAGIC precisely determined the spectral slope of the underlying particle distribution above the spectral break measured at around a few GeV by *Fermi*/LAT.

The MAGIC source spatially coincides with those previously reported by H.E.S.S. and *Fermi*/LAT. We were able to restrict the emission region to the zone where W51C interacts with W51B and, in particular, to the region where shocked gas is observed. This clearly pinpoints the origin of the emission to the interaction between the remnant and the molecular cloud. Non-thermal X-ray emission which could help to trace the relativistic electron distribution was found only from a compact region around the position of the possible PWN CXOJ192318.5+140305 (Koo et al., 2005). Morecover, MAGIC saw a local enhancement of the gamma-ray emission around this object. The projection of the gamma-like events on the line connecting the putative PWN and the centroid of the

shocked clouds was better described by the sum of two Gaussian functions. However, the existence of two independent, resolved sources could not be statistically established. We thus investigated the contribution to the total excess of two regions of 0.1°radius centered on the *cloud* region and the *PWN* region. We fond that they contributed about 30% and 20% of the total emission, respectively, and the contribution was not energy dependent within the uncertainties. Spectra of the individual regions above 350 GeV were obtained, but did not allow for detailed conclusions due to the weak individual fluxes. Given the small possible contribution of the PWN candidate in the energies investigated in this work, it is very unlikely that the main conclusion drawn here will be significantly affected even if the PWN contribution can be established.

We produced a physically plausible model of the emission of the SNR by considering a spherical geometry and uniform distribution of the ambient material. We note that this system is clearly anisotropic (as seen in the multi-wavelength data), and more detailed modeling may achieve a better description of the source. We found that the VHE emission from W51C could not be explained by any of the considered leptonic models. The emission was best described when neutral pion decay is the dominant gamma-ray production mechanism. In the proposed model, the SNR has converted about 16% of the explosion energy into kinetic energy for proton acceleration, and the emission zone engulfs a 11% of a molecular cloud of 10^5 solar masses, which provides the target material. In this scenario, protons are required to reach at least an energy of the order of 100 TeV to produce the observed emission. Extension of the spectrum towards higher energies would constrain the maximum achievable energy in the system and might shed light on the meaning of the MILAGRO measurement, which could not be accommodated in the theoretical framework we proposed. The morphology of the source could not be explained by CRs diffusing from the SNR to the cloud. Instead, it could be qualitatively explained with VHE gamma-ray emission being produced at the acceleration site of CRs. This involves ongoing acceleration of CRs or re-acceleration of already existing CRs at the shocked cloud region.

Chapter 7

Conclusions

Supernova remnants, as major contributors to the galactic cosmic rays, are believed to maintain an average cosmic-ray flux by diffusive shock acceleration regardless the way they release cosmic rays into the interstellar medium. Evidence of cosmic-ray acceleration from a supernova remnants is often found due to molecular clouds that glow in gamma-rays due to proton-proton collisions produced within them. However, the interaction of the cosmic rays with nearby gas clouds depends crucially on the release mechanism. In particular, brightness of these systems depends on the cosmic-ray leakage rate from the source, and also how far cosmic rays (either nuclei or electrons) can diffuse away from the source.

In this work we have found signs of spectral variations accross GeV-emitting supernova remnants. We have proposed that this changes may be related to different distances (or stages of the interaction) of the supernova blast wave with adjacent clouds. In two particular cases (cloud A in HB 21 and Scoville's clouds in the Cygnus Loop), the cloud is not overrun by the blast wave, but separated several parsecs from it. The general trend that we find is that the closer the clouds are (i.e. the earlier the interaction took place), the brightest they are in gamma rays, and the softer their spectrum is.

Spectral variations across the object are not resolved in the GeV emission from W51C (Abdo et al., 2009*a*). We note that this object is older than HB 21 or the Cygnus Loop. As seen by MAGIC, W51C is in general dark in gamma rays, except for an extremely bright emission region in the interaction zone with W51B. We interpret this fact in terms of the cosmic-ray escape mechanism proposed by Malkov et al. (2012*b*): W51C has been a powerful cosmic-ray accelerator, with strong self-confinement, until it has vanished. At this point the supernova remnant shell is no longer visible, but large ammount of cosmic rays have been let free and are now interacting with dense material in the adjacent star-forming regions. We cannot exclude that this gamma-ray emission is contributed up to a certain point by the possible pulsar wind nebula CXO J192318.5+140305. The existence of compact sources that could be pulsar wind nebulae associated to supernova remnats introduce some ambiguity regarding the origin of the observed gamma-ray emission. However, within a margin of a 20% in luminosity, W51C is the brightest supernova remnant detected so far in gamma rays.

The observed supernova remnants confirm the existence of spectral breaks. These breaks are unexpected under the assumption of a featureless power-law distribution of accelerated protons producing the gamma-ray emission. (Malkov et al., 2011) suggested that the spectral break in the gamma-ray emission from W44 (Abdo et al., 2010*d*) may be related to the interaction of accelerated protons with a partially ionized gas, that deteriorates the confinement, and steepens the gamma-ray spectrum by exactly one power.

In W44, W51C (Abdo et al., 2009*a*) and other GeV-bright supernova remnants, the spectral break occurs at 1-2 GeV. This corresponds to a break in the proton momentum at (Malkov et al., 2011):

$$p_{br}/mc \approx 10 B_{\mu}^{2} T_{4}^{-0.4} n_{0}^{-1} n_{i}^{-1/2}, \tag{7.1}$$

where the magnetic field, B, is expressed in micro Gauss, the temperature T is in units of 10^4 K. The neutral particle density, n_0, and the ion density, n_i, are in cm^{-3}. Should the break depend on the density like in equation 7.1, then the energy breaks at 0.4-0.7 GeV observed in HB 21 and the Cygnus Loop implies (under the assumption of a similar magnetic field) a higher ambient density. We have no notice of ionized material around these two objects. This fact could be compensated by a higher density n_0, which is possibly the case in HB 21, but seems unlikely in the Cygnus Loop.

The fact that the first supernova remnants to be detected in gamma rays, like W51C or W44, are so bright does not mean that they are a representative population of the Galactic supernova remnants. After the observations of low-luminosity, nearby supernova remnants like HB 21 or the Cygnus Loop, we note that such objects would not be detected with the present instruments at distances of several kpc. Therefore, we confirm the existence of a population of low-luminosity gamma-ray emittig supernova remnants. We consider this evidence important regarding the contribution to the cosmic rays detected on Earth, as the source density could be higher than expected. However, we note that these objects most probably do not reach maximum proton energies close to the knee. Among all supernova remnants, ultra-high energies seem to be reserved for exceptional objects whose environment, or perhaps its precursor intrinsic properties, favor the efficient acceleration of nuclei during long enough periods.

The selection of candidates we performed yielded great fraction of detections i the *Fermi*/LAT energy band, and the extension of this approach to southern objects should be considered. In the MAGIC energy band, supernova remnants are intrinsically dimmer in terms of energy flux, and only particularly bright, hard objects seem to be within reach at the current sensitivity. We look forward for the advent of the Cherenkov Telescope Array, which will certainly populate the list of supernova remnants detected at very high energies, and will certainly address the question of the maximum energy reachable by these objects.

Acknowledgments

Elaborar aquesta tesi ha implicat uns alt i baixos d'una amplitud que no m'imaginava que pogués experimentar. Com va dir un bon amic en el moment de llegir la seva tesi, la muntanya russa més boja a la que mai hagi pujat. Igual que per l'alpinista l'atracció dels cims és irressitible, un cop a dalt un s'adona que allà no podria sobreviure, i que el seu lloc és a baix, a la vall.

I would like to thank the staff MAGIC group at IFAE, Juan Cortina, Javier Rico, Abelardo Moralejo, Oscar Blanch, and Manel Martínez, for giving me the possibility to work with them for almost five years. I don not want to forget any of my colleagues with whom I shared this time at IFAE: Núria Sidro, Daniel Mazin, Stefan Klepser, Victor Stamatescu, Julian Sitarek. In particular, Roger Firpo helped a lot at the beginning of my research. Students like Manel Errando, Diego Tescaro, Roberta Zanin, Alicia López, Jelena Aleksić, Adiv González, Elsa de Cea, Dani Garrido, Gianluca Giavitto, Rubén López and Daniela Hadasch, in addition to work colleagues became good friends with whom we shared countless moments of fun, and also some stress. There were other colleagues, like Carlos Osuna and Germano Nardini, who were not really interested in astrophysics, but nevertheless we shared spectacular adventures, some of them at great altitudes above the sea level.

It can be said that the research I presented in this report would not have been possible if my supervisor, Javier Rico, and my co-supervisor, Emma de Oña, would have agreed to go for a joint research project that allowed me to perform a series of stages at Max Plank institute for Nuclear Physics (MPI-K), in Heidelberg[1]. In these stages I had the opportunity to work close to very prestigious scientists like Felix Aharonian, Maxim Barkov, Roland Crocker or Frank Rieger. In Heidelberg I met old friends like Víctor Zabalza and David López, and also new collaborators, like Rui-Zhi Yang. At MPI-K had a healthy tradition to play some kicker matches after lunch, and Eva Lefa, Dave Jones and Ervin Kafexhiu did not miss any of those.

Within the MAGIC collaboration I was accompanied by many other persons in addition of those mentioned above. I would like to mention Marc Ribó, Emiliano Carmona and Julian Krause, with whom I shared a lot of hours on Skype and also hundreds of mails. Also with David Paneque, Rebecca Gozzini, and Marcos López, we had a good time on the telescope site.

Tanmateix les persones que veritablement han fet possible que arribés fins aquí són

[1]This research was funded by projects DE2009-0064 i FPA2009-07474, from Ministerio de Investigación, Desarrollo e Innovación, these projects were managed by Javier Rico and Emma de Oña.

a la meva família. Sense el recolzament dels meus pares i les meve àvies aquesta tesi no hagués estat possible. També les meves ties i oncles s'han vist implicades en algun moment o altre. A vosaltres també, gràcies.

Mereix una menció especial la meva xicota, l'Ariadna, amb la que he conviscut tot aquest temps i que ha hagut d'aguantar els meus canvis d'humor. Moltes gràcies també als seus pares pel seu suport.

Finalment no m'oblido de dues persones que van veure com comen cava la tesi, però no han arribat a veure com l'acabava. El vostre record és el que m'ha empès en els moments més durs.

Bibliography

Abbasi R., Abdou Y., Abu-Zayyad T. et al. (2012). *Observation of Anisotropy in the Galactic Cosmic-Ray Arrival Directions at 400 TeV with IceCube.* ApJ **746** 33. 1109.1017.

Abdo A.A., Ackermann M., Ajello M. et al. (2009*a*). *Fermi LAT Discovery of Extended Gamma-Ray Emission in the Direction of Supernova Remnant W51C.* ApJ **706** L1–L6. 0910.0908.

Abdo A.A., Ackermann M., Ajello M. et al. (2010*a*). *Fermi Large Area Telescope First Source Catalog.* ApJS **188** 405–436. 1002.2280.

Abdo A.A., Ackermann M., Ajello M. et al. (2010*b*). *Fermi-Lat Discovery of GeV Gamma-Ray Emission from the Young Supernova Remnant Cassiopeia A.* ApJ **710** L92–L97. 1001.1419.

Abdo A.A., Ackermann M., Ajello M. et al. (2010*c*). *Fermi-LAT Study of Gamma-ray Emission in the Direction of Supernova Remnant W49B.* ApJ **722** 1303–1311.

Abdo A.A., Ackermann M., Ajello M. et al. (2010*d*). *Gamma-Ray Emission from the Shell of Supernova Remnant W44 Revealed by the Fermi LAT.* Science **327** 1103–.

Abdo A.A., Ackermann M., Ajello M. et al. (2010*e*). *Observation of Supernova Remnant IC 443 with the Fermi Large Area Telescope.* ApJ **712** 459–468. 1002.2198.

Abdo A.A., Allen B., Aune T. et al. (2008). *Discovery of Localized Regions of Excess 10-TeV Cosmic Rays.* Physical Review Letters **101** 221101. 0801.3827.

Abdo A.A., Allen B.T., Aune T. et al. (2009*b*). *Milagro Observations of Multi-TeV Emission from Galactic Sources in the Fermi Bright Source List.* ApJ **700** L127–L131. 0904.1018.

Ackermann M., Ajello M., Allafort A. et al. (2012). *Measurement of Separate Cosmic-Ray Electron and Positron Spectra with the Fermi Large Area Telescope.* Physical Review Letters **108** 011103. 1109.0521.

Ackermann M., Ajello M., Atwood W.B. et al. (2010). *Fermi LAT observations of cosmic-ray electrons from 7 GeV to 1 TeV.* Phys. Rev. D **82** 092004. 1008.3999.

Adriani O., Barbarino G.C., Bazilevskaya G.A. et al. (2010). *A statistical procedure for the identification of positrons in the PAMELA experiment.* Astroparticle Physics **34** 1–11. 1001.3522.

Aharonian F., Akhperjanian A.G., Anton G. et al. (2009). *Probing the ATIC peak in the cosmic-ray electron spectrum with H.E.S.S.* A&A **508** 561–564. 0905.0105.

Aharonian F., Akhperjanian A.G., Bazer-Bachi A.R. et al. (2008). *Discovery of very high energy gamma-ray emission coincident with molecular clouds in the W 28 (G6.4-0.1) field.* A&A **481** 401–410. 0801.3555.

Aharonian F.A. (1991). *Very high and ultra-high-energy gamma-rays from giant molecular clouds.* Ap&SS **180** 305–320.

Aharonian F.A. (2004). *Very high energy cosmic gamma radiation : a crucial window on the extreme Universe.* World Scientific.

Aharonian F.A. and Atoyan A.M. (1996). *On the emissivity of π ˆ0 ˆ-decay gamma radiation in the vicinity of accelerators of galactic cosmic rays.* A&A **309** 917–928.

Albert J., Aliu E., Anderhub H. et al. (2007*a*). *Discovery of Very High Energy Gamma Radiation from IC 443 with the MAGIC Telescope.* ApJ **664** L87–L90. 0705.3119.

Albert J., Aliu E., Anderhub H. et al. (2007*b*). *Unfolding of differential energy spectra in the MAGIC experiment.* Nuclear Instruments and Methods in Physics Research A **583** 494–506. 0707.2453.

Albert J., Aliu E., Anderhub H. et al. (2008). *Implementation of the Random Forest Method for the Imaging Atmospheric Cherenkov Telescope MAGIC.* Nucl.Instrum.Meth. **A588** 424–432. 0709.3719.

Aleksić J., Alvarez E.A., Antonelli L.A. et al. (2011). *Performance of the MAGIC stereo system obtained with Crab Nebula data.* ArXiv e-prints 1108.1477.

Aleksić J., Alvarez E.A., Antonelli L.A. et al. (2012). *Morphological and spectral properties of the W51 region measured with the MAGIC telescopes.* A&A **541** A13. 1201.4074.

Aliu E., Anderhub H., Antonelli L.A. et al. (2009). *Improving the performance of the single-dish Cherenkov telescope MAGIC through the use of signal timing.* Astroparticle Physics **30** 293–305. 0810.3568.

Amenomori M., Ayabe S., Bi X.J. et al. (2006). *Anisotropy and Corotation of Galactic Cosmic Rays.* Science **314** 439–443. arXiv:astro-ph/0610671.

Atwood W.B., Bagagli R., Baldini L. et al. (2007). *Design and initial tests of the Tracker-converter of the Gamma-ray Large Area Space Telescope.* Astroparticle Physics **28** 422–434.

Baade W. and Zwicky F. (1934*a*). *Cosmic Rays from Super-novae.* Proceedings of the National Academy of Science **20** 259–263.

Baade W. and Zwicky F. (1934*b*). *On Super-novae.* Proceedings of the National Academy of Science **20** 254–259.

Ballet J. (2006). *X-ray synchrotron emission from supernova remnants.* Advances in Space Research **37** 1902–1908. arXiv:astro-ph/0503309.

Bamba A., Yamazaki R., Ueno M. et al. (2004). *Fine structure of the thermal and non-thermal X-rays in the SN 1006 shell*. Advances in Space Research **33** 376–380. arXiv:astro-ph/0308322.

Baring M.G., Ellison D.C., Reynolds S.P. et al. (1999). *Radio to Gamma-Ray Emission from Shell-Type Supernova Remnants: Predictions from Nonlinear Shock Acceleration Models*. ApJ **513** 311–338. arXiv:astro-ph/9810158.

Beichman C.A., Neugebauer G., Habing H.J. et al., editors (1988). *Infrared astronomical satellite (IRAS) catalogs and atlases. Volume 1: Explanatory supplement*, vol. 1.

Bell A.R. (2004). *Turbulent amplification of magnetic field and diffusive shock acceleration of cosmic rays*. MNRAS **353** 550–558.

Bertero M. (1989). *Linear inverse and iii-posed problems*. vol. 75 of *Advances in Electronics and Electron Physics*, 1 – 120. Academic Press. URL http://www.sciencedirect.com/science/article/pii/S0065253908609464.

Bing Jiang (2011). *A List of Galactic SNRs Interacting with Molecular Clouds*. URL http://astronomy.nju.edu.cn/~ygchen/others/bjiang/interSNR6.htm.

Blair W.P., Sankrit R. and Raymond J.C. (2005). *Hubble Space Telescope Imaging of the Primary Shock Front in the Cygnus Loop Supernova Remnant*. AJ **129** 2268–2280.

Blandford R.D. and Cowie L.L. (1982). *Radio emission from supernova remnants in a cloudy interstellar medium*. ApJ **260** 625–634.

Blumenthal G.R. and Gould R.J. (1970). *Bremsstrahlung, Synchrotron Radiation, and Compton Scattering of High-Energy Electrons Traversing Dilute Gases*. Reviews of Modern Physics **42** 237–271.

Borla Tridon D., Goebel F., Fink D. et al. (2009). *Performance of the Camera of the MAGIC II Telescope*. ArXiv e-prints 0906.5448.

Bretz T., Dorner D., Wagner R.M. et al. (2009). *The drive system of the major atmospheric gamma-ray imaging Cherenkov telescope*. Astroparticle Physics **31** 92–101. 0810.4593.

Brogan C.L., Frail D.A., Goss W.M. et al. (2000). *OH Zeeman Magnetic Field Detections toward Five Supernova Remnants Using the VLA*. ApJ **537** 875–890. arXiv:astro-ph/0002398.

Byun D.Y., Koo B.C., Tatematsu K. et al. (2006). *Interaction between the Supernova Remnant HB 21 and Molecular Clouds*. ApJ **637** 283–295.

Carpenter J.M. and Sanders D.B. (1998). *The W51 Giant Molecular Cloud*. AJ **116** 1856–1867. arXiv:astro-ph/9806298.

Castro D., Slane P., Ellison D.C. et al. (2012). *Fermi-LAT Observations and a Broadband Study of Supernova Remnant CTB 109*. ApJ **756** 88. 1207.1432.

Ceccarelli C., Hily-Blant P., Montmerle T. et al. (2011). *Supernova-enhanced Cosmic-Ray Ionization and Induced Chemistry in a Molecular Cloud of W51C*. ApJ **740** L4+. 1108.3600.

Condon J.J., Broderick J.J., Seielstad G.A. et al. (1994). *A 4.85 GHz sky survey. 3: Epoch 1986 and combined (1986+1987) maps covering 0 deg less than delta less than +75 deg.* AJ **107** 1829–1833.

Copetti M.V.F. and Schmidt A.A. (1991). *Aperture synthesis observations of W 51 at 151 MHz.* MNRAS **250** 127–132.

Dame T.M., Hartmann D. and Thaddeus P. (2001). *The milky way in molecular clouds: A new complete co survey.* The Astrophysical Journal **547** 792. URL `http://stacks.iop.org/0004-637X/547/i=2/a=792`.

Dame T.M., Ungerechts H., Cohen R.S. et al. (1987). *A composite CO survey of the entire Milky Way.* ApJ **322** 706–720.

Di Sciascio G., Iuppa R. and Argo-Ybj Collaboration (2012). *Observation of CR Anisotropy with ARGO-YBJ.* Journal of Physics Conference Series **375** 052008. `1112.0666`.

Doro M., Bastieri D., Biland A. et al. (2008). *The reflective surface of the MAGIC telescope.* Nuclear Instruments and Methods in Physics Research A **595** 200–203.

Estalella R. and Anglada G. (2008). *Introducció a la física del medi interestel·lar.* Universitat de Barcelona.

Fermi E. (1949). *On the Origin of the Cosmic Radiation.* Physical Review **75** 1169–1174.

Fermi-LAT Collaboration (2012). *The Fermi Large Area Telescope On Orbit: Event Classification, Instrument Response Functions, and Calibration.* ArXiv e-prints `1206.1896`.

Ferrand G. and Safi-Harb S. (2012). *A census of high-energy observations of Galactic supernova remnants.* Advances in Space Research **49** 1313–1319. `1202.0245`.

Ferrand, G. and Marcowith, A. (2010). *On the shape of the spectrum of cosmic rays accelerated inside superbubbles.* A&A **510** A101. URL `http://dx.doi.org/10.1051/0004-6361/200913520`.

Fiasson A., Marandon V., Chaves R.C.G. et al. (2009). *Discovery of a VHE gamma-ray source in the W51 region.* In *Proceedings of the 31st ICRC, Lodz.*

Firpo R., Delfino M., Neisser C. et al. (2011). *The MAGIC data processing pipeline.* J.Phys.Conf.Ser. **331** 032040.

Fomin V.P., Stepanian A.A., Lamb R.C. et al. (1994). *New methods of atmospheric Cherenkov imaging for gamma-ray astronomy. I. The false source method.* Astroparticle Physics **2** 137–150.

Frail D.A., Goss W.M., Reynoso E.M. et al. (1996). *A Survey for OH (1720 MHz) Maser Emission Toward Supernova Remnants.* AJ **111** 1651.

Gabici S. (2012). *Cosmic rays and molecular clouds.* ArXiv e-prints `1208.4979`.

Gabici S., Aharonian F.A. and Casanova S. (2009). *Broad-band non-thermal emission from molecular clouds illuminated by cosmic rays from nearby supernova remnants.* MNRAS **396** 1629–1639. `0901.4549`.

Gabici S., Casanova S., Aharonian F.A. et al. (2010). *Constraints on the cosmic ray diffusion coefficient in the W28 region from gamma-ray observations.* In S. Boissier, M. Heydari-Malayeri, R. Samadi, & D. Valls-Gabaud , editor, *SF2A-2010: Proceedings of the Annual meeting of the French Society of Astronomy and Astrophysics*, 313–+. 1009.5291.

Gaisser T.K., Protheroe R.J. and Stanev T. (1998). *Gamma-Ray Production in Supernova Remnants.* ApJ **492** 219. arXiv:astro-ph/9609044.

Ginzburg V.L. and Syrovatskii S.I. (1964). *The Origin of Cosmic Rays.*

Goebel F., Bartko H., Carmona E. et al. (2007). *Upgrade of the MAGIC Telescope with a Multiplexed Fiber-Optic 2 GSamples/s FADC Data Acquisition system.* ArXiv e-prints 0709.2363.

Graham J.R., Levenson N.A., Hester J.J. et al. (1995). *An X-ray and optical study of the interaction of the Cygnus Loop supernova remnant with an interstellar cloud.* ApJ **444** 787–795.

Green A.J., Frail D.A., Goss W.M. et al. (1997). *Continuation of a survey of OH (1720 MHz) Maser Emission Towards Supernova Remnants.* AJ **114** 2058–+.

Green D.A. (2009). *A revised Galactic supernova remnant catalogue.* Bulletin of the Astronomical Society of India **37** 45–61. 0905.3699.

Green D.A. (2012). *The distribution of SNRs with Galactocentric radius.* ArXiv e-prints 1208.3107.

Greisen K. (1966). *End to the Cosmic-Ray Spectrum?* Physical Review Letters **16** 748–750.

Haakonsen C.B. and Rutledge R.E. (2009). *XID II: Statistical Cross-Association of ROSAT Bright Source Catalog X-ray Sources with 2MASS Point Source Catalog Near-Infrared Sources.* ApJS **184** 138–151. 0910.3229.

Hanlon W.F. (2009). *Updated Cosmic Ray Spectrum.* URL http://www.physics.utah.edu/~whanlon/spectrum.html.

Haungs A. (2003). *Energy spectrum and mass composition around the knee by EAS measurements.* Journal of Physics G Nuclear Physics **29** 809–820. arXiv:astro-ph/0212481.

Heck D., Knapp J., Capdevielle J.N. et al. (1998). *CORSIKA: a Monte Carlo code to simulate extensive air showers.*

Hess V.F. (1912). *Über Beobachtungen der durchdringenden Strahlung bei sieben Freiballonfahrten.* Physikalische Zeitschrift **13** 1084–1091.

H.E.S.S. Collaboration (2008). *Differential flux sensitivity.* URL http://www.mpi-hd.mpg.de/hfm/HESS/pages/home/proposals/sc_sens.pdf.

Hillas A.M. (1985). *Cerenkov light images of EAS produced by primary gamma.* In F.C. Jones, editor, *International Cosmic Ray Conference*, vol. 3 of *International Cosmic Ray Conference*, 445–448.

Hillas A.M. (2005). *TOPICAL REVIEW: Can diffusive shock acceleration in supernova remnants account for high-energy galactic cosmic rays?* Journal of Physics G Nuclear Physics **31** 95.

Hillas A.M. (2006). *Cosmic Rays: Recent Progress and some Current Questions.* ArXiv Astrophysics e-prints arXiv:astro-ph/0607109.

Hinton J.A. and Hofmann W. (2009). *Teraelectronvolt Astronomy.* ARA&A **47** 523–565. 1006.5210.

Hollenbach D. and McKee C.F. (1989). *Molecule formation and infrared emission in fast interstellar shocks. III - Results for J shocks in molecular clouds.* ApJ **342** 306–336.

Huang Y.L. and Thaddeus P. (1986). *Molecular clouds and supernova remnants in the outer galaxy.* ApJ **309** 804–821.

Hunter S.D., Bertsch D.L., Catelli J.R. et al. (1997). *EGRET Observations of the Diffuse Gamma-Ray Emission from the Galactic Plane.* ApJ **481** 205.

Hwang U., Decourchelle A., Holt S.S. et al. (2002). *Thermal and Nonthermal X-Ray Emission from the Forward Shock in Tycho's Supernova Remnant.* ApJ **581** 1101–1115. arXiv:astro-ph/0208485.

Katagiri H., Tibaldo L., Ballet J. et al. (2011). *Fermi Large Area Telescope Observations of the Cygnus Loop Supernova Remnant.* ApJ **741** 44. 1108.1833.

Katsuda S., Tsunemi H., Mori K. et al. (2012). *Discovery of a Pulsar Wind Nebula Candidate in the Cygnus Loop.* ApJ **754** L7. 1206.4367.

Katsuta J., Uchiyama Y., Tanaka T. et al. (2012). *Fermi Large Area Telescope Observation of Supernova Remnant S147.* ApJ **752** 135. 1204.4703.

Kelner S.R., Aharonian F.A. and Bugayov V.V. (2006). *Energy spectra of gamma rays, electrons, and neutrinos produced at proton-proton interactions in the very high energy regime.* Phys. Rev. D **74** 034018. arXiv:astro-ph/0606058.

Kohnle A., Aharonian F., Akhperjanian A. et al. (1996). *Stereoscopic imaging of air showers with the first two HEGRA Cherenkov telescopes.* Astroparticle Physics **5** 119–131.

Koo B.C. and Heiles C. (1991). *A survey of H I 21 centimeter emission lines toward supernova remnants.* ApJ **382** 204–222.

Koo B.C., Heiles C., Stanimirović S. et al. (2010). *H I Zeeman Experiments of Shocked Atomic Gas in Two Supernova Remnants Interacting with Molecular Clouds.* AJ **140** 262–265.

Koo B.C., Kim K.T. and Seward F.D. (1995). *ROSAT Observations of the Supernova Remnant W51C.* ApJ **447** 211–+.

Koo B.C., Lee J.J. and Seward F.D. (2002). *An ASCA Study of the W51 Complex.* AJ **123** 1629–1638. arXiv:astro-ph/0112367.

Koo B.C., Lee J.J., Seward F.D. et al. (2005). *Chandra Observations of the W51C Supernova Remnant.* ApJ **633** 946–952.

Koo B.C. and Moon D.S. (1997*a*). *Interaction between the W51C Supernova Remnant and a Molecular Cloud. I. H i 21 Centimeter Line Observations.* ApJ **475** 194–+.

Koo B.C. and Moon D.S. (1997*b*). *Interaction between the W51C Supernova Remnant and a Molecular Cloud. II. Discovery of Shocked CO and HCO +.* ApJ **485** 263–+.

Koo B.C., Rho J., Reach W.T. et al. (2001). *Shocked Molecular Gas in the Supernova Remnant HB 21.* ApJ **552** 175–188. arXiv:astro-ph/0012341.

Koyama K. (2001). *Particle acceleration in the shell of SNRs.* In F.A. Aharonian and H.J. Völk, editors, *American Institute of Physics Conference Series*, vol. 558 of *American Institute of Physics Conference Series*, 82–87.

Lazendic J.S. and Slane P.O. (2006). *Enhanced Abundances in Three Large-Diameter Mixed-Morphology Supernova Remnants.* ApJ **647** 350–366. arXiv:astro-ph/0505498.

Leahy D.A. and Aschenbach B. (1996). *ROSAT X-ray observations of the supernova remnant HB 21.* A&A **315** 260–264.

Lessard R.W., Buckley J.H., Connaughton V. et al. (2001). *A new analysis method for reconstructing the arrival direction of TeV gamma rays using a single imaging atmospheric Cherenkov telescope.* Astroparticle Physics **15** 1–18. arXiv:astro-ph/0005468.

Levenson N.A., Graham J.R., Hester J.J. et al. (1996). *All Quiet on the Western Front? X-Ray and Optical Observations of a Prototypical Cloud–Blast Wave Interaction in the Cygnus Loop.* ApJ **468** 323.

Levenson N.A., Graham J.R., Keller L.D. et al. (1998). *Panoramic Views of the Cygnus Loop.* ApJS **118** 541–561. arXiv:astro-ph/9805008.

Li T.P. and Ma Y.Q. (1983). *Analysis methods for results in gamma-ray astronomy.* ApJ **272** 317–324.

Linke F. (1904). *Luftelektrische Messungen bei zwölf Ballonfahrten.* Abhandlungen der Gesellschaft der Wissenschaften in Göttingen. Mathematisch-Physikalische Klasse **3** 1–90.

Lombardi S. (2011). *Advanced stereoscopic gamma-ray shower analysis with the MAGIC telescopes.* In *International Cosmic Ray Conference*, vol. 3 of *International Cosmic Ray Conference*, 262. 1109.6195.

Longair M.S. (1992). *High energy astrophysics. Vol.1: Particles, photons and their detection.*

MAGIC Collaboration (in preparation). *Upper limits on the very high energy gamma-ray emission of supernova remnants observed with the MAGIC telescopes* .

Majumdar P., Moralejo A., Bigongiari C. et al. (2005). *Monte Carlo simulation for the MAGIC telescope.* In *International Cosmic Ray Conference*, vol. 5 of *International Cosmic Ray Conference*, 203.

Malkov M.A., Diamond P.H. and Sagdeev R.Z. (2011). *Mechanism for spectral break in cosmic ray proton spectrum of supernova remnant W44*. Nature Communications **2**. 1004.4714.

Malkov M.A., Diamond P.H. and Sagdeev R.Z. (2012*a*). *On the mechanism for breaks in the cosmic ray spectrum*. ArXiv e-prints 1206.1384.

Malkov M.A., Diamond P.H., Sagdeev R.Z. et al. (2012*b*). *Analytic Solution for Self-regulated Collective Escape of Cosmic Rays from their Acceleration Sites*. ArXiv e-prints 1207.4728.

Malkov M.A. and O'C Drury L. (2001). *Nonlinear theory of diffusive acceleration of particles by shock waves*. Reports on Progress in Physics **64** 429–481.

Mattox J.R., Bertsch D.L., Chiang J. et al. (1996). *The Likelihood Analysis of EGRET Data*. ApJ **461** 396.

Meegan C., Lichti G., Bhat P.N. et al. (2009). *The Fermi Gamma-ray Burst Monitor*. ApJ **702** 791–804. 0908.0450.

Mirzoyan R. (1997). *On the Calibration Accuracy of Light Sensors in Atmospheric Cherenkov Fluorescence and Neutrino Experiments*. In *International Cosmic Ray Conference*, vol. 7 of *International Cosmic Ray Conference*, 265.

Miyata E., Ohta K., Torii K. et al. (2001). *On the Nature of AX J2049.6+2939/AX J2050.0+2914*. ApJ **550** 1023–1029. arXiv:astro-ph/0011535.

Miyata E. and Tsunemi H. (2001). *Reflection-shocked Gas in the Cygnus Loop Supernova Remnant*. ApJ **552** 624–638. arXiv:astro-ph/0101558.

Moisés A.P., Damineli A., Figuerêdo E. et al. (2011). *Spectrophotometric distances to Galactic H II regions*. MNRAS **411** 705–760. 1009.3924.

Moon D.S. and Koo B.C. (1994). *Thermal and Non-Thermal Radio Continuum Sources in the W51 Complex*. Journal of Korean Astronomical Society **27** 81–102.

Moralejo A., Gaug M., Carmona E. et al. (2009). *MARS, the MAGIC Analysis and Reconstruction Software*. ArXiv e-prints 0907.0943.

Mori M. (2009). *Nuclear enhancement factor in calculation of Galactic diffuse gamma-rays: A new estimate with DPMJET-3*. Astroparticle Physics **31** 341–343. 0903.3260.

Nolan P.L., Abdo A.A., Ackermann M. et al. (2012). *Fermi Large Area Telescope Second Source Catalog*. ApJS **199** 31. 1108.1435.

Ohira Y., Murase K. and Yamazaki R. (2011). *Gamma-rays from molecular clouds illuminated by cosmic rays escaping from interacting supernova remnants*. MNRAS **410** 1577–1582. 1007.4869.

Olinto A.V. (2012). *Cosmic rays at the highest energies*. Journal of Physics Conference Series **375** 052001. 1201.4519.

Pacini D. (1912). *Penetrating radiation at the surface of and in water*. Nuovo Cimento **6** 93–100.

Paneque D. et al. O. (2011). *Fermi Symposium, Sources in the Fermi Sky above 10 GeV.* In *Proceedings of the Fermi Symposium, Rome.*

Paoletti R., Cecchi R., Corti D. et al. (2007). *The Trigger System of the MAGIC Telescope.* IEEE Transactions on Nuclear Science **54** 404–409.

Patnaude D.J., Fesen R.A., Raymond J.C. et al. (2002). *An Isolated, Recently Shocked ISM Cloud in the Cygnus Loop Supernova Remnant.* AJ **124** 2118–2134. arXiv:astro-ph/0206492.

Paturel G., Dubois P., Petit C. et al. (2002). *Comparison LEDA/SIMBAD octobre 2002. Catalogue to be published in 2003.* LEDA, 0 (2002) 0.

Protassov R., van Dyk D.A., Connors A. et al. (2002). *Statistics, Handle with Care: Detecting Multiple Model Components with the Likelihood Ratio Test.* ApJ **571** 545–559. arXiv:astro-ph/0201547.

Rando R.f. (2009). *Post-launch performance of the Fermi Large Area Telescope.* ArXiv e-prints 0907.0626.

Reach W.T., Rho J., Jarrett T.H. et al. (2002). *Molecular and Ionic Shocks in the Supernova Remnant 3C 391.* ApJ **564** 302–316. arXiv:astro-ph/0108173.

Regener E. (1932). *Über das spektrum der ultrastrahlung.* Physikalische Zeitschrift **74** 433–454.

Reich W. (1982). *A radio continuum survey of the northern sky at 1420 MHz. I.* A&AS **48** 219–297.

Reichardt I. (2009). *Massive, automatic data analysis for the MAGIC telescopes.* Master's thesis, Universitat Autònoma de Barcelona. URL http://magic.mppmu.mpg.de/publications/theses/IReichardt.pdf.

Reichardt I., Carmona E., Krause J. et al. (2011). *Probing proton acceleration in W51C with MAGIC* . Mem. Soc. Astron. Italiana **82** 735.

Reichardt I., de Oña Wilhelmi E., Rico J. et al. (2012). *An extended source of GeV gamma rays coincident with the supernova remnant HB 21.* A&A , in press 1207.2057.

Reichardt I., Rico J., Carmona E. et al. (2009). *The MAGIC Data Center.* ArXiv e-prints 0907.0968.

Reville B. and Bell A.R. (2012). *A filamentation instability for streaming cosmic rays.* MNRAS **419** 2433–2440. 1109.5690.

Rissi M., Otte N., Schweizer T. et al. (2009). *A New Sum Trigger to Provide a Lower Energy Threshold for the MAGIC Telescope.* IEEE Transactions on Nuclear Science **56** 3840–3843.

Rolke W.A., López A.M. and Conrad J. (2005). *Limits and confidence intervals in the presence of nuisance parameters.* Nuclear Instruments and Methods in Physics Research A **551** 493–503. arXiv:physics/0403059.

Rosado M., Arias L. and Ambrocio-Cruz P. (2007). *Kinematics of the Molecular Hydrogen Associated with the Supernova Remnant IC 443.* AJ **133** 89–98.

Sato M., Reid M.J., Brunthaler A. et al. (2010). *Trigonometric Parallax of W51 Main/-South.* ApJ **720** 1055–1065. 1006.4218.

Schmelling M. (1994). *The method of reduced cross-entropy A general approach to unfold probability distributions.* Nuclear Instruments and Methods in Physics Research A **340** 400–412.

Schure K.M., Bell A.R., O'C Drury L. et al. (2012). *Diffusive Shock Acceleration and Magnetic Field Amplification.* Space Sci. Rev. 14. 1203.1637.

Scoville N.Z., Irvine W.M., Wannier P.G. et al. (1977). *CO emission from supernova remnants.* ApJ **216** 320.

Seward F.D. and Wang Z.R. (1988). *Pulsars, X-ray synchrotron nebulae, and guest stars.* ApJ **332** 199–205.

Shinn J.H., Lee H.G. and Moon D.S. (2012). *Ortho-to-Para Ratio Studies of Shocked H2 Gas in the Two Supernova Remnants IC 443 and HB 21.* ArXiv e-prints 1209.0265.

Shull J.M. and Beckwith S. (1982). *Interstellar molecular hydrogen.* ARA&A **20** 163–190.

Simpson J.A. (1983). *Elemental and Isotopic Composition of the Galactic Cosmic Rays.* Annual Review of Nuclear and Particle Science **33** 323–382.

Tatematsu K., Fukui Y., Landecker T.L. et al. (1990). *The interaction of the supernova remnant HB 21 with the interstellar medium - CO, H I, and radio continuum observations.* A&A **237** 189–200.

Tescaro D., Aleksic J., Barcelo M. et al. (2009). *The readout system of the MAGIC-II Cherenkov Telescope.* ArXiv e-prints 0907.0466.

Thompson D.J., Bertsch D.L., Fichtel C.E. et al. (1993). *Calibration of the Energetic Gamma-Ray Experiment Telescope (EGRET) for the Compton Gamma-Ray Observatory.* ApJS **86** 629–656.

Tikhonov A. and Arsenin V. (1977). *Solutions of ill-posed problems.* Scripta series in mathematics. Winston.

Uchiyama Y., Blandford R.D., Funk S. et al. (2010). *Gamma-ray Emission from Crushed Clouds in Supernova Remnants.* ApJ **723** L122–L126. 1008.1840.

Uchiyama Y., Funk S., Katagiri H. et al. (2012). *Fermi Large Area Telescope Discovery of GeV Gamma-Ray Emission from the Vicinity of SNR W44.* ApJ **749** L35. 1203.3234.

Uyanıker B., Reich W., Yar A. et al. (2002). *Is the Cygnus Loop two supernova remnants?* A&A **389** L61–L64. arXiv:astro-ph/0205443.

van Weeren R.J., Rttgering H.J.A., Brggen M. et al. (2010). *Particle acceleration on megaparsec scales in a merging galaxy cluster.* Science **330** 347–349. http://www.sciencemag.org/content/330/6002/347.full.pdf, URL http://www.sciencemag.org/content/330/6002/347.abstract.

Völk H.J., Berezhko E.G. and Ksenofontov L.T. (2005). *Magnetic field amplification in Tycho and other shell-type supernova remnants.* A&A **433** 229–240. arXiv:astro-ph/0409453.

Walter M. and Wolfendale A. (2012). *Early history of cosmic particle physics.* The European Physical Journal H **37** 323–358. 10.1140/epjh/e2012-30020-1, URL http://dx.doi.org/10.1140/epjh/e2012-30020-1.

Welsh B.Y. and Sallmen S. (2003). *High-velocity NaI and CaII absorption components observed towards the IC 443 SNR.* A&A **408** 545–551.

Wulf T. (1909). *Über den Ursprung der in der Atmosphäre vorhandenen γ-Strahlung.* Physikalische Zeitschrift **10** 997–1003.

Yang R., Reichardt I. and de Oña Wilhelmi E. (in preparation). *The supernova remnant HC40 in GeV gamma rays* .

Zanin R. (2011). *Observation of the Crab pulsar wind nebula and microquasar candidates with MAGIC.* Ph.D. thesis, Universitat Autònoma de Barcelona. URL http://magic.mppmu.mpg.de/publications/theses/RZanin1.pdf.

Zatsepin G. and Kuzmin J. (1966). Exp. Theor. Phys. Lett. **4** 89.

Zirakashvili V.N. and Aharonian F.A. (2010). *Nonthermal Radiation of Young Supernova Remnants: The Case of RX J1713.7-3946.* ApJ **708** 965–980. 0909.2285.